Measurement of the elastic electron deuteron cross-section and determination of the electric form factor in the region of low Q^2

Dissertation

zur Erlangung des Grades
Doktor der Naturwissenschaften

dem Fachbereich Physik, Mathematik und Informatik
der Johannes Gutenberg-Universität Mainz
vorgelegt von

Dipl. Phys.
Yvonne Andrea Stöttinger
geb. Kohl

geboren in Wiesbaden

Mainz, 27.05.2019

1. Berichterstatter:
2. Berichterstatter:

Tag der mündlichen Prüfung: 06. Mai 2021

Abstract

The electromagnetic form factors of light nuclei provide a sensitive test of our understanding of nuclei. The deuteron in particular, as the only bound two-nucleon structure, is a fundamental system that has received extensive attention in the past, by both theory and experiment. Because the deuteron has a spin of one, three form factors are needed to fully describe the electromagnetic structure of the deuteron. Especially the deuteron charge radius is a favorite observable to compare experiment and theory. An extensive measurement campaign has been performed at MAMI (Mainz Microtron) to determine the deuteron charge radius using elastic electron scattering. The experiment took place at the 3-spectrometer facility of the A1-collaboration. Cross section measurements of the elastic electron-deuteron scattering have been performed for 180 different kinematic settings in the low momentum transfer region. The overlapping acceptances of the measurements maximize the internal redundancy of the data and allow a tight control of systematic uncertainties. The simulation of the electron-deuteron scattering as well as the simulation of the cryogenic depositions around the target cell are important tasks in the analysis.
The first step of the analysis is the preparation of the raw data by using cuts on the accepted momenta, the out-of-plane angle and the in-plane angle to reduce the background. The handling of the background originating from electrons which were scattered at the walls of the target cell is a critical objective in the analysis of the data. Since the tail of the distribution of these electrons is located - in particular for small scattering angles - beneath the elastic deuteron peak it has to be removed as effectively as possible from the rest of the data. Since available simulations of this contribution to the background did not include the inelastic part, the data from the empty cell measurements had to be used instead of the simulation to subtract the wall contribution of the background.
Based on the data of the cross section measurements, the charge form factor was determined by two methods. The first approach was to fit the measured cross sections divided by the cross section given by the calculations of the group of Abbott et al with a Sum-of-Gaussians parametrization. In the second approach the measured data points for the cross section were used to calculate the charge form factor for each Q value. It was found that the two methods are consistent.
From the fit to the form factor, the radius can be determined from the slope at zero momentum transfer. The obtained value for the deuteron radius in this thesis $r_d = (2.121 \pm 0.007_{\mathrm{stat.}} \pm 0.014_{\mathrm{syst}})$fm is in agreement with most of the values from previous measurements, but at the same time exhibits a tendency to a smaller value in comparison to the other results.
Due to the systematic uncertainties a more precise conclusion cannot be drawn at this point. The largest contribution to these systematic uncertainties is that of the background subtraction.

Contents

1 Introduction

The building blocks of matter consist of protons, neutrons and electrons. The first experimental evidence for the internal structure of atoms was found by Rutherford, Geiger and Marsden in 1911 [1, 2]. Based on the results from experiments of scattering α-particles at gold foils, models for the internal structure of atoms were developed. The electron was already known since its discovery by Thompson [3] in 1897 and the first indications for protons were found by Wien in 1898 [4]. By that time Rutherford created the model of the atom as a system of a large hull made out of very small electrons and a very small nucleus, which is much heavier than all the electrons in the hull. It was also Rutherford who discovered the unique role of the proton, being also the hydrogen nucleus, when he transmuted nitrogen into oxygen in 1919 [5]. The missing piece of the puzzle, the neutron, was then discovered in 1932 by Chadwick [6].
In more than 100 years since the first indication of the existence of the proton a lot of experiments were performed, so that today the mass of the proton is known to be 938.2796(27) MeV/c^2, its charge to be $1.602 \cdot 10^{-19}$ C and its spin to be $\frac{1}{2}\hbar$ [7].
A formalism to describe charged point-like spin-$\frac{1}{2}$-particles in relativistic quantum mechanics was developed by Dirac in 1928 [8]. On basis of the Dirac-equation the magnetic moment of such a particle is given as

$$\mu = g \cdot \frac{Ze}{2M} \cdot \frac{\hbar}{2} \tag{1.1}$$

where M is the mass of the particle, Ze is its charge, $\hbar$ is Plancks constant divided by 2π and $g = 2$ is the gyromagnetic ratio[1].
Assuming a point like proton the expected value for its magnetic moment μ_p is 1. In experiments by Stern, Frisch and Estermann in 1933 [12, 13] μ_p was determined to be 2.5 times larger than expected. Later measurements found the more precise value of 2.792847351(9) [7]. In the case of the proton this deviation cannot be explained by higher order calculations in quantum electrodynamics (QED) and quantum chromodynamics (QCD), but it is an indicator for the inner structure of the proton. As it is understood today, the proton is not point-like but consists of two up quarks and one down quark. Therefore the proton (as well as the neutron) is a baryon, which is a hadron composed of three quarks. As a hadron the proton is held together by the strong interaction [7].

[1] The deviation from $g = 2$, which was found in experiments can be explained by quantum electrodynamics (see [9–11])

Although a decay of a proton into for example a pion and a positron would be kinematically possible, such a decay has never been observed. Therefore the proton can be called a stable particle with a lifetime greater than $6.6 \cdot 10^{33}$ years [14].

A perfect tool for investigating the internal structure of nucleons is elastic electron scattering. Since electrons have, as far as we know, no inner structure and are point-like particles they are the perfect projectiles for experiments in which the cross section of the scattering is being measured. Again it was Rutherford who found an expression for the cross section for scattering an electron at a nucleus [1]. Since his equation did not include the spin and the spatial dimension of the nucleus, some modifications have to be applied (see 2.1). The spatial dimension of a nucleus is given by the form factor which is basically the Fourier transformation of the charge function. The proton has an electric G_E and a magnetic form factor G_M, which are both accessible in unpolarized elastic electron proton scattering.
The first measurements of nucleon form factors were performed in the 1950s at the Stanford University in California by Hofstadter [15–17]. These measurements lead to the description of the form factors of the proton and the magnetic form factor of the neutron as a dipole form. This empirical choice of a parametrization of the form factors relates to an exponential distribution of the charge and is still used today as a simple approximation to the data. But since measurements in 1980 in Mainz it is clear that this description is not sufficient [18].
The form factors of the nucleons were measured in many experiments since the 1950s, which lead to a lot of data points that all roughly agree with the dipole parametrization. The interest in the form factors was raised in recent years especially for the region below 1 $\left(\frac{GeV}{c}\right)^2$ because of three findings:
The first arose in a reanalysis of the world form factor data by Friedrich and Walcher in 2003 [19]. They fitted a phenomenological model to the data, which consisted of two dipole terms and a needed bump to achieve a good fit. The bump term was found in all proton and neutron form factors at similar positions. The existence of this structure could be an indication for a pion cloud, which is part of the description of the proton as a superposition of a proton and a combination of a neutron and a π^+.
The second is the observation of differences in the ratio $G_E(Q^2)/G_M(Q^2)$ measured by Rosenbluth techniques and by polarization transfer techniques, first observed in [20]. This led to the recognition of the importance of hard two-photon exchange corrections [21]. Calculations of two-photon exchange depend on the off-shell structure of the photon and are not under precise theoretical control. Experimental measurements generally constrained two-photon effects to be no more than $\approx 1\%$. This topic continues to be under active investigation, due to its potential impact on knowledge of the proton structure [22].
The third important finding came from atomic physics. The proton radius can also be measured by using laser spectroscopy of electronic or muonic hydrogen, an atom formed by an electron respectively a negative muon and a proton, and therefore links the fields of nuclear and atomic physics. In the recent past an experiment with laser spectroscopy of the 2S-2P transition in muonic hydrogen with 10 ppm accuracy was performed at the Paul-Scherrer Institute (PSI), Switzerland [23].

The finding of this experiment was a 6σ discrepancy between the measured 2S-2P resonance frequency and its QED prediction. Included in this prediction is the knowledge of fundamental constants like the electron and the muon mass, the fine-structure constant and others, as well as the proton charge radius [23]. Since this radius is the least well-known of the needed constants, the attention was pointed to this quantity [24]. The proton charge radius extracted by this experiment is $r_p = 0.84087(39)$ fm. Compared to the other two methods with which it is possible to measure the proton radius, elastic scattering of electrons at protons and high-precision continuous-wave laser spectroscopy of hydrogen, the accuracy reached with the spectroscopy of muonic hydrogen surpasses the other two methods by an order of magnitude [23]. But the discrepancy between the result for the radius from muonic hydrogen and the other determinations is 5.6σ. Since this large discrepancy is not explained yet, it is known as the proton radius puzzle.
The proton radius is the subject of ongoing discussions. Here only a few facts and remarks will be given (for more details see [23]).
The spectroscopy of muonic hydrogen is very sensitive to the proton charge radius, but insensitive to possible systematic effects [25, 26]. Because of the rate of six events/h observed on resonance, the scanning of the 2S-2P resonances is quite time consuming. This lead to a limit on the total accuracy induced by the statistical uncertainty, making the results less prone to systematic effects.
The spectroscopy of hydrogen requires the knowledge of the Rydberg-constant R_∞. To deduce R_∞ and r_p two measurements are usually done. The first uses the transition 1S-2S, since it is the most accurate one and has the largest sensitivity to r_p [27]. The second one utilizes the transition from 2S to 4S, 8S, 8D, 12D etc. [28].
The 4σ discrepancy between r_p from muonic and electronic hydrogen spectroscopy is caused by the big discrepancy for two of the transitions in the second measurement. The others show a discrepancy below 2σ [29, 30]. New measurements for R_∞ could find an error in these two transition measurements and could lead to less discrepancy in total between electronic and muonic hydrogen.
It is also possible that there is an error in the muonic hydrogen theory. The largest contributions to the theory are the one-loop electron vacuum polarization, the finite-size contribution, the two-loop electron vacuum polarization and the one-loop muon self energy together with the muon vacuum polarization. Since all the other contributions are smaller than the discrepancy itself, it is improbable that the discrepancy can be explained by miscalculations in one of these [31–33]. But since the two-photon exchange contribution (TPE) cannot be simply computed using proton form factors, the explanation of the proton radius puzzle might also be reached by new calculations of this contribution [34].
In electron proton scattering one major point of discussion is how the different analysis methods handle the extrapolation to $Q^2 = 0$. This extrapolation is needed because the form factor G_E can be measured only down to a minimal Q^2, but for the calculation of r_p, the value of the form factor slope at $Q^2 = 0$ is needed [35–38]. Since the extrapolation would be easier and more accurate with more data at very low Q^2, new experiments have been initiated, for example a pilot measurement in Mainz in 2013 demonstrates the feasibility of the usage of initial state radiation [39]. One possibility to investigate this problem in more detail is to compare radius extrac-

tions from similar experiments on the next higher nuclei, specifically on the deuteron. Also the deuteron radius can be obtained by different kinds of experiments. As can

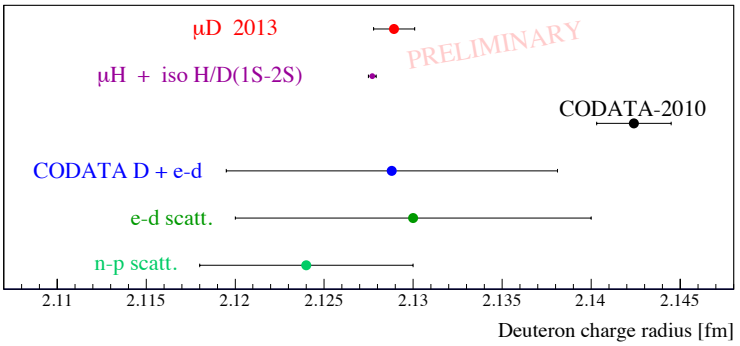

Figure 1.1: The deuteron radius obtained by different kinds of measurements. See text for details. [40]

be seen in fig. 1.1 the value obtained by measurements with myonic deuterium is known with a very high precision [40], but it does not agree with the CODATA-2010 value [41]. Since the CODATA value for the deuteron radius is calculated from the proton radius and the difference $r_d^2 - r_p^2$ obtained from the measurement of the isotopic shift, the puzzle can also be seen for the deuteron. So the puzzle exists not only for the proton, but also for the deuteron. However the value from elastic electron deuteron scattering still has a comparatively large error. In order to distinguish between the CODATA and the myonic-deuterium value a reduction of the electron-deuteron scattering error of about a factor of two is required. With a more exact value for the deuteron radius also a value for the proton radius can be obtained by using again $r_d^2 - r_p^2$ from the isotopic shift measurements [23].
The beam of the MAinz MIcrotron (MAMI) and the detector setup of the A1-collaboration allow a high precision measurement of the elastic electron-deuteron cross section in the Q region below $2fm^{-1}$. The estimated errors for such a measurement at the Mainz setup are smaller than most of the errors of the data points, which were measured by other groups in the past. The dominating part of these errors are the systematic ones, since small statistical errors can be achieved due to high count rates for elastic electron deuteron scattering.
This thesis is organized in 7 chapters. In the first section of chapter 2 scattering experiments and all associated important quantities are introduced. In the second section the theoretical foundations of the elastic electron-deuteron cross section are described and the required radiative corrections are discussed. The end of chapter 2 establishes the connection between the deuteron and the proton radius.
Chapter 3 describes the setup available in Mainz. This includes the electron accelerator MAMI, the 3-spectrometer facility with the magnetic system and the detector system as well as the target chamber. Also relevant setup components like a picoamperemeter and a beam position stabilization will be discussed. In this chapter also the measuring program will be introduced. The end of this chapter form the description of the luminosity measurement and the necessary calibrations.
The data analysis chapter (chapter 4) is composed of the two main parts: simulation and data analysis. In the simulation sections the simulations for the elastic scattering at deuterium as well as the simulation of scattering at cryogenic depositions

and at the target wall are discussed. The first part of the data analysis section is the description of the data preparation, including luminosity calculations and event identification. Also the target background is discussed in detail. In the end of this chapter the form factor parametrization, which was used in this thesis, as well as the fit to the cross section data is described, including the determination of the errors. The result of the fit for the cross section is presented in chapter 5.
Chapter 6 summarizes the results of this thesis and gives an outlook for possible future experiments to resolve remaining problems.

2

Electron - Deuteron - Scattering

2.1 Scattering experiments

Scattering experiments are a fundamental method in nuclear and particle physics to investigate details of interactions between different particles as well as the inner structures of atoms and their components.
In a typical scattering experiment a beam of particles with well-defined energy is directed on the object of investigation, also called the target. The projectile particles and the target particles will interact with each other. The products of this reaction can be measured with various detector systems in order to get the rate, energy and mass as well as their angle relative to the direction of the incoming beam.
Experimentally it is possible to use beams of various particles (electrons, protons, neutrons, heavy ions, etc). Depending on the kind of particle one can reach beam energies between 10^{-3} eV for 'cold' neutrons and 10^{13} eV for protons.
Target materials can be solid, liquid, gaseous or even - in storage ring experiments - other particle beams. In elastic scattering experiments the particles before and after the reaction are the same, only the momenta and energies of the particles change. By using different energies of the incoming beam and measuring the outgoing particles at different scattering angles conclusions about the shape of the target particle (or the beam) can be drawn.
In scattering experiments the measured reaction rates as well as energy and angle distributions of the reaction products provide information about the dynamics of the interaction, that is about the shape of the interaction potential and the coupling strength. The most important parameter in describing these reactions is the cross section σ, which is a measure for the probability of a reaction between the beam particle and the target particles.

2.1.1 Geometrical reaction cross section

A graphic description of the cross section is the geometrical reaction cross section. For this a thin target with thickness d, particle density n_b and N_b scattering points is considered. Each target particle has the area cross section σ.
To determine this area cross section a mono energetic beam of point like particles is directed on the target. In this model each time a beam particle hits a target particle there is a reaction (and the projectile vanishes out of the beam after the reaction).

The total reaction rate $\dot{N}$ is given by the difference of the beam particle rate $\dot{N}_a$ before and after the target material and is a direct measure for the area cross section σ.
If the incoming particle beam has the area A and the density of beam particles is n_a, the flux ϕ_a of particles hitting the target is the product of the density and particle velocity v_a:

$$\phi_a = \frac{\dot{N}_a}{A} = n_a \cdot v_a \qquad [\phi_a] = \frac{1}{\mathrm{m^2 s}} \tag{2.1}$$

The number of target particles in the cross section area of the beam is $N_b = n_b \cdot A \cdot d$ and the reaction rate is $\dot{N} = \phi_a \cdot N_b \cdot \sigma$
This formula is applicable, if the scattering points are not overlapping and the scattering only happens at a single scattering point. The geometrical reaction cross section is therefore:

$$\sigma_b = \frac{\dot{N}}{\phi_a \cdot N_b} \tag{2.2}$$

This definition is valid for a beam which is homogenous and constant in time. Often this is already a good approximation. In general the probability of a reaction between two particles can differ strongly from the value one would expect based on their geometrical size.

2.1.2 Electron scattering

To investigate small objects like atoms or nuclei often scattering experiments with electron beams are used [42]. Electrons are, as far as we know, point like particles with no inner structure. The interaction between an electron and the nucleus is carried out in the first Born approximation by a virtual photon, which can be described using quantum electrodynamics. Since the electrons in these experiments are relativistic particles, four vectors are normally used in the calculations. The incident electron is scattered in the direction $\Omega = (\theta, \phi)$. The unpolarized cross section is independent of the azimuthal scattering angle ϕ. Therefore it has two degrees of freedom, e.g. the energy of the incoming electron E and the scattering angle θ. The virtual photon in the scattering process has a negative four-momentum squared, it is space like. Therefore, the negative of q^2 is

$$Q^2 = -q^2 = 4EE' \sin^2\left(\frac{\theta}{2}\right) > 0. \tag{2.3}$$

The energy E' of the scattered electron in the laboratory system is

$$E' = \frac{E}{1 + \frac{E}{M \cdot c^2 \cdot (1 - \cos\theta)}} \tag{2.4}$$

with the target mass M and speed of light c.

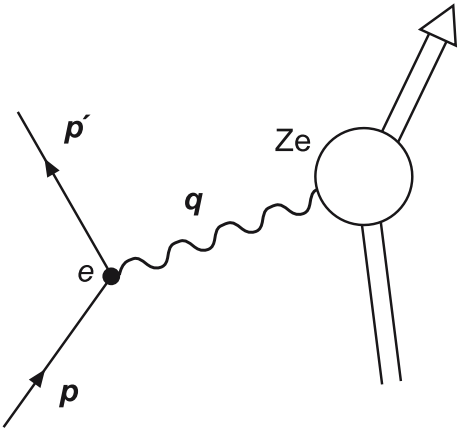

Figure 2.1: Drawing of the scattering process of a electron e at a nucleus Ze. The incoming electron has momentum p, after the scattering took place the outgoing momnetum is p'. The momentum of the virtual photon is q.

In case of elastic scattering there is a distinct relation between the scattering angle and the energy of the scattered electron. In case of inelastic scattering eq. 2.4 is no longer valid.
The cross section for the scattering of an electron with energy E at a nucleus with charge Ze under disregard of the spin is given by the Rutherford cross section [1].

$$\left(\frac{d\sigma}{d\Omega}\right)_{\text{Rutherford}} = \frac{4Z^2\alpha^2(\hbar c)^2E'^2}{|qc|^4} \tag{2.5}$$

with momentum transfer $\vec{q} = \vec{p} - \vec{p'}$ ($\vec{p}$, $\vec{p'}$ are the momenta before and after the scattering), atomic number Z, coupling constant α, Planck constant $\hbar$.
In experiments with relativistic energies the Rutherford cross section is modified by spin effects [43]. The cross section of the electron scattering is now given by the Mott cross section

$$\left(\frac{d\sigma}{d\Omega}\right)_{\text{Mott}} = \left(\frac{d\sigma}{d\Omega}\right)_{\text{Rutherford}} \cdot \cos^2\left(\frac{\theta}{2}\right) \tag{2.6}$$

In scattering experiments on nuclei or nucleons the experimental cross section equals the Mott cross section only in case $|q| \to 0$, for higher $|q|$ the experimental cross section is systematically smaller. The reason for this is the spatial dimension of nuclei and nucleons. For higher $|q|$ the wavelength of the virtual photons is smaller and the resolution is higher.
The spatial dimension of a nucleus is given by the form factor,

$$F(q) = \int \exp\left(iqx/\hbar\right) f(x) d^3x \tag{2.7}$$

which is the Fourier transformation of the charge function $f(x)$, which is normalized to the total charge. The form factor contains all information about the spatial distribution of the charge of the examined object. For radial charge distributions it is possible to calculate the form factor analytically. In fig. 2.2 some examples for

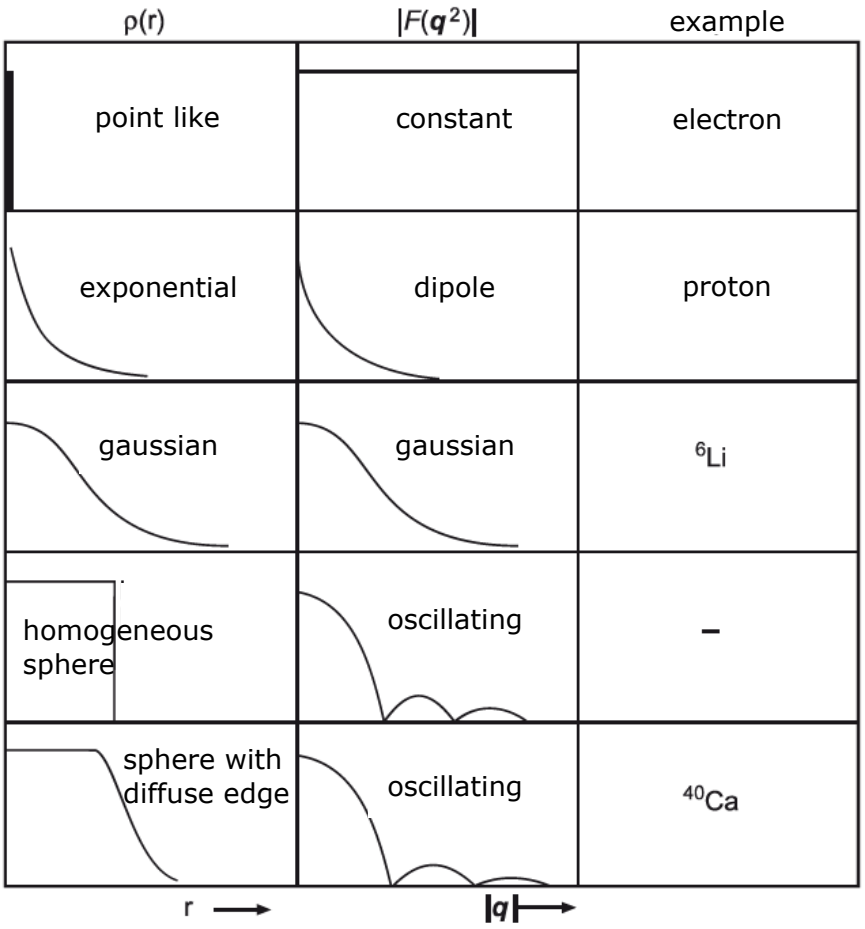

Figure 2.2: Connection between radial charge distribution and form factor in Born approximation. A constant form factor corresponds to a point like charge (e.g. electron), a dipole form factor to an exponentially declining charge distribution (e.g. proton), a gaussian form factor to an gaussian charge distribution (e.g. ^{6}Li nucleus) and an oscillating form factor corresponds to a homogeneous sphere with more or less sharp edge. All nuclei, but the very light ones, have an oscillating form factor.

this kind of distributions are shown.
For spherical-symmetrical systems the form factor is only depended on $|q|$. That is why the form factor is written from now on as $F(q^2)$ [44].
Experimentally the form factor is determined as the ratio between Mott cross section and measured cross section:

$$\left(\frac{d\sigma}{d\Omega}\right)_{\text{exp}} = \left(\frac{d\sigma}{d\Omega}\right)_{\text{Mott}} \cdot \left|F\left(q^2\right)\right|^2 \tag{2.8}$$

The proton cross section is given by the Rosenbluth equation [45], which contains the electrical form factor $G_E(Q^2)$ and the magnetic form factor $G_M(Q^2)$. From the extrapolation of $G_E(Q^2)$ to $Q^2 = 0$, the proton electric form factor can be extracted from the slope:

$$\left(\frac{dG_E}{dQ^2}\right)_{Q^2=0} = -\frac{1}{6}r_p^2 \tag{2.9}$$

The cross section is measured for a given beam energy for different scattering angles (and therefore different q^2) and the Mott cross section is calculated for each of the measured angles.
A typical detector system for measuring form factors is the 3-spectrometer facility of the A1 collaboration in Mainz, which is described in detail in chapter 3.

2.2 The deuteron

Electron scattering provides an excellent tool for a detailed check of theoretical calculations of few body nuclei. The simplest nucleus containing both types of nucleons is the deuteron. Being a weakly bound state of a proton and a neutron, it provides a unique playground for investigating nuclear forces and nuclear dynamics. Understanding its structure has far-reaching implications, not only for nuclear physics itself but also for the experiments that exploit the deuteron as an effective neutron target in order to obtain information on the neutron. Therefore, it has been extensively studied by both theoreticians and experimentalists. [42]
An important insight into its properties can be obtained by studying the three electromagnetic form factors of the deuteron. The charge form factor is of special interest since it carries information about the charge distribution inside the deuteron and the charge radius of the nucleus. There have been already several electron deuteron scattering measurements in the past [46–48]. But as can be seen in fig. 2.3 the results for the cross section do not fully agree. The results from Simon *et al.* [47] indicate a higher cross section in the middle of the shown Q range, but the results from Platchkov *et al.* [48] indicate a rising slope at higher Q. Also many of the prior data points have a large error.
The measurement for this work was done with settings over the Q range indicated by the green dots in fig. 2.3. The estimated errors for this measurement are smaller

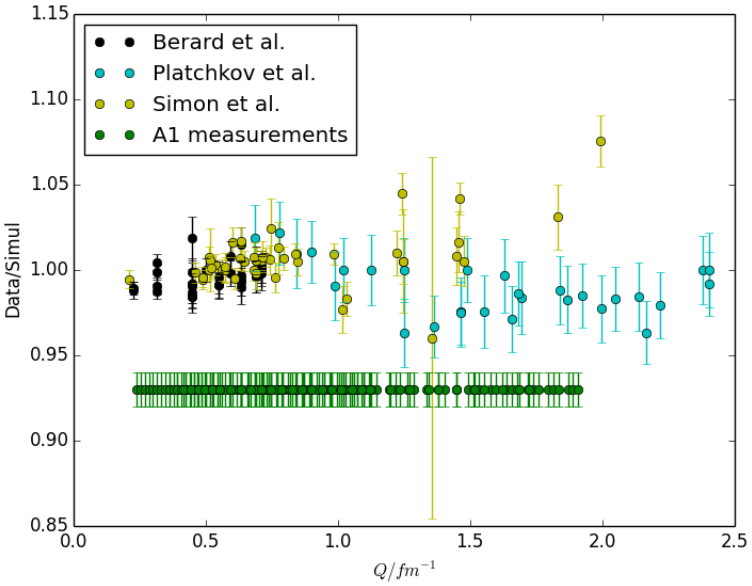

Figure 2.3: Cross section obtained by prior experiments relative to fitted result. The green points indicate the measured Q range at MAMI with the estimated errors. (Berard *et al.*: black, Simon *et al.*: lightgreen, Platchkov *et al.*: turquoise)[46–48]

than most of the errors of the existing data points. The dominating part of these errors are the systematic ones, the statistic errors are much smaller.
By extracting the deuteron radius it is possible to make also a statement about the proton radius puzzle. From isotope shift (2S-1S) measurements between hydrogen and deuterium the difference of the quadratic radii is known [49]:

$$r_d^2 - r_p^2 = 3.82007(65)\text{fm}^2 \tag{2.10}$$

With this relation a value for the proton radius can be determined by the deuteron radius. Therefore the goal of this experiment is to reduce the error of the deuteron radius as far as possible.

2.2.1 Cross section of elastic electron - deuteron scattering

The cross section for unpolarized electron-deuteron scattering can be written as in [50] (from now on $c = 1$ and $\hbar = 1$):

$$\frac{d\sigma}{d\Omega} = \left(\frac{d\sigma}{d\Omega}\right)_{\text{Mott}} \left[A\left(Q^2\right) + B\left(Q^2\right)\tan^2\left(\frac{\theta}{2}\right)\right] \tag{2.11}$$

$A\left(Q^2\right)$ and $B\left(Q^2\right)$ are the two structure functions, which are defined by the quantity S in

$$\frac{d\sigma}{d\Omega} = \left(\frac{d\sigma}{d\Omega}\right)_{\text{Mott}} \cdot S \tag{2.12}$$

$$S = A + B\tan^2\left(\frac{\theta}{2}\right) \tag{2.13}$$

The structure functions are quadratic combinations of the three electromagnetic form factors which characterize a spin 1 nucleus:

$$A\left(Q^2\right) = G_C^2\left(Q^2\right) + \frac{8}{9}\eta^2 G_Q^2\left(Q^2\right) + \frac{2}{3}\eta G_M^2\left(Q^2\right) \tag{2.14}$$

$$B\left(Q^2\right) = \frac{4}{3}\eta(1+\eta)G_M^2\left(Q^2\right) \tag{2.15}$$

$$\eta = \frac{Q^2}{4M_d} \tag{2.16}$$

with the charge form factor G_C, the quadrupol form factor G_Q, the magnetic form factor G_M, the mass of the deuteron $M_d = 1875.612$ MeV and the scattering angle of the electron θ.
In the same way as in the case of the proton, the deuteron radius can be extracted from the extrapolation of $G_C\left(Q^2\right)$ to $Q^2 = 0$:

$$\left(\frac{dG_C}{dQ^2}\right)_{Q^2=0} = -\frac{1}{6}r_d^2 \tag{2.17}$$

A notable difference to the cross section of the electron proton scattering is that in the case of the deuteron, since it is a spin 1 particle, there are only two unpolarized structure functions but three form factors. Since $B(Q^2)$ depends only on G_M, this form factor can be determined by a Rosenbluth-separation of $A(Q^2)$ and $B(Q^2)$, or by a cross section measurement at $\theta = 180°$. $A(Q^2)$ depends on all three form factors, so it is not possible to do a full Rosenbluth-separation using unpolarized electron deuteron scattering [45]. Only the longitudinal part of $A(Q^2)$, which is a quadratical combination of G_C and G_Q can be determined from the unpolarized cross section.
In order to extract G_C in this experiment the contributions of the other two form factors will be estimated from a parametrization obtained from dedicated measurements of other groups. This is possible since the charge form factor G_C dominates the cross section at low Q^2.

2.2.2 Radiative corrections

The cross section given by eq. 2.11 contains the nuclear information, but cannot be measured, since it holds only the lowest order Feynman diagram, where the scattering of the electron at the deuteron is mediated by just one exchanged virtual

photon. When measuring the cross section also higher order Feynman diagrams contribute and need to be included in the calculation in order to extract the form factor. These Feynman diagrams describe the additional radiative processes which lead to a correction of the cross section:

$$\left(\frac{d\sigma}{d\Omega}\right)_{\text{radiative}} = \text{corr} \cdot \left(\frac{d\sigma}{d\Omega}\right)_{\text{non radiative}} \tag{2.18}$$

In fig. 2.4 the non radiative amplitude of elastic electron scattering and the leading

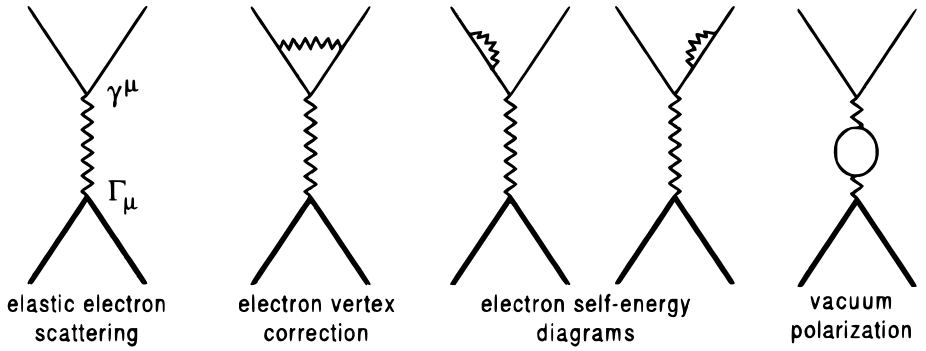

Figure 2.4: Feynman diagrams as graphical representation of the non radiative amplitude of elastic electron scattering and elastic amplitudes with radiative corrections on the electron side [51].

elastic amplitudes with radiative corrections on the electron side are shown. The first Feynman diagram is the non radiative amplitude of interest. The electron vertex, the electron self-energy and the vacuum polarization corrections have been studied extensively. The integrals over the internal four-momenta of these graphs are logarithmically divergent for large momenta. This can be treated by charge and mass renormalization. Details can be found in [51–53].
In addition to the elastic amplitudes with radiative corrections on the electron side, there are also inelastic amplitudes with radiative corrections on the electron side which need to be taken into consideration. The lowest order ones are shown in fig. 2.5. These diagrams describe the initial state radiation (ISR) and the final state

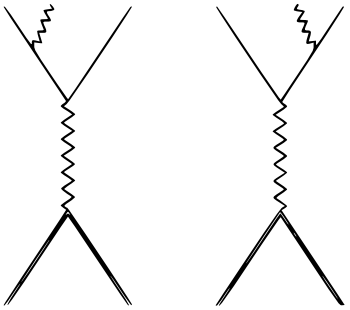

Figure 2.5: Feynman diagrams as graphical representation of the inelastic amplitudes with radiative corrections on the electron side (initial and final state radiation)[51].

radiation (FSR).

All these radiative corrections can be added as a correction factor to the cross section calculation:

$$\left(\frac{d\sigma}{d\Omega}\right)_{\text{rad}} = \left(\frac{d\sigma}{d\Omega}\right)_{\text{non rad}} \cdot (1+\delta) \tag{2.19}$$

For different feynman diagrams the factor δ is divided into different parts. As a result for the radiative corrections on the electron side one gets:

$$\left(\frac{d\sigma}{d\Omega}\right)_{\text{rad}} = \left(\frac{d\sigma}{d\Omega}\right)_{\text{non rad}} \cdot (1+\delta_{\text{vac}}+\delta_{\text{vertex}}+\delta_{\text{real radiative}}) \tag{2.20}$$

with

$$\begin{aligned}\delta_{\text{vac}}+\delta_{\text{vertex}}+\delta_{\text{real radiative}} = \frac{\alpha_{em}}{\pi}\Bigg(&\frac{13}{6}\ln\left(\frac{Q^2}{m^2}\right)-\frac{28}{9}-\frac{1}{2}\ln^2\left(\frac{E_e}{E'_e}\right)\\ &-\frac{\pi^2}{6}+\text{Sp}\left(\cos^2\frac{\theta_e}{2}\right)\\ &+\ln\left(\frac{(\Delta E_S)^2}{E_e\cdot E'_e}\right)\left(\ln\left(\frac{Q^2}{m^2}-1\right)\right)\Bigg)\\ \Delta E_S = \xi(E'^{el}_e - E'_e) = \xi\Delta E'&\\ \xi = \frac{E_e}{E'^{el}_e}&\end{aligned} \tag{2.21}$$

where $\alpha_{em}=\frac{e^2}{4\pi}$ is the fine-structure constant and m is the mass of the electron. E_e is the energy of the unscattered electron and E'_e the energy of an electron scattered under an angle θ when no photon is emitted. $\Delta E'$ is the maximum difference to E'_e allowed by the radiative tail cut-off; it is called the cut-off energy, E'^{el}_e denotes the elastic scattered electron lab energy, to distinguish from E'_e and ΔE_S is the maximum soft photon energy in the center of mass system of (recoiling deuteron and soft photon). Details about the Spence function $\text{Sp}(x)$ can be found in [54].
In addition to the radiative corrections on the electron side, there are also analog contributions on the deuteron side. These are the elastic amplitudes of the deuterium vertex correction, the deuterium self-energy and the box and crossed-box diagrams (fig. 2.6) as well as the inelastic amplitudes of deuterium ISR and FSR (fig. 2.7). Since there are no complete calculations of these corrections for spin-1 particles, an approximation based on the calculations for the proton was used for this thesis. This approach is based on a statement from Maximon and Tjon [51], where it is written *"..although we are primarily interested in electron-proton scattering, the radiative corrections studied here can also be applied to electron-nucleus scattering, with appropriate changes in F_1 , F_2 , [...] and M."* (F_i are the form factors and M the target mass). Furthermore the corrections on the deuteron side contribute less to the cross section since they are suppressed by the mass of the deuteron.

The results for the radiative corrections on the deuteron side can be divided into

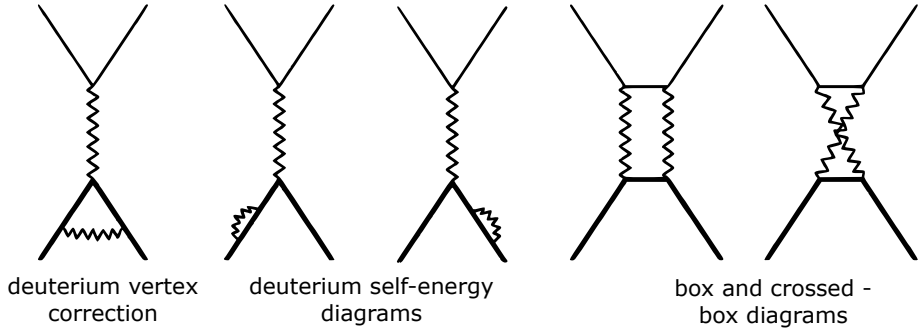

Figure 2.6: Feynman diagrams as graphical representation of amplitudes with radiative corrections on the deuteron side [51].

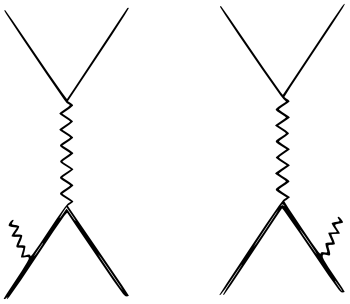

Figure 2.7: Feynman diagrams as graphical representation of inelastic amplitudes with radiative corrections on the deuteron side (initial and final state radiation)[51].

one part δ_1 which is proportional to Z (hadron charge):

$$\delta_1 = \frac{2\alpha_{em}}{\pi}\left(\ln\left(\frac{4(\Delta E_S)^2}{Q^2 x}\right)\ln(\eta) + \mathrm{Sp}\left(1-\frac{\eta}{x}\right) - \mathrm{Sp}\left(1-\frac{1}{\eta x}\right)\right), \tag{2.22}$$

where ΔE_S and η are given as in equation 2.21 and where the variable x is defined by

$$\begin{aligned} x &= \frac{(Q+\rho)^2}{4M} \\ \rho^2 &= Q^2 + 4M^2 \end{aligned} \tag{2.23}$$

and one part δ_2 which is proportional to Z^2:

$$\begin{aligned} \delta_2 = \frac{\alpha_{em}}{\pi}\Bigg(& \ln\left(\frac{4(\Delta E_S)^2}{M^2}\right)\left(\frac{E'_D}{|\vec{p}'_D|}\ln x - 1\right) + 1 \\ & + \frac{E'_D}{|\vec{p}'_D|}\Bigg(-\frac{1}{2}\ln^2 x - \ln x \ln\left(\frac{\rho^2}{M^2}\right) + \ln x \\ & - \mathrm{Sp}\left(1-\frac{1}{x^2}\right) + 2\mathrm{Sp}\left(-\frac{1}{x}\right) + \frac{\pi^2}{6}\Bigg)\Bigg), \end{aligned} \tag{2.24}$$

where E'_D and $|\vec{p}'_D|$ are the lab energy and momentum of the recoiling deuteron. All the details of this calculation can be found in [51–53].

When the cross section for electron-deuteron scattering is measured, also further Feynman diagrams contribute to the cross section and need to be included in the cross section calculation. However, since the fine-structure constant α_{em} is much smaller than 1 and every additional vertex in a Feynman diagram contributes a factor α_{em} to the cross section calculation, these higher order diagrams become less and less important the more vertices they contain. Because of this the higher order diagrams were not taken into account for this analysis.
In addition to the corrections described so far, there is also the Coulomb correction which is due to the interaction of the electron with the Coulomb field of the target [52, 54, 55]. It has been found in [54] that, neglecting the inner structure of the deuteron the correction can approximately be written as $(1 + \delta)$ with:

$$\delta = Z\alpha_{em}\pi \frac{\sin\frac{\theta}{2} - \sin^2\frac{\theta}{2}}{\cos^2\frac{\theta}{2}}, \tag{2.25}$$

which depends only on the scattering angle of the electron. This correction has been applied to the measured cross section and is of the order of 1%.

3

The Experiment

In this chapter an overview of the MAinz MIcrotron (MAMI) accelerator and the detectors in the 3-spectrometer facility will be given [56–58]. There will be a brief overview of the whole accelerator and a more detailed description of the parts which were crucial for the experiment.
Furthermore, there will be a detailed specification of the 3 high-resolution magnetic spectrometers used by the A1 collaboration. One key aspect is the liquid deuterium/hydrogen target.

3.1 Electron accelerator MAMI

MAMI is a normal conducting continuous wave (cw) electron accelerator consisting of a cascade of three racetrack microtrons (RTM). This cascade can produce a beam with an energy up to 855 MeV and a current of 100 μA for nuclear, hadron and radiation physics experiments. After the electrons propagate through the three RTMs, they can be further accelerated by a forth stage: a Harmonic Double-Sided Microtron (HDSM), which generates up to 1.6 GeV electrons.
A schematic overview plan is depicted in fig. 3.1. For this experiment the thermionic electron source which can provide currents up to 100 μA was used, currents between a few nanoampere and 10 μA were used for this work. Alternatively the accelerator is also equipped with a polarized source that utilizes the photoelectric effect with a GaAs crystal.
The electrons produced by the source are injected into the first RTM by a linear accelerator. At this stage the electrons reach an energy of 3.5 MeV with high energy stability ($\leq$ 1 keV) [57]. The main parameters of the MAMI injector and the RTMs can be found in tab. 3.1.
Each of the RTMs consists of a normal conducting accelerator segment and two high-precision conventional magnets which recirculate the beam back into the accelerator segment. In RTM1 the beam starts with 18 recirculations and enters RTM2 with 14.86 MeV, by which the beam energy gets increased to 180 MeV in 51 turns. Here the beam may bypass the remaining accelerator stages and may be directed directly to the different experimental sites. (The part of the accelerator up to this point is also called MAMI A.) If more energy is needed for the experiments, the beam will instead enter RTM3, which can boost the energy up to 855 MeV in 90 turns (MAMI B). Every second recirculation path can be instrumented with a kicker magnet that

	Injector	RTM1	RTM2	RTM3
General				
injection energy (total) / MeV	0.511	3.97	14.86	180
extraction energy (total) / MeV	3.97	14.86	180	855
number of turns	-	18	51	90
Radio-frequency system				
frequency / GeV	2.4495	2.4495	2.4495	2.4495
linac length (electrically) / m	4.93	0.80	3.55	8.87
# of sections | klystrons	3 | 1	1 | 1	2 | 2	5 | 5
beam power / kW	0.35	1.1	16.6	67.5
Magnet system				
flux density / T	-	0.1026	0.5550	1.2842
min. deflection radius / m	-	0.129	0.089	0.467
max. deflection radius / m	-	0.482	1.083	2.216
# of corrector magnets	40	72	204	360
# of quadrupoles and solenoids	20	2	4	4
Beam parameters				
energy spread (1σ) / keV	1.2	1.2	2.8	13
norm. emittance horiz. (1σ) $/\pi \cdot 10^{-6}$m	0.05	0.07	0.25	13
norm. emittance vert. (1σ) $/\pi \cdot 10^{-6}$m	0.04	0.07	0.13	0.84
standard energies for experiments / MeV	-	-	180	195 - 855 in steps of 15 MeV

Table 3.1: Main parameters of MAMI injector and RTMs [57].

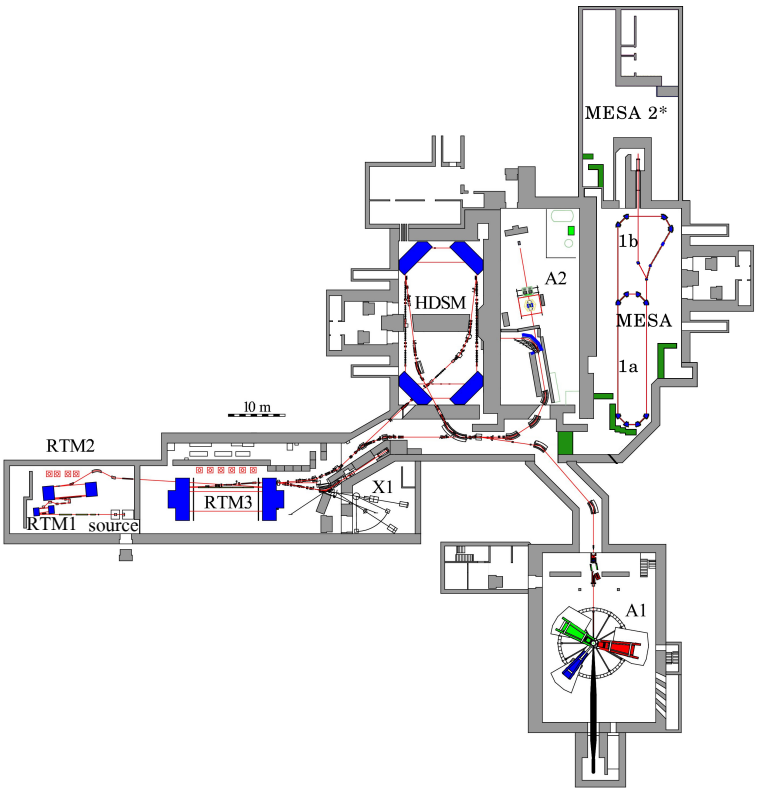

Figure 3.1: Schematic overview of the MAMI facility with all accelerator stages (RTM1/2/3, HDSM) and experimental halls (A1, A2, X1).

deflects the beam to the exit beam line system. In this way the energy can be selected in 15 MeV steps between 180 and 855 MeV.
The beam may then be injected into the last stage (MAMI C). The HDSM consists of two anti-parallel accelerator segments, in which the electrons are recirculated by four magnets. This stage raises the electron energy up to 1.6 GeV in 43 recirculations. For the measurements described in this work, beam energies of 180 MeV, 315 MeV and 450 MeV were used.

3.2 3-spectrometer facility

For this experiment the detector setup of the A1 collaboration at MAMI was used. It is called the 3-spectrometer-facility. This name originates from the three permanently mounted high resolution magnetic spectrometers, labeled A, B and C, which can be operated in single, double or triple coincidence mode. To measure at different scattering angles, the spectrometers can be rotated around a central pivot. A broad range of angles needed for the electron scattering experiments was accessible via remote control from the counting room. A photograph of the A1 experimental hall is shown in fig. 3.2, a detailed description of the whole setup can be found in [59].
The spectrometers of the A1 collaboration are high acceptance magnetic spectrometers, able to measure charged particles. The momentum of the particles as well as

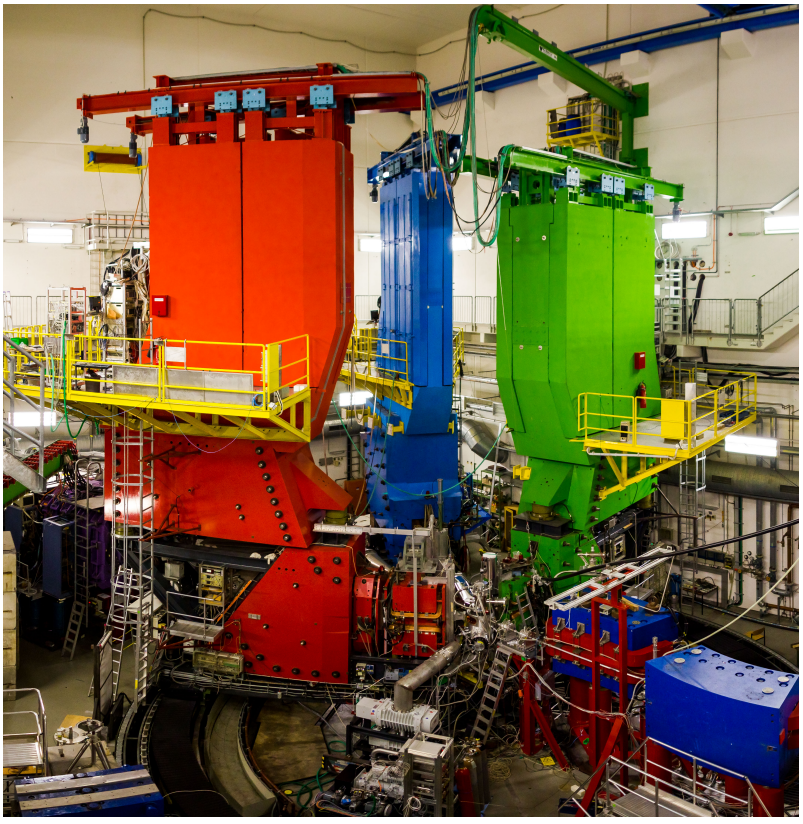

Figure 3.2: The A1 spectrometer hall with spectrometer A (red), B (blue) and C (green). The beam line pipe comes in from the right.

their angles can be determined with high accuracy. In fig. 3.3 the schematics of spectrometer A is shown. Originating from the target, the particles enter the spectrometer through the collimator and are mapped onto the focal plane of the magnetic system. This is the plane at the focal point onto which the magnetic system focuses the particles. The detectors of the spectrometer enable the determination of the trajectory of the particles inside the spectrometer. With this information conclusions about the momentum of the particle at the target can be drawn. In the following subsections the magnetic system and the detector system are described. The main specifications of the spectrometers are summarized in tab. 3.2. For the analysis of the data different coordinate systems are used. These coordinate systems are shown in fig. 3.4 on page 30. The vertex coordinate system (x, y, z) has its origin at the center of the target. The z-axis of this system possesses the same direction as the incoming electron beam. The non-dispersive angle is the angle in the xy-plane of the vertex system, while the dispersive angle represents the angle with respect to that plane.
The focal coordinate system $(x_f, y_f, \Theta_0, \Phi_0)$ is located in the focal plane of each spectrometer, e.g. the tracks determined with the VDCs are given in this system.

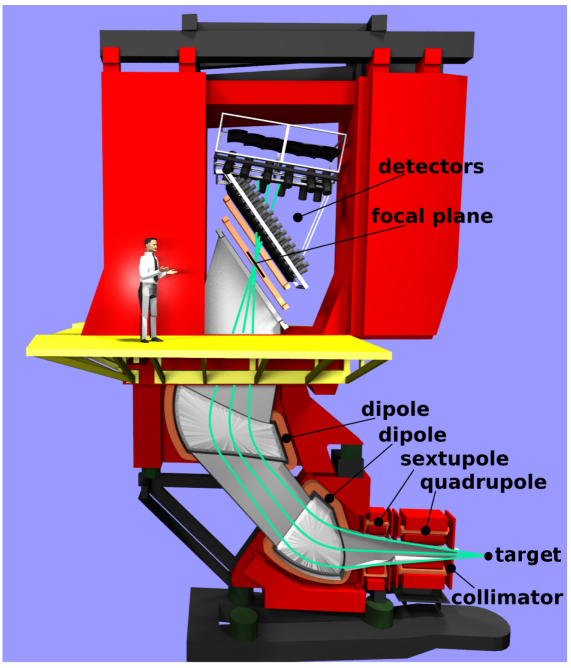

Figure 3.3: Schematic side view of spectrometer A. Particles enter the spectrometer at the collimator and are focused onto the focal plane (by the magnetic field of a quadrupole, a sextupole and two dipole magnets). The momentum of the particle is then determined by the detectors in the upper part of the spectrometer.

	Spec. A	Spec. B	Spec. C
configuration	QSDD	Clamshell D	QSDD
maximum momentum / (MeV/c)	735	870	551
reference momentum / (MeV/c)	630	810	459
central momentum / (MeV/c)	665	810	490
maximum solid angle / msr	28	5.6	28
momentum acceptance	20%	15%	25%
momentum resolution	10^{-4}	10^{-4}	10^{-4}
angular resolution at target / mrad	< 3	< 3	< 3
position resolution at target / mm	3 - 5	1	3 - 5
length of central path / m	10.75	12.03	8.53

Table 3.2: Main parameters of the spectrometers A, B and C.

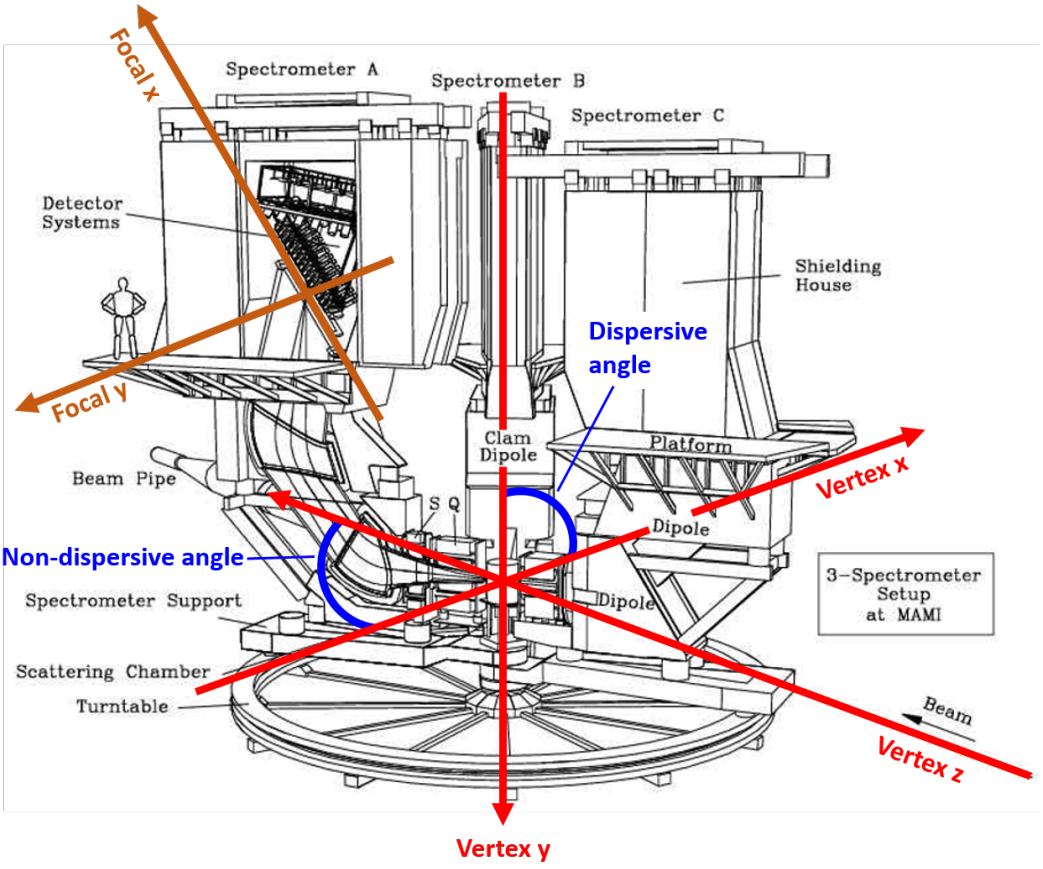

Figure 3.4: Schematics of the spectrometers with the different used coordinate systems. (modified version [60])

3.2.1 Magnetic system

The magnetic system of spectrometer A and C is comparable since spectrometer C is basically a scaled down version of spectrometer A. Both spectrometers consist of a quadrupole magnet, a sextupole magnet and two dipole magnets. In this configuration the quadrupole functions as a beam focus in non-dispersive direction and it defocuses the beam in dispersive direction. The magnetic system ends in point-to-point optics in the dispersive plane and parallel-to-point optics in the non-dispersive plane. This system enables high resolution measurements of particle angles and momentum within a relatively large acceptance (up to 28 msr).
Spectrometer B consists of only one single dipole in a clamshell configuration, resulting in a slim design with higher spatial resolution but smaller acceptance than spectrometer A and C (max. 5.6 msr). For out-of-plane measurements, spectrometer B can be tilted, but this feature was not utilized in this experiment.
Figure 3.5 shows the dimensions and magnet arrangements for spectrometer A and B.

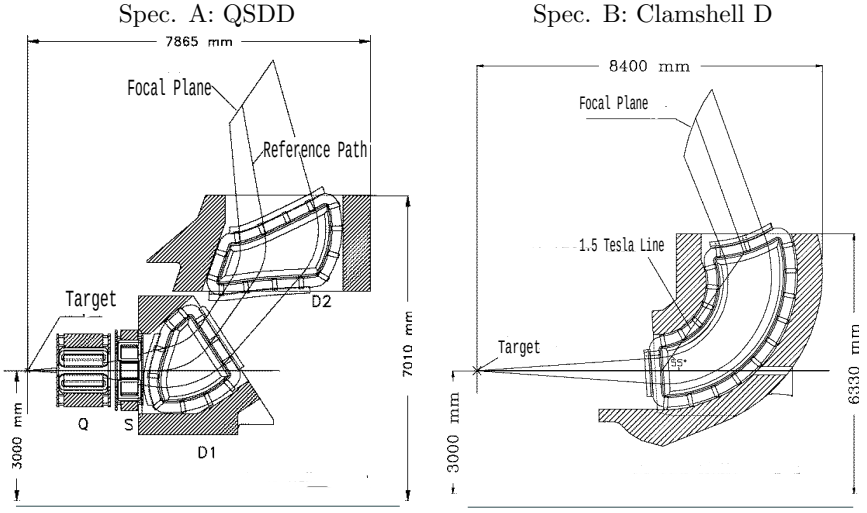

Figure 3.5: Schematic overview of dimensions and magnet positions in spectrometer A and B [61]. (Q: quadrupole magnet, S: sextupole magnet, D: dipole magnet)

3.2.2 Detector system

The three spectrometers are equipped with similar detector systems consisting of two double layers of vertical drift chamber, two scintillator planes and a gas-Cherenkov detector. The drift chambers are located in the focal plane of the spectrometers and are used for the reconstruction of the particle trajectory. The scintillators are used for triggering, particle identification and for time referencing. The Cherenkov detector is the last part of the detector through which the particles propagate. This gas detector distinguishes between pions (and heavier particles) and electrons. Figure 3.6 shows a schematic overview of all detector parts.

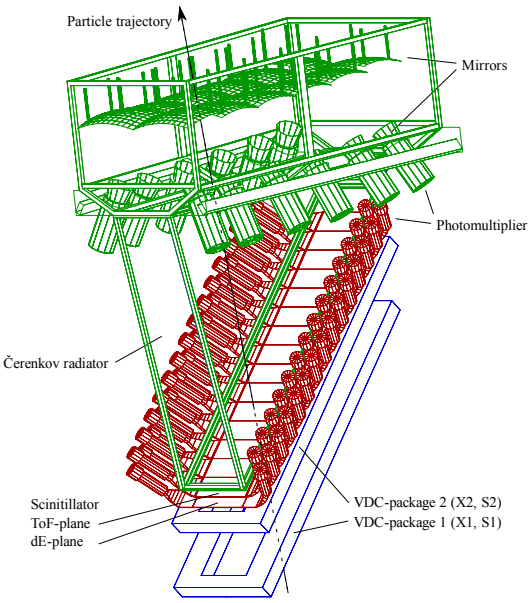

Figure 3.6: Schematics of all detector parts of the three spectrometers. The particles first pass the VDCs (blue), then the scintillators (red) and in the end the Cherenkov detector (green) [59].

Vertical Drift Chambers (VDCs)

The vertical drift chambers are utilized for the reconstruction of the particle trajectory inside the detector system. The focal plane is tilted by approximately 45° while being passed by the particles with an angle between 33° and 54°. Each VDC double layer consists of two individual VDC-planes, one with potential and signal wires perpendicular to the dispersive plane (X-chambers) and one with diagonal potential and signal wires (40° rotation, S-chambers). To not only gain an exact value for the position in the focal plane but also an exact value for the angle of the trajectory, two parallel double layers are used with a separation distance of 20 cm to each other. The spatial resolution of this configuration was determined to be better than 200 μm (FWHM[1]) in the dispersive and 400 μm in the non-dispersive direction.
A schematic view of a VDC is shown in fig. 3.7. Each VDC consists of a plane of alternating signal and potential wires with a pitch of 2.5 mm, sandwiched between two cathode planes of aluminized foil in 12 mm distance. The potential wires are directly grounded, while the signal wires have zero potential through the input impedance of the preamplifier electronics. The cathode planes are set to a potential of about -6 kV with respect to the wires. The VDC volume is filled with an argon-isobutane mixture with a small amount of ethanol. Passing charged particles generate electron-ion-pairs along their trajectory. While the ions drift to the cathodes, the free electrons are accelerated to the high field strength area around the wires, where the number of electrons is increased due to secondary collisions (gas amplification). When the electrons reach the signal wire the resulting current is detectable. Since the potential wires are thicker, the field strength is lower and no

[1] Full Width Half Maximum

sufficient gas amplification takes place close to them.
Already with one drift chamber it is possible to determine the position as well as the angle of the passing particle by using the relative time differences of the signals from each single wire (cf. fig. 3.7). By using more than one drift chamber in particularly the measurement precision of the angle is improved [62]. With the precise knowledge of the mapping characteristics of the spectrometer, which comes from dedicated optics calibration measurements, it is possible to determine the momentum of the particle and the vertex of the event from the track inside the spectrometer.
To achieve a good performance of the VDC, it is important that as many wires as possible are functioning. Too many non functional wires would worsen the efficiency of the track reconstruction. Prior to the experiment the status of the VDCs of all spectrometer was checked and in spectrometer C several non functional wires were found. The VDC layer containing these wires was dismounted and broken wires were repaired before the experiment started.
For a more detailed description of the VDC system, see [62] and [63].

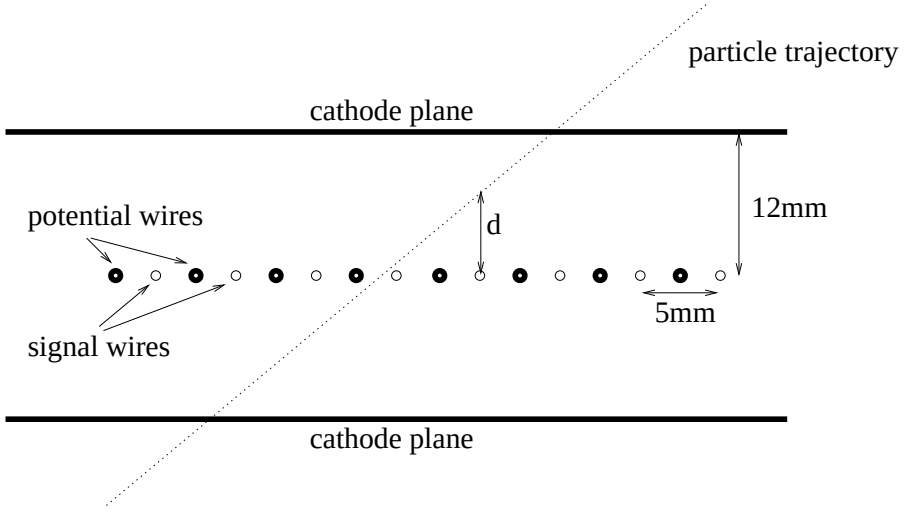

Figure 3.7: Schematic view of a single layer of the vertical drift chamber. Passing charged particles generate electron-ion-pairs along their trajectory. While the ions drift to the cathodes, the free electrons are accelerated to the high field strength area around the wires, where the number of electrons is increased due to secondary collisions (gas amplification). The different distances of the trajectory to each single wire, result in relative time differences of the signals. The trajectory is determined by a fit, for which the signals of all four wire chambers are considered.

Scintillators

The two scintillator planes are segmented (15 segments for A and C, 14 for B). Through segmentation the time resolution is improved and the segmentation furthermore allows for a rough position estimate of the particle track. The first plane (dE-plane, dE = change of energy) is 3 mm thick and is used to separate minimum-ionizing particles (electrons/positrons, pions) from protons or deuterons by measuring the specific energy loss in the scintillator material. The second plane (ToF-plane,

ToF = time of flight) is 10 mm thick and consists of a scintillator material with a faster time response behavior than the dE-plane. Normally, a coincidence between dE and ToF-plane is demanded for a trigger signal, with the ToF-plane as a reference for timing. Depending on the nature of the experiment the trigger logic can be switched to dE or ToF only. For this experiment ToF was used, since the efficiency of the dE layerwas not sufficiently high . How the efficiency of the scintillators was checked will be discussed in 3.4. For more details about the scintillator system see [64].

Cherenkov detector

The Cherenkov detector is realized as a gas detector and is used for the discrimination between electrons and heavier particles like pions. The detector volume is filled with $C_3H_2F_6$, in which propagating electrons or positrons with energies larger than 11 MeV produce Cherenkov light. For the application of the spectrometer as electron detector it is possible to separate electrons from pions and muons for the whole momentum acceptance range.

3.2.3 Target Chamber

The target system is enclosed in a vacuum scattering chamber located at the rotation axis of the spectrometers. Depending on the experimental conditions, different types of target materials need to be positioned inside the scattering chamber. Solid state targets are the easiest to handle at room temperature. A target ladder holds several interchangeable materials like graphite, tantalum etc. A luminescent screen (Al_2O_3 plate with a printed on cross) is always mounted on the ladder for visual beam position checks. For this experiment also an empty cell was installed on the ladder in order to measure the background. This empty cell was built especially for this experiment with the same dimensions as the cryogenic cell which is used for the deuterium measurement. Its walls are made out of HAVAR foil[2] with a thickness of 50 μm. It was used to measure the contribution of scattering at the walls. More details about this contribution is given in 4.4.
To choose one of the materials the whole ladder can be moved vertically by an electric motor which can be operated through a software in the counting room.
The lid of the barrel shaped scattering chamber can be exchanged for two different target constructs which are needed for experiments with gaseous and liquid targets: A high pressure gas target and a cryogenic target (see fig. 3.8). For the experiment described in this thesis the cryogenic target was installed and filled with deuterium[3] which was cooled down to be liquified. This was necessary to achieve a high density in the target volume.
The cryogenic target system consists of two loops. The inner loop ('Basel-loop',

[2]HAVAR consists mainly of cobald, chrome, iron, tungsten, molybdenum and manganese
[3]The deuterium has a purity of 99.7% and the sum of N_2, O_2, H_2O, DH and THC is less than 0.3% [65]

named after the place of its development: the University of Basel) is filled with liquid deuterium. The liquid is continuously recirculated by a fan.
To move the target cell inside the scattering chamber, the Basel-loop is attached to the lid. There a construct is located which allows to pivot the target out of the scattering point to make space for the target ladder.
There are different types of target cells that can be mounted at the position, where the electron beam hits the Basel-loop. In this experiment a round cell with a diameter of 2 cm was used. The wall of this cell is made out of 10 μm thick HAVAR foil. As already mentioned for the empty cell the scattering of electrons inside the walls results in background events which have to be subtracted in the analysis (see 4.4).
A heat exchanger couples the inner loop to the outer loop, which is coupled to a Philips-Stirling-compressor [66]. This compressor is liquifying the gas with a cooling capacity of about 100 Watt. The outer loop is filled with hydrogen and works like a heat pipe: The liquified hydrogen flows to the target, cooling down the target heat exchanger. The warmed up hydrogen evaporates and returns to the Philips-Stirling-compressor. More details on the heat exchanger can be found in [67].
The deuterium in the Basel-loop is subcooled to ensure that the electron beam load does not substantially change the density of the target material by local heating above the boiling point. Nevertheless, for higher currents the beam is rastered in the transverse directions to reduce the effective power density.

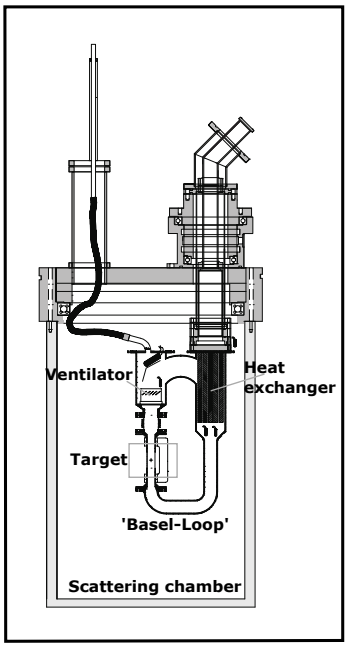

Figure 3.8: Schematics of the target setup installed in the scattering chamber. Figure from [68].

3.2.4 Picoamperemeter and beam position stabilisation

The standard device to measure the beam current at MAMI is a fluxgate magnetometer located within a part of RTM3 where all recirculations of the beam pass

through. With this setup the most accurate measurement can be done for the highest number of recirculations in RTM3, i.e. for a beam energy of 855 MeV. Since for this experiment beam energies 180 MeV, 315 MeV and 450 MeV were used, another way of measuring was necessary. This was especially required for the measurement at the 180 MeV setups, as for this energy the fluxgate magnetometer is not applicable.
For these measurements a picoamperemeter (pA-meter) at a collimator located right in front of the first linear accelerator segment was installed.
The beam can be deflected in the direction of the collimator and the resulting beam induced current can be measured. When the beam passes the collimator and is injected into the accelerator some of the beam current is unavoidably lost at this point. As a result an offset needs to be subtracted from the measured value for the current.
Since it is not possible to guide the beam towards the target and measure the beam current with the pA-meter simultaneously, the beam was automatically deflected to the collimator every 3 min for a short time period during each run of data taking. For these diagnostic modes called intervals the data taking was automatically stopped and restarted when the interval was over. The current at this early stage of the accelerator is basically the same as in the experimental hall, because any significant beam loss in the further accelerator stages (at the beam energies used in this thesis) would increase the radiation levels in the MAMI halls and there was no loss measured. To check this the measurements by pA-meter, fluxgate magnetometer and the luminosity measurements by the spectrometers were compared, for details see 4.5.
In [69] it was shown that a shift of the beam position on the target results in a drift of the measured cross section. For high beam energies the beam is stabilized by the circulation in RTM3, which dampens beam position changes introduced in the earlier stages of the accelerator. For lower recirculation numbers this self-stabilization gets less effective. In the case of the incident beam energy of 180 MeV this stabilization is absent, since the beam bypasses RTM3. To monitor the position of the beam at the target a beam position stabilization module was installed by the MAMI group: Two cavities in front of the target are used to measure the beam position. According to the digitized signal of these cavities a correction current for the dipoles, which are steering the beam, is generated. For adequate sensitivity these cavities need high beam currents. Since for the experiment quite small beam currents were used, the beam had to be switched to a diagnostic mode, in which the beam is modulated with high current pulses with a very low duty cycle. For this purpose every three minutes the data acquisition was stopped and the beam switched to the diagnostic mode. During this time the beam position was checked and the pA-meter was used to measure the current.

3.3 Measuring program

The measurements were performed in March 2014. In three weeks of beam time 180 different settings were measured for the deuterium target as well as for the corresponding empty cell. The empty target settings are essential for the background subtraction in the analysis.
The kinematic setup for an scattering experiment can be completely described by any two parameters of the set (ϵ, Q^2, E, E', θ). Since the form factors depend only on Q^2 and the relative electric and magnetic contributions to the cross section are weighted by ϵ, the most convenient combination for the analysis is Q^2 and $\epsilon = \left(1 + 2(1+\tau)\tan^2\frac{\theta_e}{2}\right)$ with $\tau = \frac{Q^2}{4M^2}$. The accessible region for the kinematic setups is defined through the accelerator and the properties of the detector system. Figure 3.9 shows the accessible region for an experiment with spectrometer A. The lower boundary of the accessible Q^2 region is set by the lower limit on the incident beam energy (180 MeV, dark green line and area). Correspondingly the upper end is set by the maximum incident beam energy. The red line in fig. 3.9 shows the limit for maximum MAMI B energy (855 MeV).
The ϵ region is limited by the minimum and maximum scattering angle possible to reach with spectrometer A (23° and 160°). The excluded regions are marked in dark and light blue.
Spectrometer A has a maximum central momentum of 630 MeV/c. This excludes measurements at higher beam energies and forward angles (gray area).
The angular acceptance of spectrometer A is a bit wider than ±4°, thus a spacing of 2° between the settings gives about 50% overlap to allow checks for systematic errors.

Beam energies can be provided by the accelerator in discrete levels of energy in 15 MeV steps. The change of energy is quite time consuming (around six hours). Due to this reason a few fixed beam energies were selected. Since this experiment focuses on the extraction of the A(Q^2) form factor at low Q^2 the lowest possible beam energy of 180 MeV is essential. The other two beam energies (315 MeV and 450 MeV) were selected in equidistant intervals and will be used to constrain the normalizations and to check the contributions of the magnetic form factor. Because of the limited number of beam time hours a measurement with a broader range of energies was not possible.
The energy change of the accelerator is not the only time consuming part in the setting change, changing of the field in the spectrometers also takes a significant amount of time (around 45 min). Owing to this, the momentum was not adjusted for each new angle in order to keep the elastically scattered electrons at the same place in the focal plane.
The cross section data is expected to be most sensitive to the charge radius of the deuteron in the region below 1 fm^{-1} ($Q^2 < 0.04$ GeV^2), which is well covered by the chosen kinematics. The chosen settings for spectrometer A are depicted as black dots in figure 3.9.

Since all three spectrometers were used in each setting, the best possible combination of angles at which the spectrometers were measuring needed to be found. Besides

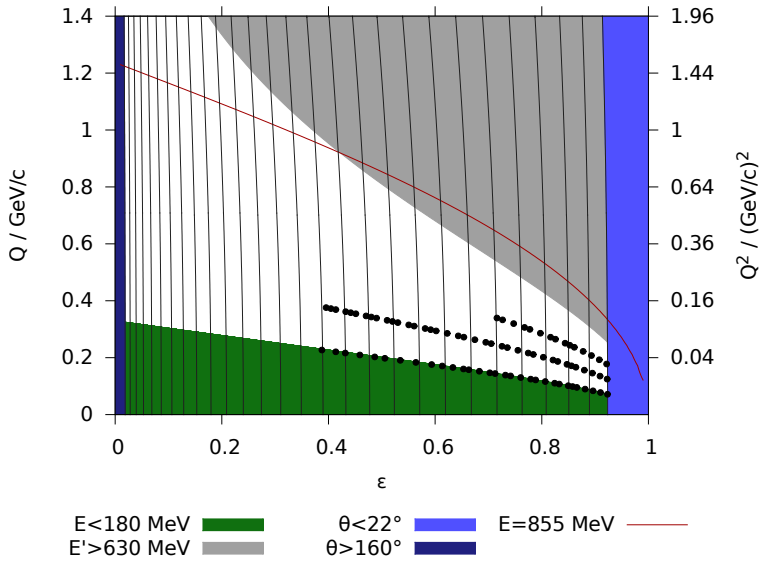

Figure 3.9: The accessible kinematic region in ϵ/Q space. The colored lines and areas show the limits of the facility: The red line represents the MAMI B limit of 855 MeV and the dark green line the limit for low beam energies. The dark (light) blue shows the kinematic region excluded from measurement due to the maximum (minimum) possible spectrometer angle. The grey shaded area is excluded by the upper momentum of spectrometer A. The black dots show the points at which the measurement took place. [70]

the geometrical constraints, like the minimum distance between spectrometer A/B and the exit beam line and between spectrometer B and C, it has also to be taken into consideration that the fringe fields of the quadrupole magnets in spectrometer A and C posses an influence to the particle trajectories detected with spectrometer B (this is described in [71]). To avoid these influences efficiently, the spectrometers always had at least a spacing of 50° to each other. All measured angles for both targets are depicted in figure 3.10 and all settings can be found in table A.1 in appendix A.

For all energies the smallest angle was 15.1° which was measured by spectrometer B. At the largest measured angles (in this experiment up to 107°) spectrometer C was located. Since spectrometer C was mainly used as a luminosity monitor, it was only set to a few different angles. Spectrometer A and spectrometer B were moved for each new setting in 1-2° steps at forward angles. For larger angles the steps were increased (up to 3°).

3.4 Calibration

Prior to the form factor determination an investigation of parameters concerning the data had to be performed to ensure that the later extracted values of the form factor are not biased by external influence. The stability of the spectrometers' magnetic fields, the performance of the detectors and the density of the deuterium inside the target had to be investigated.

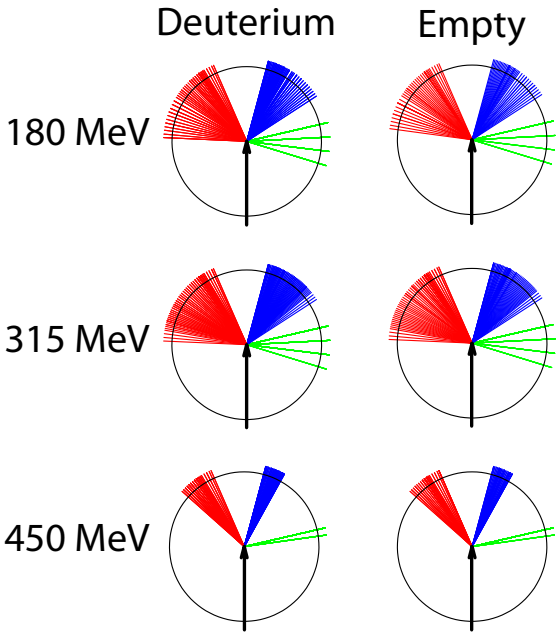

Figure 3.10: Kinematic settings for deuterium and empty target. The colored lines indicate the measured angles for each spectromter. (spectrometer A: red, spectrometer B: blue, spectrometer C: green).

Density of liquid deuterium

The density of the target material inside the target cell is a parameter which had to be monitored during all of the data taking. In the course of the experiment the pressure and the temperature of the deuterium inside the target cell were measured at multiple times during each run in order to obtain their mean values. Assuming a mix of liquid and gas, the density calculation can be performed routinely by using the program *liquidDensity*. But since in this experiment the liquid was undercooled, meaning that there is a liquid without a gaseous state, the actual state of the liquid target does not match the criteria of the calculations. Because of this reason the mean temperature has to be corrected before the density can be calculated. To get the corrected temperature value, the difference from the gas pressure curve (when the target was heating up) for all pairs of temperature and pressure is calculated. A temperature interval can be found for which this difference is nearly constant. For this interval a linear fit is performed, which is then used to calculate the corrected value:

$$\text{Correction} = a - b \cdot \text{MeanTemp}_{\text{pre}} \tag{3.1}$$

$$\text{MeanTemp}_{\text{corr}} = \text{MeanTemp}_{\text{pre}} - \text{Correction} \tag{3.2}$$

The temperature and pressure values before and after the correction as well as the gas pressure curve from the National Institute of Standards and Technology (NIST) for deuterium are shown in fig. 3.11 [72]. The corrected values are in good agreement with the NIST data. With the corrected value for the temperature and the pressure the program was used to determine the correct density in the target cell. This

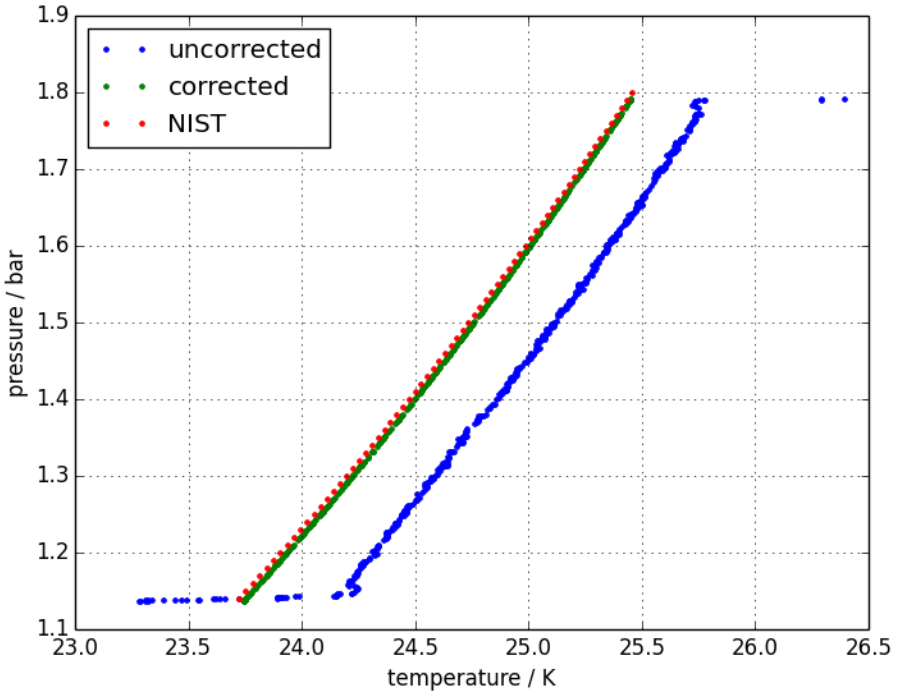

Figure 3.11: Gas pressure curve from NIST (red) in comparison to the values from the experiment. The blue curve shows the values before the correction and the green curve the corrected values. These are in good agreement with the NIST data.

calibration showed that there were only very small density fluctuations during the entire experiment (see fig. 3.12).

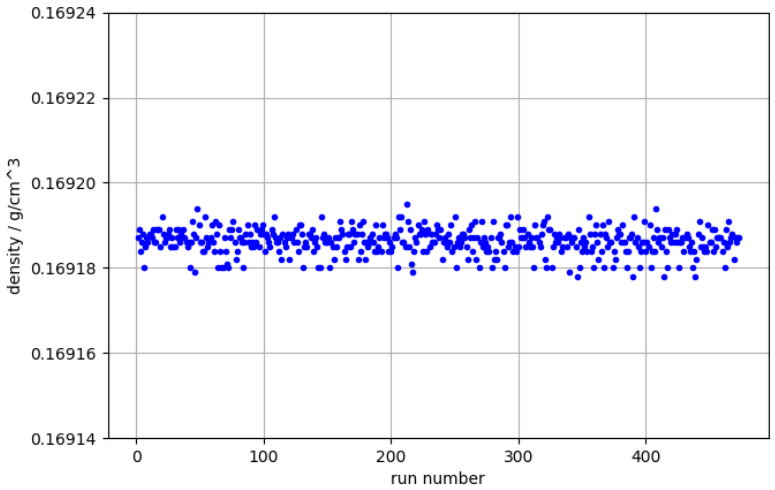

Figure 3.12: Density for each run. There were only small density fluctuations during the entire experiment.

Central momentum calibration

Matching the positions of the elastic peak in the experiment and the simulation is an important part of the analysis. If they do not match, the cut in $\Delta E'$ (see 4.3.2) would fail to select the equivalent part of the peak region in both the experiment and the simulation. $\Delta E'$ is the difference of the detected energy to the energy calculated from the detected scattering angle. This quantity is used to identify the elastic reaction, since the distribution of $\Delta E'$ shows a peak near zero for the elastic events. The peak position is given by the relative momentum, which is in first order determined by the focal plane coordinate x (for description of coordinate systems see 3.2) and by the absolute momentum of the reference trajectory, that depends on the magnetic fields of the spectrometer magnets. To measure the magnetic field each spectrometer is equipped with Hall probes and a Nuclear Magnetic Resonance (NMR) system, which is more precise than the Hall probes and whose signal does not drift due to radiation damage or temperature fluctuations. The inhomogeneities of the field at the position of the probe must be below a certain level, to be able to measure the field strength with the NMR system, otherwise no resonance can be found. This is fulfilled by design for spectrometer A and C, although not for B, where correction coils are employed to suppress inhomogeneities caused by the clam shell design.
During data acquisition the NMR values from which the values for the central momentum can be derived were read out frequently, typically once for each 30 minutes run. To get the right peak position in simulation and experiment the correct momentum for each run has to be inserted into the run database (*run.db*). Since the

pairs of momentum and NMR values can show deviations from the expected relation to each other, the values were fitted with a cubic polynomial function (see fig. 3.13) before writing the momentum values the database.

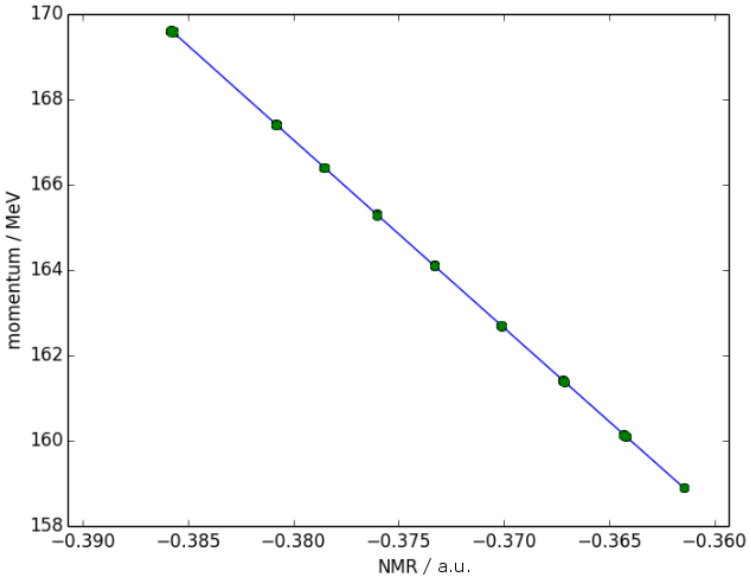

Figure 3.13: Fit of momentum and NMR values. The momentum values were then used for the simulation.

Scintillator efficiency

The knowledge of the scintillator efficiency is also essential to the analysis. Usually the efficiencies are in the order of $\approx 99\%$ or higher. In the case of an efficiency lower than 99%, a correction has to be applied to the cross section data. Since the ToF scintillator layer was used for triggering during the experiment, the dE layer was utilized to measure the efficiency of the ToF layer. For this purpose, dedicated efficiency runs were performed during the beam time. For these runs the trigger was set to trigger on the dE scintillators. The efficiency was calculated as the number of events where ToF and dE layer had provided a trigger signal divided by the totality of all events.
Due to the reason that the efficiency can be different for the different scintillator bars, the efficiency corrections can not be applied as a global factor, but have to be calculated for each part of the scintillator and applied accordingly. To do this the reconstructed position of the electrons in the scintillator plane, which is determined by the vertical drift chambers, is used. Using this position the scintillator plane is being sectored in multiple bins in both directions (x_{scint}, y_{scint}), see top left plot in fig. 3.14 and fig. 3.15. The efficiency is estimated in each of these bins and corrected accordingly.
To apply the efficiency correction in `Cola++` (see chapter 4) to the experimental rates a so called *.col* file is used. In this file first the scintillator bin in which the event

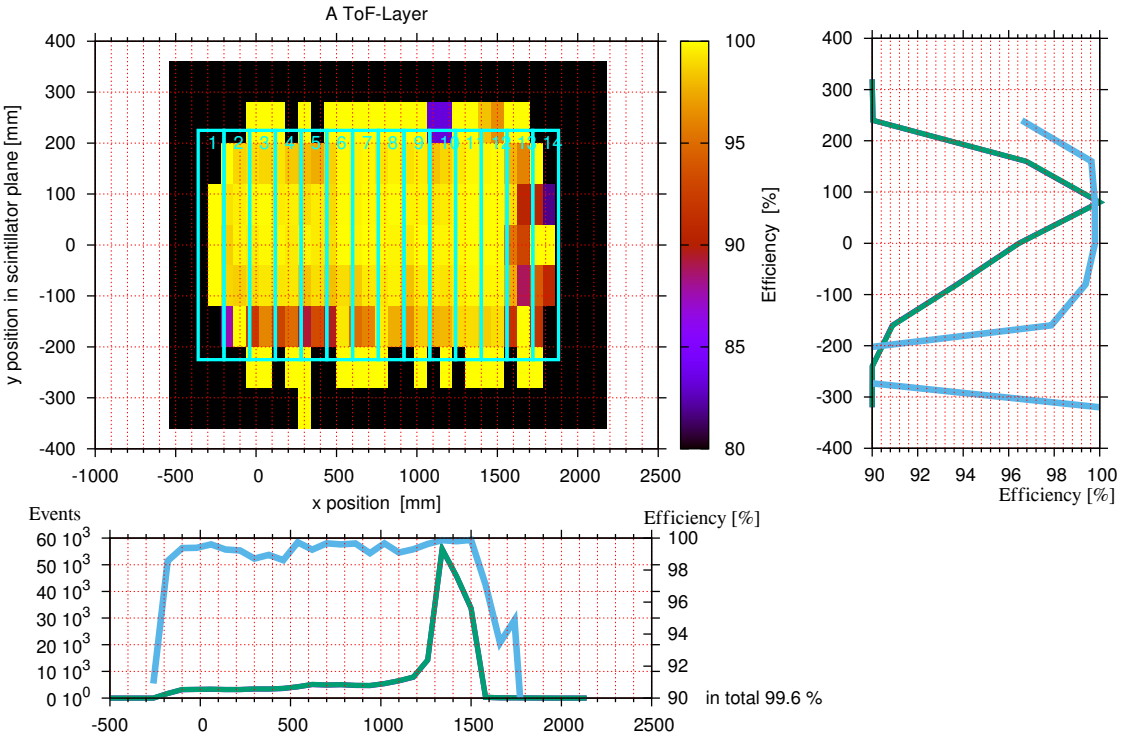

Figure 3.14: Efficiency plot before the correction. In the 2d plot the efficiency distribution over the whole ToF layer is shown. The blue, numbered rectangles are the scintillator bars. The plots on the right and below that plot show the projections of the efficiency to the x and y axis of the scintillator plane (blue lines) and the distribution of events for this specific efficiency run (green lines).

falls is found. After that, the weight, which is the inverse of the efficiency measured in this bin, is calculated. This weight is there upon used as a multiplicative correction factor.
In fig. 3.14 the efficiency distribution over the whole ToF layer of spectrometer A is shown. The blue, numbered rectangles are the scintillator bars. The plots on the right and below that plot show the projections of the efficiency to the x and y axis of the scintillator plane (blue lines) and the distribution of events for this specific efficiency run (green lines). Figure 3.15 shows the same plot, yet with an applied correction. As a result the efficiency is now more uniform over the whole scintillator layer, which can be seen at the more uniform distributed yellow area in the top left plot and the higher efficiency (blue line) in the plots on the right and below the 2d plot.

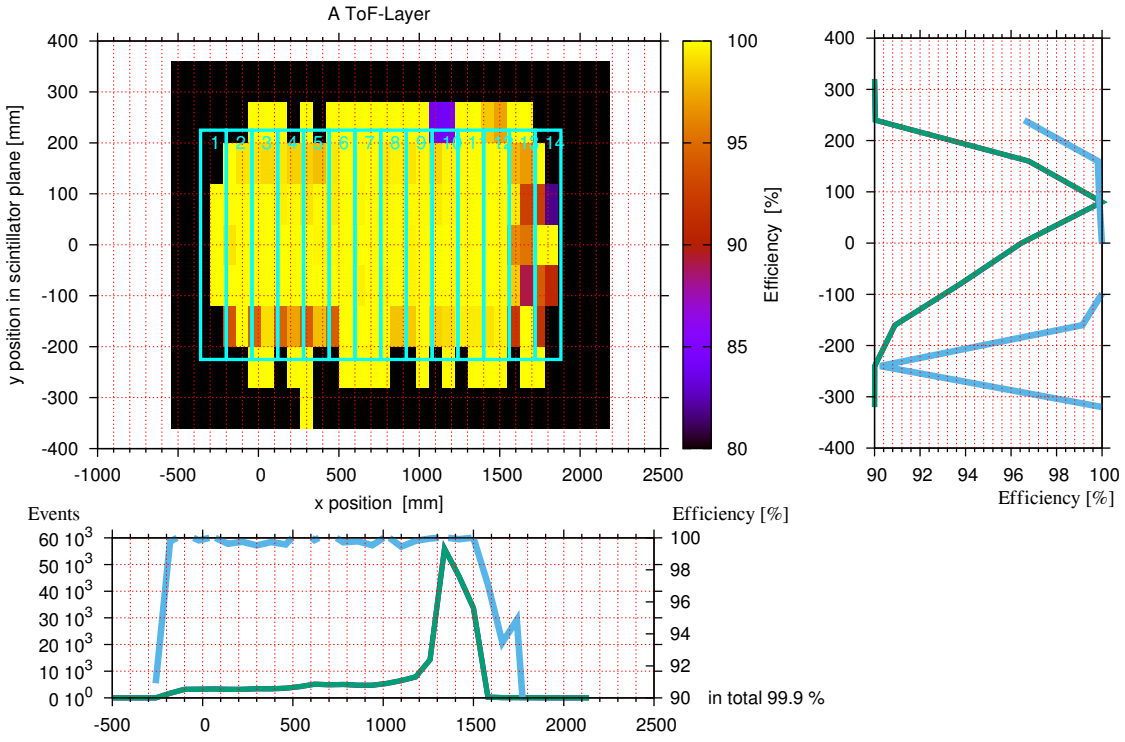

Figure 3.15: Efficiency plot after the correction. In the 2d plot the efficiency distribution over the whole dE layer is shown. The blue, numbered rectangles are the scintillator bars. The plots on the right and below that plot show the projections of the efficiency to the x and y axis of the scintillator plane (blue lines) and the distribution of events for this specific efficiency run (green lines).

VDC calibration

For the calibration of the VDC different steps have to be done.
Broken wires had to be excluded from the analysis. This was achieved by manually checking overview plots for wires with very low efficiency or high noise. Those few broken wires were disabled for the analysis by flagging them with the corresponding

entry in the run-database.
The next step is to differentiate between good events and δ-electrons[4], also noisy wires can be detected with this method. For this differentiation the drift time difference criterion is used. The timing difference between signals in neighboring wires provides information about the kind of event the VDC recorded. This is schematically shown in fig. 3.16. The vertical lines represent the drift length and therefore the time it took the signal to arise after a particle passed through the VDC. Since there is only the timing information and no information about from which side the particle entered the chamber, the vertical lines go in both directions. For a good event the time it took the signal to arise is smallest for one wire and increases for the neighboring wires. The signal for a *delta*-electron has a decreasing time difference for neighboring wires. For very noisy wires the neighboring wires usually produce no signal. So it is possible to filter out everything but the good events. Since the x- and s-wires of the VDCs have different geometries (see 3.2.2),

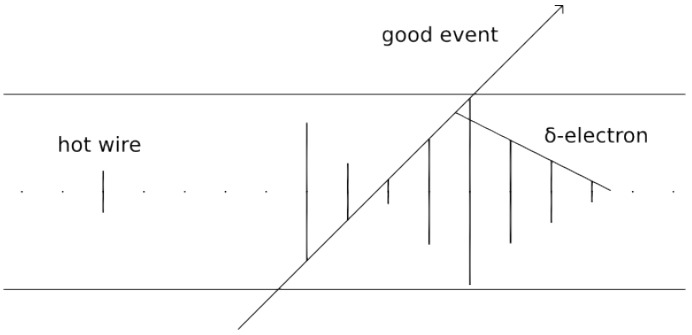

Figure 3.16: Illustration of the time differences of different kinds of events in the VDC. The dots in the middle represent the wires and the vertical lines the time it took the signal to arise after a particle passed through the VDC.

the mean multiplicity is smaller for the s-wires than for the x-wires. The selection is controlled via run-database parameters, which can have the value 1 or -1. Here 1 means that all events with the wrong timing difference to neighboring wires are removed. This means that tracks produced by δ-electrons and effects of hot wires are removed. For -1 events in which only one wire gave a signal are not removed.
Also the cut conditions for the timing difference are controlled by run-database variables. See fig. 3.17 as an example how to obtain the values. The figure shows the time differences for each wire. The pink lines need to be as closely as possible around the bulk of events to mark the minimum and the maximum time differences. The slope of the lines is m.
Subsequently for the VDC calibration is to adjust timing offsets, the drift time and the drift velocity inside the gas chambers:

- The drift velocity is set for the analysis with the run-database variable VDC.Driftvelocity, it is almost constant, but especially after an exchange of the gas bottle it tends to change. This velocity is needed for converting the measured drift times into a distance, which then is used for the track reconstruction.

[4] δ-electrons are created when ionizing radiation has enough energy to loosen electrons out of the surrounding matter. They are secondary particles.

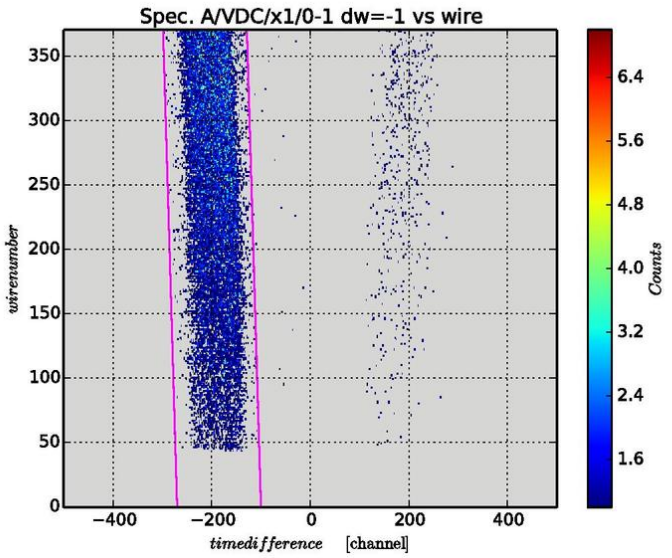

Figure 3.17: Time difference for each wire. The pink lines mark the minimum and the maximum time differences.

- The drift times are measured by a TDC[5], for each VDC plane a different TDC crate is used.
- Due to small differences in signal processing times in the electronics, each wire might have a different timing offset. These are hard coded in the analysis software and should be constant.

Base for the optimization of these values is the goal to minimize the errors of the reconstructed track in the VDC. Under the assumption that variations on the x-plane parameters mainly affect the quality of focal-plane x-coordinates and the dispersive angle, and variations on the s-plane parameters mainly affect the focal-plane s-coordinates and the non-dispersive angle, the reconstructed track errors were minimized in an iterative process. The final values were entered in the run-database.
In fig. 3.18 the drift velocities for all deuterium and empty cell runs are shown. It can clearly be seen that the first exchange of the isobutane bottle changed the drift velocity in all chambers significantly. This is probably due to impurities in the gas bottle. Already in other A1-beamtimes [71] it had been observed that the gas bottle exchange is correlated with the change of the drift velocity for a certain amount of time.

[5]Time to Digital Converter

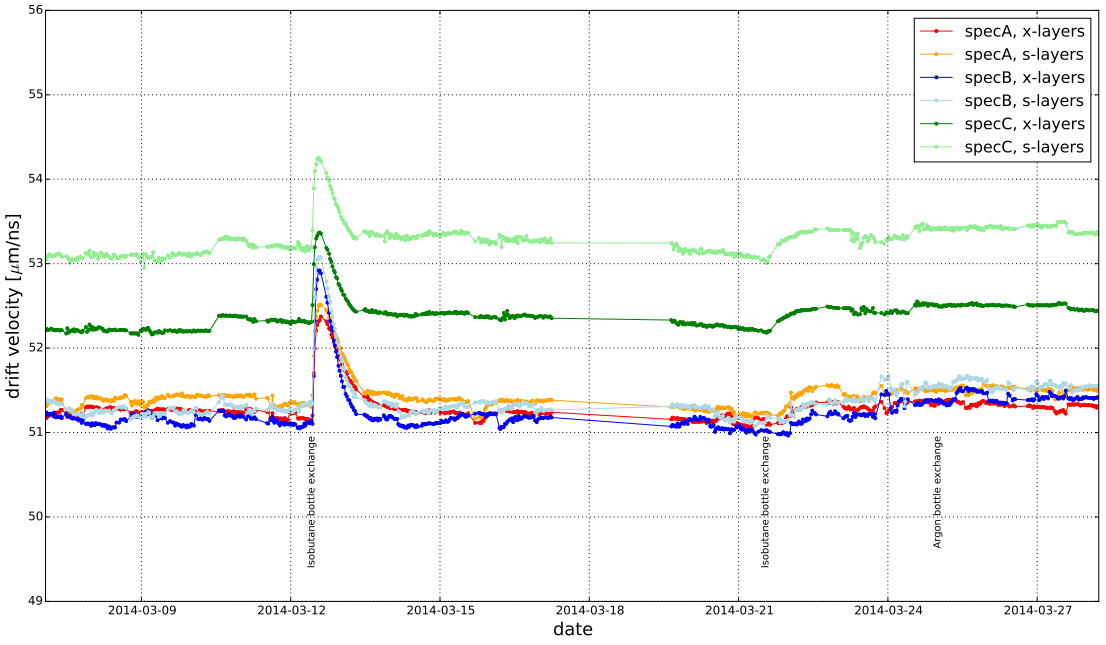

Figure 3.18: Drift velocity for all VDCs in all three spectrometers.

4

Data Analysis

This experiment aims at measuring the elastic electron deuteron cross section in the kinematic region accessible with MAMI to extract the form factor and determine the deuteron charge radius. The cross section is determined relative to the cross section implemented in the simulation by comparing the measured count rate for the given spectrometer acceptance with the result of the simulation. The simulations needed for this analysis are the simulation for the electron-deuteron scattering (4.1) and the simulation of the cryogenic depositions around the target cell (4.2). While analyzing the deuteron data also the target background has to be analyzed (4.4) and the luminosity (4.5) needs to be determined before the fit of the form factor can be performed (4.6).

For the data analysis a software package was used to handle the analysis of the A1 data, which was developed by the A1 collaboration. This package is called `Cola++`[1]. It reads the raw spectrometer data and determines the tracks of the scattered electrons in the VDCs. Afterward it applies the transfer matrices to calculate the scattering and azimuthal angle, the momentum and the scattering vertex of the electron with respect to the beam axis. Another A1 software package (`Lumi++`) was used to determine the dead-time of the spectrometers. For the simulation a third package (`Simul++`) was used. That package handled the simulation of the cross section and acceptances for the interactions of electrons with deuterium, HAVAR, nitrogen and oxygen among others and is described in sections 4.1 and 4.2.

4.1 Simulation of electron - deuteron scattering

A simulation has to mimic the behavior of a real experiment as precise as possible. For this, the kinematics, which were used in the experiment, need to be generated, from these the cross sections have to be calculated. Since in the experiment also radiative corrections contribute to the measured cross sections (see section 2.2.2), these corrections have also to be applied in the simulation. After all these steps histograms similar to the ones for the experimental data are filled, which are then used for the comparison of data and simulation in the analysis.
The simulation for this experiment calculates the cross section for an electron scattering on a deuteron as well as the needed corrections described in 2.2. It also

[1] Cindy OnLine Analysis in C++ [73]

models the energy losses of electrons traversing the target cell (see also appendix C) and the spectrometer. The acceptance of the spectrometers is also included in the simulation.
The generator for the elastic electron deuteron scattering simulation is *generateElasticDeuteron*. Depending on the generator flag, which needs to be set in the run database, the generator will create events with different kinds of radiation corrections. For this analysis the flag with the best available radiation corrections was used. This includes the internal Bremsstrahlung as well as the radiative corrections on the electron side and the structure independent ones for the hadron side, respectively [53].
The simulation starts with generating the incoming electron beam. The energy of the beam is known from the accelerator data and is provided to the simulation by a run database variable. For generating a scattering vertex in the target cell a model of the cell was implemented (see also appendix C). The round cell consists of a wall made out of HAVAR foil confining the deuterium (3.2.3). The details of the applied energy losses can be also found in 3.2.3. Adding a layer of cryogenic depositions on the HAVAR foil is also possible. Besides a vertex position also a scattering angle as well as an azimuthal angle are generated pseudo-randomly. After applying the energy losses in the target cell the cross section for the scattering process was calculated.
The generator of the radiative corrections can be split in two parts: the electron contribution and the hadron contribution.
For the electron contribution the calculations of Vanderhaeghen *et al.* [53] are followed (see also 2.2.2). The part of the radiative correction δ which gives rise to the radiative tail is[2]

$$\delta\left(\Delta E_S\right) = \frac{\alpha}{\pi} \ln\left(\frac{\left(\Delta E_S\right)^2}{E_e \cdot E_e'}\right)\left[\ln\left(\frac{Q^2}{m^2}\right) - 1\right] \tag{4.1}$$

There are two terms for the hadron contribution that contribute to the radiative tail (cf. 2.2.2). They are contained in δ_1 (eq. 2.22) and δ_2 (eq. 2.24).
The part of the radiative corrections which is responsible for the radiative tail was included by sampling the according distributions of $\Delta E'$ within the generator [53] which leads to the correct shape of the tail.
After the scattering process energy losses due to Bremsstrahlung and multiple scattering of the scattered electron on the way from the scattering point to the spectrometer were applied. The result of all the calculations for the cross section, the corresponding energy losses and the radiative corrections was the four - vector of the scattered electron as well as the weight for the event determined during the cross section calculation. These results were then used for the further analysis, where cuts were applied on certain parameters to enable the comparison of data and simulation.

[2] As in 2.2: E_e: incoming electron energy, E_e': energy of the scattered electron, Q^2: momentum transfer, ΔE_S: maximal energy of emitted photon in c.m. system of recoiling deuteron and photon, $\Delta E' = (E_e'^{el} - E_e')$: cut-off engery, $E_e'^{el}$: elastic scattered electron lab energy

4.2 Simulation of the cryogenic depositions around the target cell

The simulation of the elastic scattering of electrons on deuterons is not the only important simulation for this analysis. Left-over air in the volume around the cryogenic target cell causes a contribution to the background events by electrons scattered at frozen oxygen and nitrogen (see 4.4 for more details). Since it is not possible to measure this background on its own (without HAVAR cell and deuterium) the only reasonable possibility to describe it, is to simulate the electron scattering on these elements.
To model the cross sections for oxygen and nitrogen the Mott cross section eq. 2.6 multiplied by an appropriate form factor was used [74]. For oxygen the form factor was approximated by Helm's model [75], which is a simple model to parametrize form factors of heavy nuclei. It is a convenient way to parametrize a charge distribution as a convolution of a homogeneously charged sphere with radius R ($\varrho_{\text{h.s.}}$) and a Gaussian distribution with variance σ (ϱ_{G}):

$$\varrho_{\text{H}}(r) = \varrho_{\text{h.s.}}(r, R) * \varrho_{\text{G}}(r, \sigma) \tag{4.2}$$

The main advantage of Helm's model is that the form factor $F(q)$ for the resulting distribution is given by the product of the Fourier tranform of $\varrho_{\text{h.s.}}$ and ϱ_{G}:

$$F_{\text{H}}(q) = F_{\text{h.s.}}(q) F_{\text{G}}(q) \tag{4.3}$$

For more details and the values of R and σ see [75].
For nitrogen a form factor model was used, which is described in detail in [76]. In this model the form factor is written as

$$F^2\left(q^2, \theta\right) = F_L^2\left(q^2\right) + \left(\frac{1}{2} + \tan^2\left(\frac{\theta}{2}\right)\right) F_T^2\left(q^2\right) \tag{4.4}$$

where the form factors $F_L^2\left(q^2\right)$ (longitudinal or Coulomb term) and $F_T^2\left(q^2\right)$ (transverse term) are functions of q^2 only and can be decomposed into several multipole contributions according to the selection rules and the transitions. Generally they are written as

$$F_L^2\left(q^2\right) = \sum_{\lambda=0}^{\infty} F_{C\lambda}^2\left(q^2\right) \tag{4.5}$$

$$F_T^2\left(q^2\right) = \sum_{\lambda=1}^{\infty} \left(F_{E\lambda}^2\left(q^2\right) + F_{M\lambda}^2\left(q^2\right)\right) \tag{4.6}$$

In fig. 4.1 a comparison between nitrogen data and the model given in eq. 4.4 is shown [76]. The simulations for nitrogen and oxygen are more basic than the one for deuterium. The events are generated such that they appear only at the location of

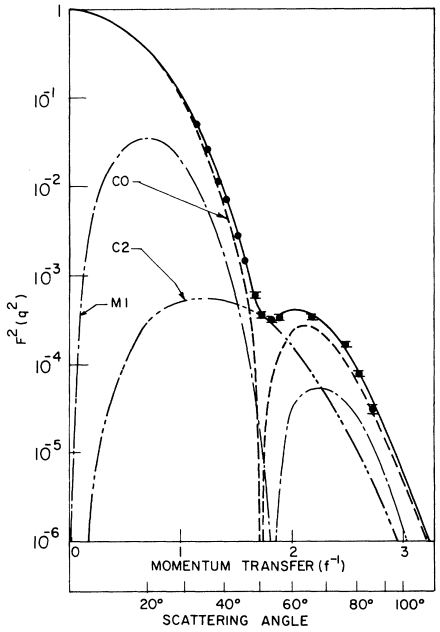

Figure 4.1: Fit to elastic scattering on N^{14} data at 400 MeV beam energy. The sum of monopole (C0) and electric quadrupole (C2) terms corresponds to F_L^2 in eq. 4.5 and the magnetic dipole (M1) term corresponds to F_T^2 in eq. 4.6. These contributions are shown in different dashed lines. The solid line is the total result of the three terms [76].

the cryogenic depositions. The simulation does not include excited states of nitrogen and oxygen since there are no calculations for this available. The calculation of the energy loss of the electron inside the target cell is explained in appendix C.
It could be possible that also excited states of nitrogen and oxygen contribute to the measured spectrum. If there are any contributions of this, they should be visible in a 2 dimensional histogram, where the energy of the scattered electron (E') is plotted versus the scattering angle. Such a histogram can be seen in fig. 4.2. The declining line in the lower part of the plot is caused by electrons which are scattered at the deuterons. The nearly horizontal lines in the top of this plot are caused by the electrons which are scattered elastically at the nuclei of the HAVAR wall and the cryogenic depositions. If there were any contributions by excited states at the cryogenic depositions in the region of the deuteron peak, they should appear in this plot as lines with less slope than the deuteron line at roughly the same E'. Since there are no such lines visible (all kinematics have been checked), these contributions are neglected in this analysis.

4.3 Data processing

The detector information stored in the raw data files is interpreted and analyzed. In a single-arm experiment, the main tasks are:

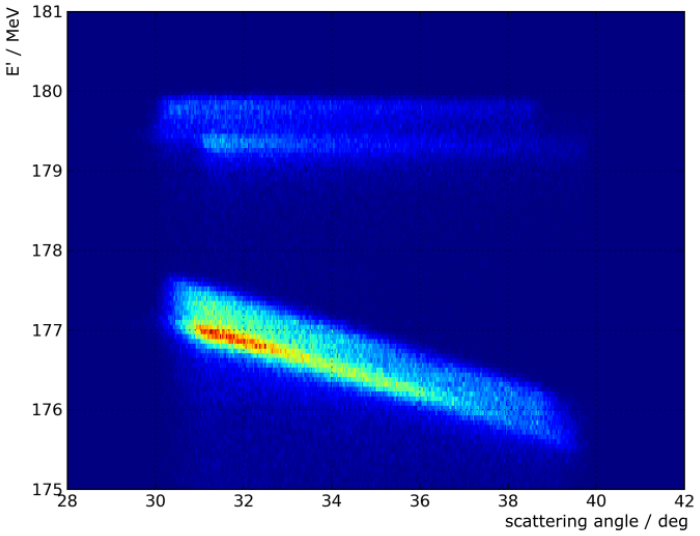

Figure 4.2: Energy of the scattered electrons (E') versus the scattering angle. The declining line in the lower part of the plot is caused by electrons which are scattered at the deuterons. The nearly horizontal lines in the top of this plot are caused by the electrons which are scattered elastically at the nuclei of the HAVAR wall and the cryogenic depositions. If there were any contributions by excited states or quasi-elastic scattering at the cryogenic depositions in the region of the deuteron peak, they should appear in this plot as lines with less slope than the deuteron line at roughly the same E'.

- Calculate the particle trajectories in the detector system from the VDC information.
- Transform these trajectories using transfer matrices to the particle coordinates at the target. These matrix elements are polynomials and they emulate the magnetic properties of the spectrometer. The result after their application are the properties of the particle after the scattering process at the scattering vertex in the target, such as direction, vertex position and relative momenta of the particles (see also 4.3.1).
- Calculate derived properties and fill histograms accordingly.

Besides the events from elastic electron deuteron scattering one is interested in, the detector system also records background events and random triggers from cosmic rays. To minimize background and erroneous trajectories, cuts have to be applied, which is described in 4.3.2.

4.3.1 Transfer matrices

The transfer matrices are used for the reconstruction of the particle momentum and the interaction point. These are determined by dedicated calibration measurements with sieve-slit collimators and movable thin targets (see [77] for details). The matrices are different for different central momenta of the spectrometers, this is mostly

based on the inhomogeneity of the fringe fields of the magnets.
In essence, the functional dependence of a target coordinate $t_i \in \{\theta, \phi, y_0, \Delta p\}$ is described by a polynomial expansion in terms of the detector focal plane coordinates $f_j \in \{\Theta_0, \Phi_0, X, Y\}$:

$$t_i = \sum_a \sum_b \sum_c \sum_d M_{abcd,i} f_1^a f_2^b f_3^c f_4^d, \tag{4.7}$$

under the assumption that the perpendicular beam coordinates are zero (or known). For this analysis standard matrices which have already been used for other experiments in the A1-collaborations have been used.

4.3.2 Event identification

Electrons scattered elastically without the emission of a real photon carry the energy

$$E'(\theta) = \frac{E}{1 + \frac{E}{m_d}(1 - \cos\theta)}. \tag{4.8}$$

Ionization as well as external and internal Bremsstrahlung reduce the energy of the detected electron. To identify the elastic reaction, the difference of the detected energy E'_{exp} to the energy calculated from the detected scattering angle $E'(\theta_{\text{exp}})$ is defined as

$$\Delta E'_{\text{exp}} = E'(\theta_{\text{exp}}) - E'_{\text{exp}}. \tag{4.9}$$

The distribution for $\Delta E'_{\text{exp}}$ shows a peak near zero, with the radiative tail at higher values of $\Delta E'_{\text{exp}}$. The radiative tail largely overlaps with the distribution for the break-up of the deuteron, which starts around 2 MeV (see fig. 4.3). A cut around the elastic peak down to a cut-off energy $\Delta E'$ selects the elastic reactions and gets rid of the break-up events. The extent of the detector plane defines the momentum acceptance of the spectrometer. Since it is difficult to control the efficiency at the edges of the detector plane, the uppermost and lowermost accepted momenta are cut out. The variable to which the momentum cut is applied is Δp_c, the deviation of the particle momentum from the central momentum. Cuts on out-of-plane (Θ_0) and in-plane (Φ_0) angles were applied to reduce the background. The cuts are summarized in tab. 4.1, the effect of the cuts on the $\Delta E'$-histogram can be seen in fig. 4.3. For spectrometer B one additional cut was necessary, when particles hit the long entrance flange of spectrometer B, which is located in front of the collimator, they may be scattered back into the acceptance. These particles are easily identified by the horizontal component (y_{flange}) of the intersection of the particle trajectory and the plane of the entrance of the flange. The two dimensional histogram of y_{flange} and the horizontal offset at the collimator y_{colli} is shown in fig. 4.4. Around $y_{\text{flange}} = 0$ the good events are located. The events in the side bands above and beneath these are

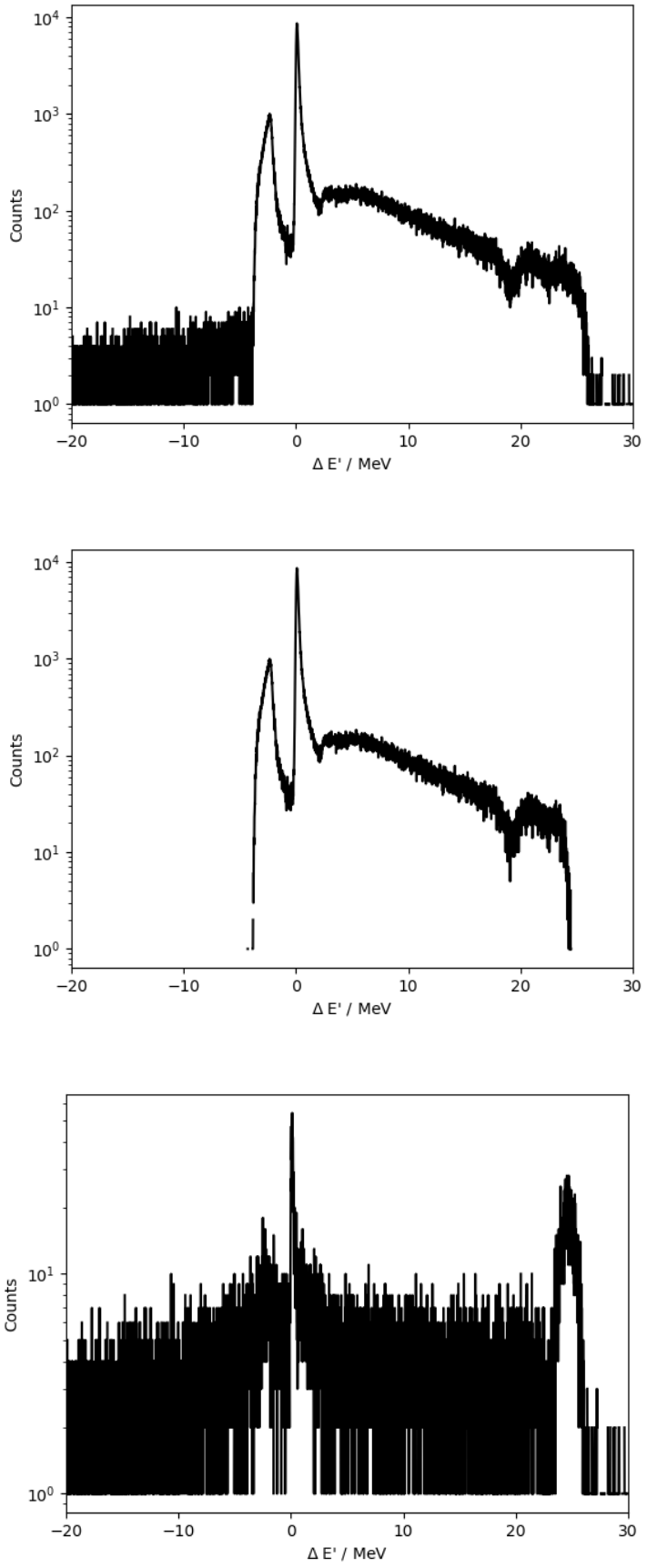

Figure 4.3: ΔE' plots of a run with spectrometer A at 35° with 180 MeV beam energy. Top: spectrum without any cuts. Middle: After applying all cuts from tab. 4.1. Bottom: Rejected events. Most of the rejected events are random events. The bump around 25 MeV are events detected near the edge of the detector plane.

Cut	Spec. A	Spec. B	Spec. C
$\lvert\Delta p_c\rvert$	$-10\% < \Delta p_c < 9\%$	$< 7.3\%$	$< 12.3\%$
$\lvert\Phi_0\rvert$	$< 6.5°$	$< 3°$	$< 6.7°$
$\lvert\Theta_0\rvert$	$< 5°$	$< 3°$	$< 6.5°$
$\lvert y_{\text{flange}}\rvert$	-	< 30 mm	-

Table 4.1: Cuts used in the analysis.

from electrons scattered at the entrance flange, which are cut away by the y_{flange}-cut.

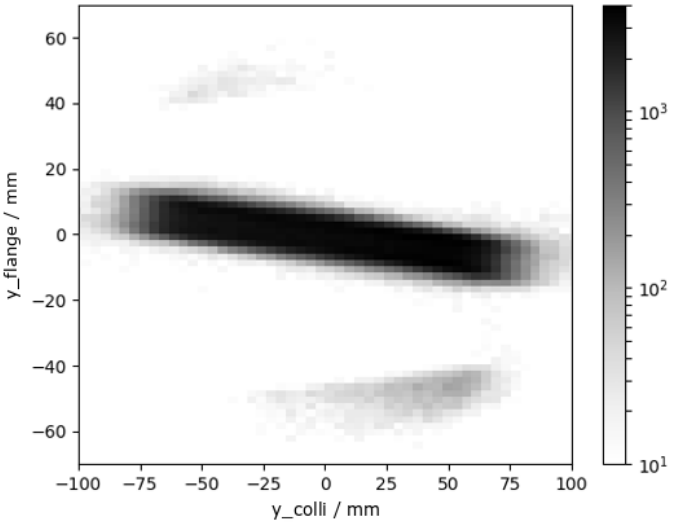

Figure 4.4: Two dimensional histogram of y_{flange} and the horizontal offset at the collimator y_{colli} for a measurement taken with spectrometer B at $32°$ and 180 MeV beam energy. The grey scale is logarithmic to emphasize the side bands. Around $y_{\text{flange}} = 0$ the good events are located. The events in the side bands are from electrons scattered at the entrance flange.

4.4 Target background

The liquid deuterium is contained within a cryogenic cell, cf. section 3.2.3. When the electron beam reaches the target, it has to propagate through its walls, which are thin foils made out of HAVAR. Besides the scattering of electrons at deuterons, scattering also occurs on the nuclei of the wall atoms. This scattering produces background signals also in the energy region of the elastic peak of the deuteron. The elastic peak due to scattering at the deuteron is located on the tail of the elastic peaks from the wall nuclei, due to the difference in recoil. At higher momentum transfer, the wall background signal mostly comes from quasi-elastic scattering.

Due to the different masses m_i of the nuclei of HAVAR, the elastic background peak is a superposition of several peaks at positions:

$$E_i' = \frac{E}{1 + \frac{E}{m_i(1-\cos\theta_e)}} \tag{4.10}$$

The peaks from the wall nuclei are broadened in the $\Delta E'$-spectra, since the reconstruction assumes $m_{\text{target}} = m_D$.
The background events which are located under the elastic deuteron peak have to be separated or subtracted from the data. A separation with kinematic cuts would only be possible in a coincidence experiment and not in a single arm experiment. The only possible cut in a single arm experiment to reduce the background would be a vertex position cut although it is difficult: The vertex resolution and accuracy depends strongly on the spectrometer angle and therefore cannot be precisely implemented. An estimation of the target length at cryogenic temperatures could not be attained with sufficient precision.
The contribution from the HAVAR background plays a significant role mostly for the spectrometer angles below 23°, because the smaller the angles the closer the wall peak is to the deuteron peak and therefore more background events appear in the deuteron peak region.

One possibility to subtract the contribution of the HAVAR wall would be to use

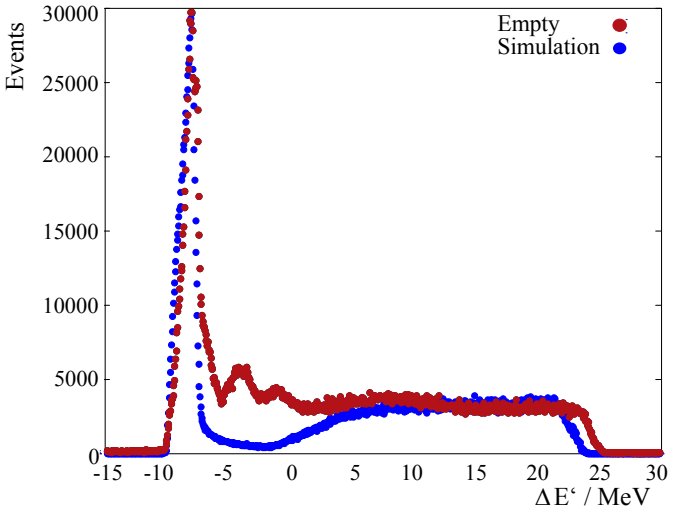

Figure 4.5: Comparison of empty cell data (red) with simulation for HAVAR wall (blue). The inelastic wall nuclei peaks are clearly visible between the elastic peak on the left and the quasi-elastic contribution on the right. The elastic peaks of data and simulation do not match perfectly mostly because of the thicker walls of the empty target.

a simulation of this contribution and subtract it from the data. Unfortunately the available simulation for HAVAR did include only the elastic and quasi-elastic part of the total contribution and no inelastic part. Comparing the simulation to the empty cell data, which was also taken during the beam time, showed that at least for certain kinematics the inelastic contribution is clearly visible in the data as additional peaks in the spectra, which are located between the elastic HAVAR peak

and the quasi-elastic contribution of the wall nuclei (see fig. 4.5).
Because of this insufficient description of the data by the available simulation the background subtraction of the the HAVAR wall is done by using the dedicated empty cell runs. In these runs the beam hit an empty target, which has the same dimensions as the cryogenic cell but thicker walls (5 times the thickness of the cryogenic cell). The thicker walls were chosen to reach the same radiation length for electrons passing through the empty cell as for electrons passing through the deuterium filled cell. Since the only material of the empty cell is the HAVAR of the walls, the only option to reach the same radiation length as for the filled cell was to increase the wall thickness. Unfortunately it is not possible to directly subtract the empty run data from the deuteron run data, since the different wall widths lead to different widths of the peaks produced by nuclei in the wall. The high number of background events for the smaller angles are the reason why the following description of background subtraction has the highest importance for spectrometer B, since only this spectrometer can reach angles below 23°. How small the effect for the bigger angles is can be seen exemplary in fig. 4.6. In this figure a typical spectrum of $\Delta E'$ is shown (here for 180 MeV, 27° in B), blue is the data curve, green the simulation which was scaled accordingly to the luminosity in the data, red is the data from the dedicated empty run and black the sum of simulation and empty data. The empty

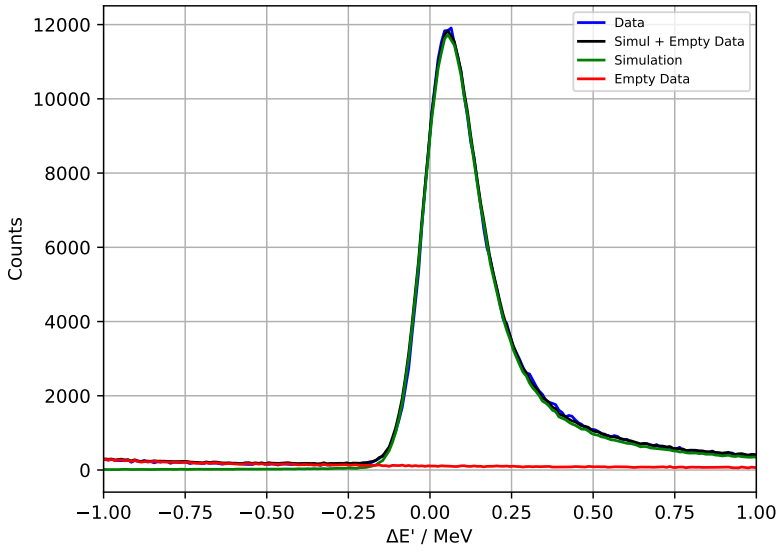

Figure 4.6: $\Delta E'$ spectrum for 27° at 180 MeV in spectrometer B, blue is the data curve, green the simulation which was scaled accordingly to the luminosity, red is the data from the dedicated empty cell run and black the sum of simulation and empty data.

cell data contributes here with less than 1% to the deuteron peak.
In fig. 4.7 an example for small angles is shown. The energy was again 180 MeV, but here spectrometer B was set to the angle 20°. The peak from the wall nuclei is quite close to the elastic deuteron peak and a lot of the events in its tail are in the region of this elastic peak. For angles smaller than 20° the empty cell peak is even closer to the deuteron peak and the subtraction of the background events gets more complicated, since there is not only the contribution to the background of the

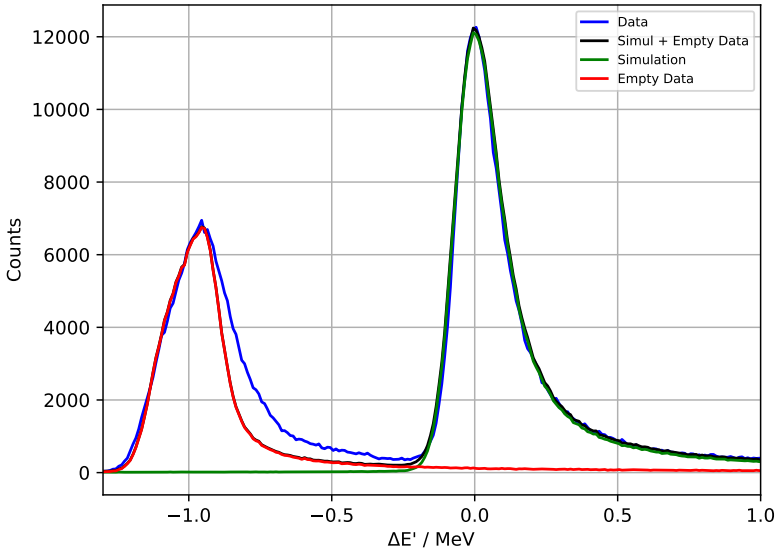

Figure 4.7: $\Delta E'$ spectrum for 20° at 180 MeV in spectrometer B, blue is the data curve, green the simulation which was scaled accordingly to the luminosity, red is the data from the dedicated empty cell run and black the sum of simulation and empty data.

scattering at wall nuclei but also at cryogenic depositions on the outer side of the HAVAR wall (see below). In this plot (fig. 4.7) it is also clearly visible that the wall peak from the empty target measurement has not the same width as the wall peak from the deuteron measurement, as mentioned before. So before the empty cell data could be subtracted from the deuterium data, the peak had to be broadened by a convolution of the empty cell data peak with a Landau function. The result of this convolution can be seen in fig. 4.8. The blue and the green curve are the data and the simulation as before and in red is now shown the empty cell data convolved with a Landau function. Now the width of the empty cell and the deuteron data in the wall peak match better than before, but it is already visible that there is another contribution on the right part of the wall part, which is not described so far.
The events from the HAVAR wall are the most significant, but not the only background contribution, which needs to be described and subtracted from the deuteron data. Since there are still some particles present in the vacuum chamber around the target cell and the cryogenic cell is at very low temperature, the left-over air particles are forming a thin layer of cryogenic depositions around the target cell. There the electrons can be scattered and contribute to an additional peak in the spectra. In fig. 4.9 the data minus the convolution for the empty cell background is shown in blue. The green curve is the deuteron simulation. On the left side of the deuteron peak is a remaining smaller peak which originates most likely from the electrons that are scattered from the frozen air particles around the target cell. In this plot a red curve is also shown which is the simulation for the ice, which is described in detail in section 4.2. This simulation aims to subtract the cryogenic deposition background in the data.
After the subtraction of empty cell events as well as of ice events the spectrum can be described fully. The black curve in this plot is the result after the subtraction of

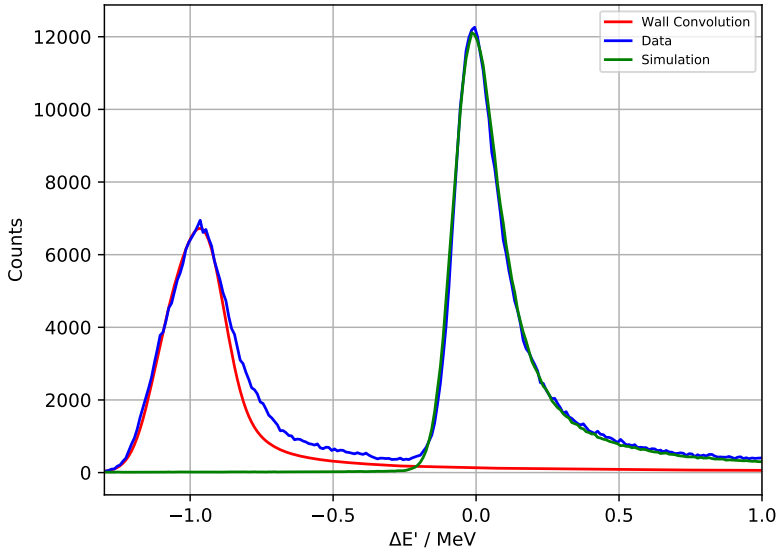

Figure 4.8: $\Delta E'$ spectrum for 20° at 180 MeV in spectrometer B, blue is the data curve, green the simulation which was scaled accordingly to the luminosity and red is the data from the dedicated empty cell run convolved with a Landau function.

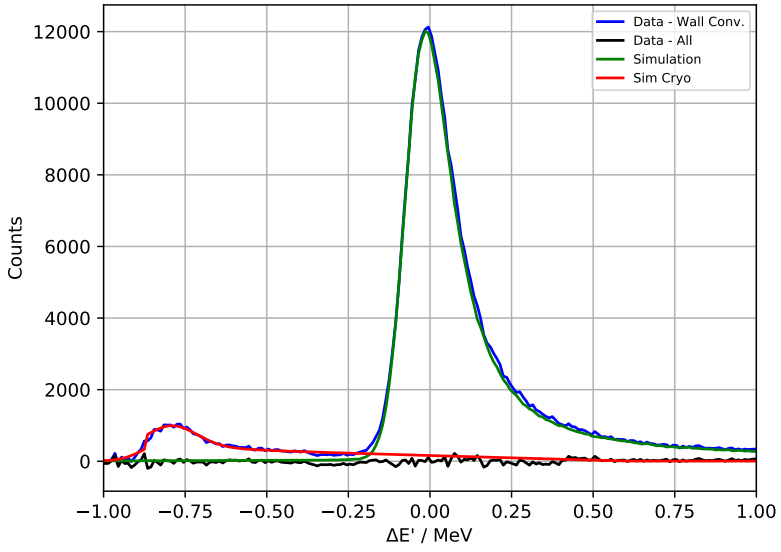

Figure 4.9: $\Delta E'$ spectrum for 20° at 180 MeV in spectrometer B, blue is the data minus the convulsion for the empty background, green the simulation which was scaled accordingly to the luminosity, the red curve is the simulation for the ice. In black the result of the subtraction of the simulation, the convolved empty cell data and the simulation for the cryogenic depositions from the deuteron data is shown.

the simulation, the convolved empty cell data and the simulation for the cryogenic depositions from the deuteron data. Since this is nearly zero, it shows that the data can be well described by these contributions.
As mentioned the background subtraction for smaller angles gets more complicated, because the wall peak and also the peak for the cryogenic depositions moves closer to the deuteron peak. The cryogenic deposition peak lies for very small angles nearly under the deuteron peak, so that it is not possible to see if the cryogenic simulation describes it adequately. Since, for these reasons, the description of the data for smaller angles is insufficient precise, the data taken at angles smaller than 20° are not used for the further analysis.

4.5 Luminosity

The integrated luminosity L_{int} is defined as the number of electrons N reaching the target in the duration of the measurement T multiplied by the areal density of the target nuclei n_T:

$$L_{\text{int}} = N \cdot n_T \tag{4.11}$$

The number of electrons is calculated from the integral over the beam current I in A,

$$N = \frac{1}{e} \int_T I dt \tag{4.12}$$

with the electron charge e. For this experiment the beam current is measured by a picoamperemeter (see. 3.2.4). The areal density of the deuterons n_T is given by the number of atoms within one of these molecules $z = 2$ and the their areal density n_{D_2} which can be determined by Avogadro's constant $N_A = 6.022 \cdot 10^{23} \frac{1}{\text{mol}}$, the mass-volume-density ϱ in $\frac{g}{cm^3}$, the thickness l in cm and the molar mass M_{D_2} in $\frac{g}{mol}$:

$$n_T = z \cdot n_{D_2} = 2 \cdot \frac{N_A}{M_{D_2}} \cdot \varrho \cdot l \tag{4.13}$$

The target density ϱ is calculated from continuous pressure and temperature measurements. These parameters were found to be almost constant during the measurements, an example will be given in 3.4. The luminosity has to be corrected for prescaling and dead time.
In addition to the luminosity measurements with spectrometer C, spectrometer A and B were instrumentalized interchangeably as luminosity monitors, this was possible, since these two spectrometers were never moved to a new angle at the same time, while spectrometer C stayed at the same angle. To make this possible and to keep the 50° spacing between spectrometer B and C as mentioned in 3.3, spectrometer C had to be at a significantly higher angle than the other two spectrometers. Due to this reason spectrometer C was not employed to measure the luminosity for all data

runs. The luminosity measured with the spectrometers was used for cross checking the readings from the picoamperemeter and the fluxgate magnetometer. For this each measurement of the luminosity monitor is analyzed in the same way as for the cross section measurements, e.g. the same procedure of background subtraction (see 4.4) is performed. The luminosity can be written as:

$$L = \frac{I \varrho l N_A}{e M_{D_2}} \tag{4.14}$$

The only value in this equation which is not (nearly) constant for all runs is the beam current which was increased for higher angle settings. Since the luminosity is calculated relative to the one for the previous run:

$$L_i = L_{i-1} \frac{E_i \cdot PS_i \cdot t_{i-1}}{E_{i-1} \cdot PS_{i-1} \cdot t_i} \tag{4.15}$$

many common factors like the angular acceptance cancel out and uncertainties in their determination play no role at this point. As seen in eq. 4.15 the other values needed to determine the relative luminosity are the number of events E_i, the prescaler PS_i and the time t_i of each run. The prescaler is a factor which scales the number of recorded events during data taking. The experiment allows prescaling of the triggers, so that only every n-th event is recorded. Only recorded events produce significant dead-time. The prescaling helps up to a certain amount to accommodate the largely different event rates in the different spectrometers at different scattering angles. The time of the run t_i is the dead-time corrected duration of the run. Equation 4.15 is valid in this form if one spectrometer would have been used as luminosity monitor for all runs. For interchangeable luminosity monitors a distinction of cases has to be done, which is shown in detail in appendix B.
In fig. 4.10 the comparison of the charge values calculated from the picoamperemeter and from the luminosity measurement can be seen. To increase the visibility in the plot the ratio of the two current values is plotted against the picoamperemeter value. One disadvantage of the method to get the current from the luminosity measurements is that the error increases from run to run (see appendix B). But in the error margin the two methods agree with each other.
In fig. 4.11 the charge values calculated from the picoamperemeter and from the fluxgate magnetometer are being compared. Also here the ratio of the two values is shown. As expected, since the fluxgate magnetometer is not very sensitive for low currents (see 3.2.4), the two methods do not agree for low currents. With increasing current the values from the picoamperemeter tend to agree better with those from the fluxgate magnetometer.

4.6 Fit of the form factor model to the cross section

To do a fit of the measured cross sections, an ansatz has to be made for the description of the form factors. For this thesis a parametrization which employs a

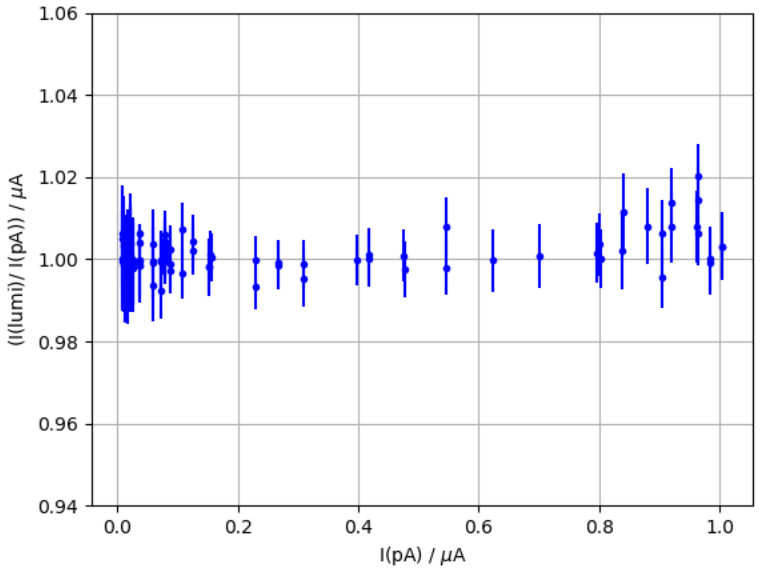

Figure 4.10: Comparison of the current of the electron beam calculated using the pA readouts and calculated using the luminosity taken with the spectrometers. On the y-axis the ratio of the two currents is plotted.

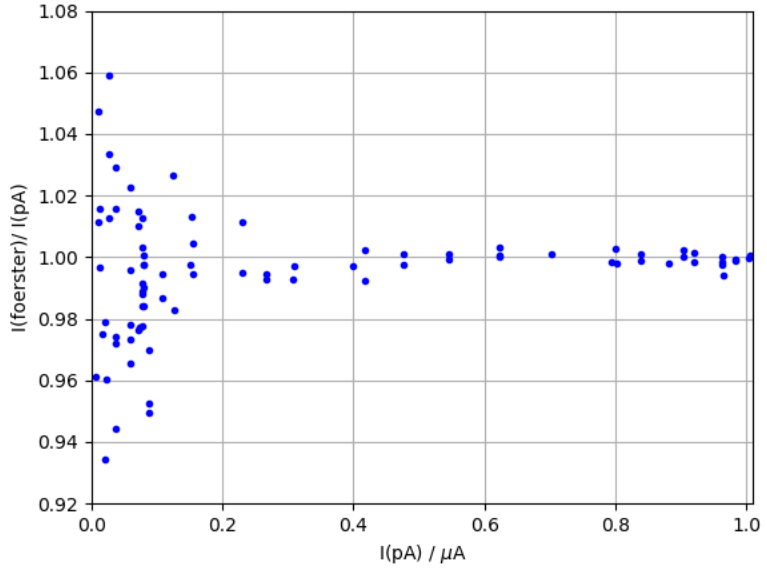

Figure 4.11: Comparison of the current of the electron beam calculated using the pA readouts and calculated using the fluxgate magnetometer (Förster probe). On the y-axis the ratio of the two currents is plotted.

Sum-of-Gaussians was chosen [78, 79]. In this parametrization the form factors are written as:

$$G_X(Q) = G_X(0) \cdot e^{-\frac{1}{4}Q^2\gamma^2} \sum_{i=1}^{25} \frac{A_i}{1+2\frac{R_i^2}{\gamma^2}} \left(\cos(QR_i) + \frac{2R_i^2}{\gamma^2} \frac{\sin(QR_i)}{QR_i} \right) \tag{4.16}$$

The index X stands for the three form factors, charge monopole G_C, charge quadrupole G_Q and magnetic dipole G_M. Since this experiment is only sensitive to measuring the charge monopole form factor G_C, only the corresponding parameters were fitted. The parameters for G_Q and G_M were taken from a parametrization done by Abbott et al. [79]. The cross section calculated with all parameters from Abbott et al. is called from now on Abbott cross section.
The Sum-of-Gaussians parametrization corresponds in configuration space to a density $\varrho(R)$ written as a sum of Gaussians placed at arbitrary radii R_i, with amplitudes A_i and a fixed width γ, which are fitted to the data. The distances R_i relate to the distances of the nucleons to the center of mass of the deuteron.
This parametrization represents a totally general basis and the following restrictions were applied accordingly to those described in [79].
The width γ corresponds to the size of the proton ($\gamma\sqrt{3/2} = 0.8$ fm), since there are no expected structures smaller than the size of the nucleon. Accordingly the spacing between the Gaussians is chosen slightly smaller than this width (0.4 or 0.5 fm). The fact that the radius at which the tails of densities give no significant ($< 10^{-3}$) contribution to $G_X(Q)$ can be specified, justifies to place the Gaussians at radii $R_i \leq R_{\max} = 10$ fm. Additionally the deuteron wave functions have an analytic form outside of the range of the Nucleon-Nucleon-force, which depends only on the deuteron binding energy. Therefore this shape can be imposed and the ratio of the amplitudes A_i can be fixed, for radii $R_i \geq 4$ fm. These restrictions leave 11 free parameters for the fit of the form factor: 10 Gaussian amplitudes A_1 to A_{10} corresponding to $R_i < 4$ fm and one overall amplitude for the shape-given tail at $R \geq 4$ fm.

The cross sections which were determined by the experiment are analyzed by using a fit of the previously described model for the form factors. One of the most challenging tasks in a cross section measurement is the absolute normalization. It is near to impossible to determine this normalization down to a sub-percent level directly from the knowledge of all relevant properties of the experiment. Fortunately theory states that the form factor G_C has to go to one for Q^2 going to zero and it is possible to use this limit to determine the normalization from the measured data. Therefore the fit also has to include normalization constants for each group of data in addition to the parameters of the form factor model. For this purpose one group of data consists of the cross sections measured for one energy with one spectrometer for different angles. This results in six normalization constants in addition to the 11 model parameters described in 4.6.

The function which is minimized by the fit is analog to the one used for the electron scattering at proton measurements described in [71]:

$$\chi^2 = \sum_i \left(r_i - N_i \frac{\int_{A_i} \left(\frac{d\sigma}{d\Omega}\right)_{\text{fit}} d\Omega}{\int_{A_i} \left(\frac{d\sigma}{d\Omega}\right)_{\text{Abbott}} d\Omega} \right)^2 / \left(\Delta r_i\right)^2 \tag{4.17}$$

The ratio of the ith measured cross section to the Abbott cross section is r_i, the normalization constant of the corresponding data group is N_i, the acceptance of measurement i is A_i and the statistical error of r_i is Δr_i. $\left(\frac{d\sigma}{d\Omega}\right)_{\text{fit}}$ is the result for the cross section from the fit and $\left(\frac{d\sigma}{d\Omega}\right)_{\text{Abbott}}$ is the cross section calculated with the parameters from Abbott [79]. For this calculation the acceptance integration is done numerically.
A measure of how well the data points are compatible with the assumption that they can be described by the used fit function is the reduced χ^2:

$$\chi^2_{\text{red}} = \frac{\chi^2}{d} \tag{4.18}$$

d is the number of degrees of freedom which is the difference of the number of data points and the number of fit parameters.
For a perfect matching fit χ^2_{red} equals 1. If χ^2_{red} is much larger than 1, the assumption is not well chosen and for a χ^2_{red} lower than 1 the uncertainties are probably chosen too pessimistically. For the function used here to describe the data the reduced χ^2 is 1.1(calculated with 480 data points and 17 fit parameters), so the fit describes the data well.
Figure 4.12 shows the normalized cross section data divided by the cross section given by the calculations of Abbott et al. [79] compared to the fit as functions of Q. The data points from the measurements with spectrometer A are shown in red and the ones from the measurements with spectrometer B in blue. The errors in this plot are the statistical ones. For all three energies the data points do not deviate more than one percent from one.

4.7 Determination of the errors on the cross section

4.7.1 Statistical errors

In the chosen form factor model the cross section does not depend linearly on all the parameters. That is the reason for choosing a Monte Carlo method to determine the statistical error on the cross section fit.
For this method a large number (10000) of pseudo data sets are generated. Starting points for creating these data sets are the measured cross sections divided by the results from Abbott [79]. Each of these cross section data points is then randomized with a Gaussian distribution according to the statistical error of the data. Basically these pseudo data sets are the simulation of the result of 10000 experiments with

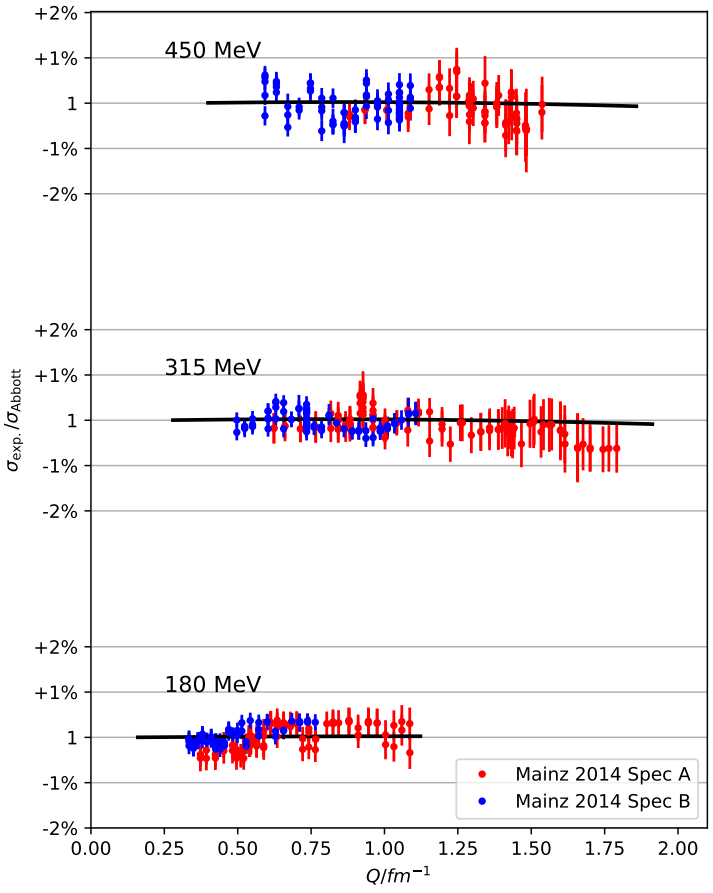

Figure 4.12: The measured cross sections and the fit, divided by the cross section given by the calculations of Abbott et al. [79] as function of Q. The error bars in this plot are the statistical ones. The data points from the measurements with spectrometer A are shown in red and the ones from the measurements with spectrometer B in blue.

the same number of cross section measurements each.
Each of these pseudo data sets is then fitted with the same model as the original data. At each Q^2 the confidence band is constructed around the fit to the original data. Inside the confidence band are 68% of the fit functions, the remaining fit functions are half above and half beneath the confidence band. The result for all three beam energies is shown in fig. 4.13.

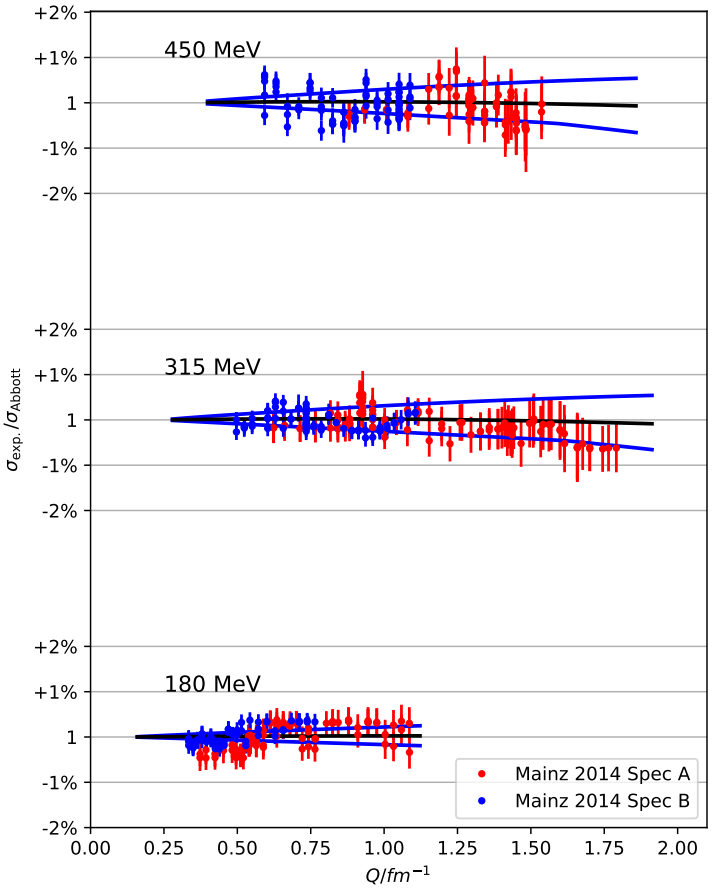

Figure 4.13: The measured cross sections divided by the Abbott cross sections for all three beam energies with the fit curve in black (simultaneous fit of all data sets) and the upper and lower edge of the statistical confidence band in blue. The error bars in this plot are the statistical errors. Upper part of the plot corresponds to a beam energy of 450 MeV, the middle part to 315 MeV and the lower part to 180 MeV.

4.7.2 Systematic errors

For the systematic errors it has to be noted that a global shift of the data has no effect on the result, because it is subsumed in the fitted normalization. However,

drifts over time transform into changes in the slope of the data versus Q^2 and the scattering angle, respectively, which will influence the outcome of the fits. That is why such trends in the data have to be estimated. For larger angles a small drift in the data can be noticed, therefore it is important to estimate the respective error. Sources for experimental systematic errors are:

- Energy cut in the elastic tail. By varying the cut-off energy in the analysis, this can be estimated. It changes the cross section results by 0.1 - 0.2%.
- Beam energy uncertainty. This was estimated by the accelerator team to be 160 keV for the beam energies 315 and 450 MeV. Since the beam with an energy of 180 MeV does not enter RTM3 a different beam energy determination has to be used, which is less accurate, the error is estimated to be 250 keV [80].
- Efficiency change due to different positions of the elastic peak on the focal plane. This has to be considered because the efficiency of the detector is position-dependent and the wires in the drift chambers can have different tensions. Also there can be missing wires and the quality of the scintillators can differ. Since the kinematics were always chosen as such, that the position of the elastic line in the focal plane changes only slightly during the experiment, this effect is estimated to be small. From the efficiency calibration data an uncertainty smaller than 0.07% is estimated.
- Normalization drift, due to unaccounted dead time effects in the detector/ electronics when the event rate changes. As far as possible the event rate was held constant by adjusting the beam current, the prescaling and the spectrometer angles. Since this was not always perfectly possible, it has to be considered as a source of uncertainty. The resulting error on cross section measurements can be estimated from long time experience with the detector setup to be smaller than 0.05%.
- Background estimation. Depending on the amount of background events below the elastic peak this error is estimated to be between 0 and 0.3% and it is, as expected, found to have a higher impact on the smaller angles than for the larger angles (see appendix D for some details), due to the fact that the wall peak is closer to the elastic peak for smaller angles. To get this estimation, the estimated number of background events was varied and the result for the cross section was checked.

The last two errors need to be applied manually to the data. Before being able to do so, the cross section values have to be grouped by the spectrometer and the energy they were measured at. For each of the 6 groups a factor, which was interpolated between the minimum and maximum estimated uncertainty (which relates to the minimum and maximum Q value), is multiplied onto the cross section values ($\frac{d\sigma}{d\Omega} \cdot (1 + \text{factor})$). These modified cross sections are then fitted with the same form factor model as the unmodified cross sections. By repeating this procedure with a negative slope in the interpolation an upper and a lower bound can be determined. This procedure was done for each of the sources of systematic errors. In the end

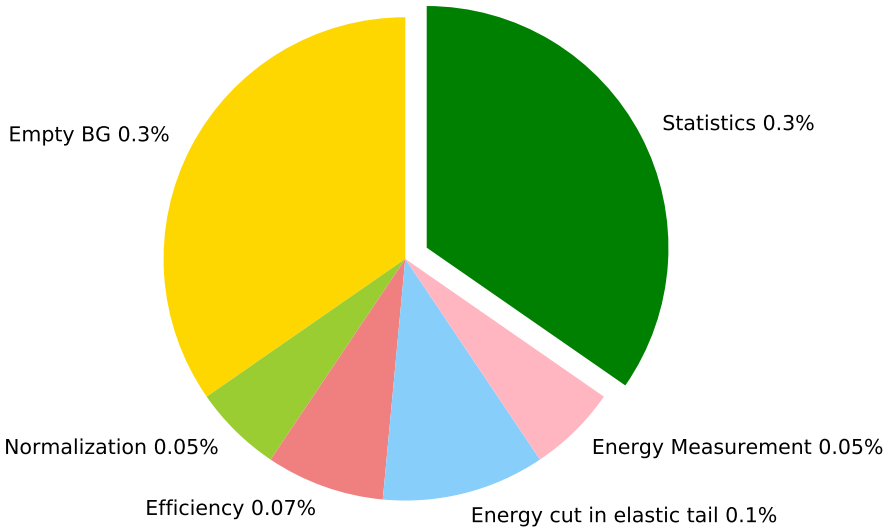

Figure 4.14: Uncertainties on the measurement of the cross section. About one third of the errors is caused by the statistics of the experiment. The largest contribution to the systematic errors is the background coming from electrons which were scattered at the wall of the target cell. For details on the different kind of error sources see 4.7.

all experimental uncertainties were combined quadratically. All experimental contributions to the error are shown in fig. 4.14. It is clearly visible that the largest experimental contributions to the total error are the background estimation and the statistics.
Another category of systematic errors are the theoretical errors. The radiative corrections are described in 2.2.2 and should be known well enough that any slope in the data which is introduced by this correction should be contained in the slope uncertainty, which was described above.
However, another part of the theoretical systematic errors is related to the Coulomb correction. For this correction an approximation was used (see 2.2.2 eq. 2.25). To estimate the effect on the fit the correction was scaled by $\pm 50\%$. With the modified cross section the same procedure as for the experimental systematic errors was performed.
In all cross section plots from here on the error bands for the systematic experimental and theoretical uncertainties are added linearly to the statistical error bands.

5

Results for the Form Factor and Interpretation

5.1 Fit of the form factor

The fit parameters of the form factor model are fixed with the fit of the measured cross section divided by the cross section given by the calculations of Abbott et al. [79]. The fit parameters together with eq. 4.16 give the plot shown in fig. 5.1. The

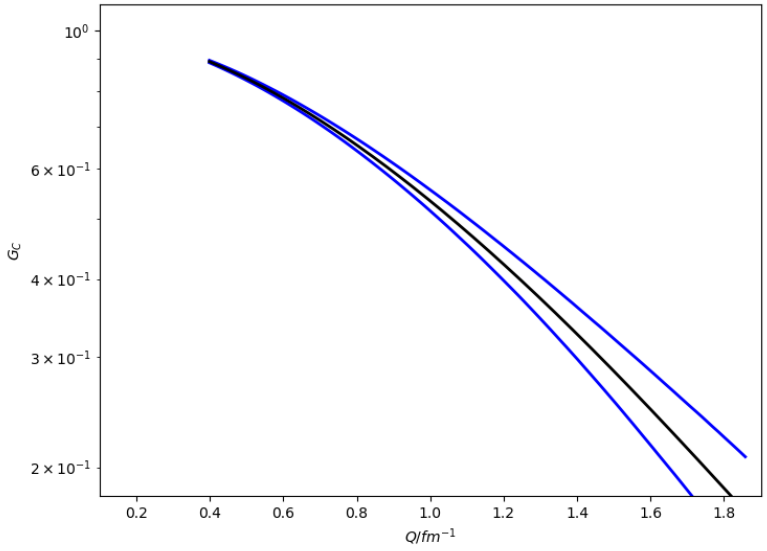

Figure 5.1: The charge form factor of the deuteron, when inserting the fit parameters in the form factor parametrization eq. 4.16. The fit to the charge form factor is shown as the black solid line and the corresponding error band boundaries in blue.

fit to the charge form factor is shown as the black solid line and the corresponding error band boundaries in blue. From the slope of G_C at $Q = 0$ the deuteron charge radius can be extracted, see 5.2.
As a cross check to see if the calculations and fitting procedures are consistent an alternative approach to calculate the charge form factor is described in the following. The measured data points for the cross section can also be used to calculate the

charge form factor for each Q value individually. From equations 2.11, 2.14, 2.15 and 2.16 the charged form factor is written as:

$$G_C^2(Q^2) = \frac{\left(\frac{d\sigma}{d\Omega}\right)}{\left(\frac{d\sigma}{d\Omega}\right)_{\text{Mott}}} - B(Q^2)\tan^2\left(\frac{\theta}{2}\right) - \frac{8}{9}\eta^2 G_Q^2(Q^2) - \frac{2}{3}\eta G_M^2(Q^2) \tag{5.1}$$

The values for the cross section, the scattering angle and Q are known from the

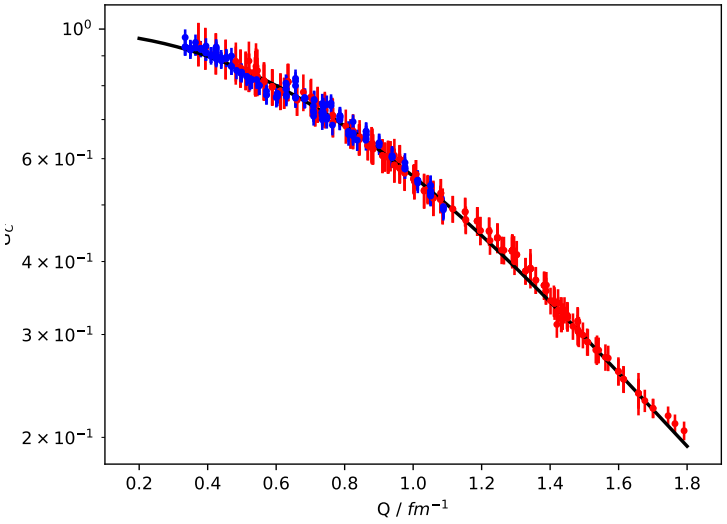

Figure 5.2: The charged form factor of the deuteron from the cross section data, the error bars in this plot originate from the statistical errors. The data from spectrometer A is shown in red, while the data from spectrometer B is shown in blue. The fit function to the charged form factor is represented in black.

experiment, $G_Q^2(Q^2)$ and $G_M^2(Q^2)$ can be calculated by using the results from Abbott et al. [79]. The only remaining unknown part of this equation is $\left(\frac{d\sigma}{d\Omega}\right)_{\text{Mott}}$ which can be determined by using a simulation of the Mott cross section for all kinematics that were measured in the experiment. This simulation is basically the same as for the deuteron scattering, but without the deuteron form factor part.
The result for the charge form factor can be seen in fig. 5.2. The error bars represent only the statistical errors, which are calculated by error propagation from the errors of the cross section. A similar fit procedure as for the cross section was used to fit the charge form factor. The result of the fit can also be seen in fig. 5.2 as the solid black line.
Fitting the points which were calculated from the measured cross section data is a cross check to see if the calculations and fitting procedures are consistent. In 5.2 the charged deuteron radius will be determined by employing the fit of the cross section data and by applying the fit to the here shown charge form factor.

5.2 Determination of the radius

The deuteron charge radius can be extracted from the slope of $G_C(Q^2)$ at $Q^2 = 0$. It is not possible to measure at $Q^2 = 0$, but from the fitted form factor model parameters, the radius can be directly calculated

$$r_d = \sqrt{-6 \cdot \left(\frac{dG_C}{dQ^2}\right)_{Q^2=0}} \tag{5.2}$$

by using the parametrization eq. 4.16.
The fit parameters together with eq. 4.16 give the plot shown in fig. 5.1. The result for the deuteron charge radius is

$$r_d = (2.121 \pm 0.007_{\text{stat.}} \pm 0.014_{\text{syst.}})\,\text{fm} \tag{5.3}$$

The value for the systematic error for the deuteron charge radius was determined by a similar procedure as for the cross section, which is described in 4.7.
As mentioned in 5.1 the fit to the charge form factor points can also be used as a cross check for the radius. Using the fit from 5.1 the same result for the radius with slightly larger errors is found. Therefore the two methods are consistent to each other. The larger errors can be explained by the error propagation and the usage of the Mott Simulation.

5.3 Comparison with existing data

The cross section data and the charged deuteron radius determined in this experiment is in the following compared with existing data. As mentioned in **??** there are three sets of existing data to which the cross section results of this analysis can be compared. The data from Berard *et al.* [46] were taken using cooled H_2 and D_2 gas targets, in the range of four momentum transfer $Q = 0.2 - 0.7$ fm^{-1}. The experiment measured ratios of cross sections relative to hydrogen. To get the cross sections for the deuteron a normalization to absolute data on the proton was performed. The experiment performed by Simon *et al.* [47] used both a low temperature gas and a liquid target for both hydrogen and deuterium. The hydrogen data taken with the gas target and a special small angle spectrometer served as the absolute cross section standard and the data with the liquid targets were measured relative to this standard. With this procedure the Q range $Q = 0.2 - 2$ fm^{-1} was covered. The data from Platchkov *et al.* [48] were measured with a liquid deuterium target and the experiment provided absolute data in the range $Q = 0.7 - 4.5$ fm^{-1}.
These data sets from Berard *et al.* (black points, 1973), Simon *et al.* (lightgreen points, 1981) and Platchkov *et al.* (turquoise points, 1990) can be seen in fig. 5.3 in the upper part. The measured cross sections divided by the Abbott cross sections for all three beam energies measured in this experiment are shown in the lower part of the plot labeled with 180, 315, 450 MeV, for all data points in this plot the sta-

tistical error is shown.

It is clearly visible that the Mainz2014 data points deviate never more than 1%

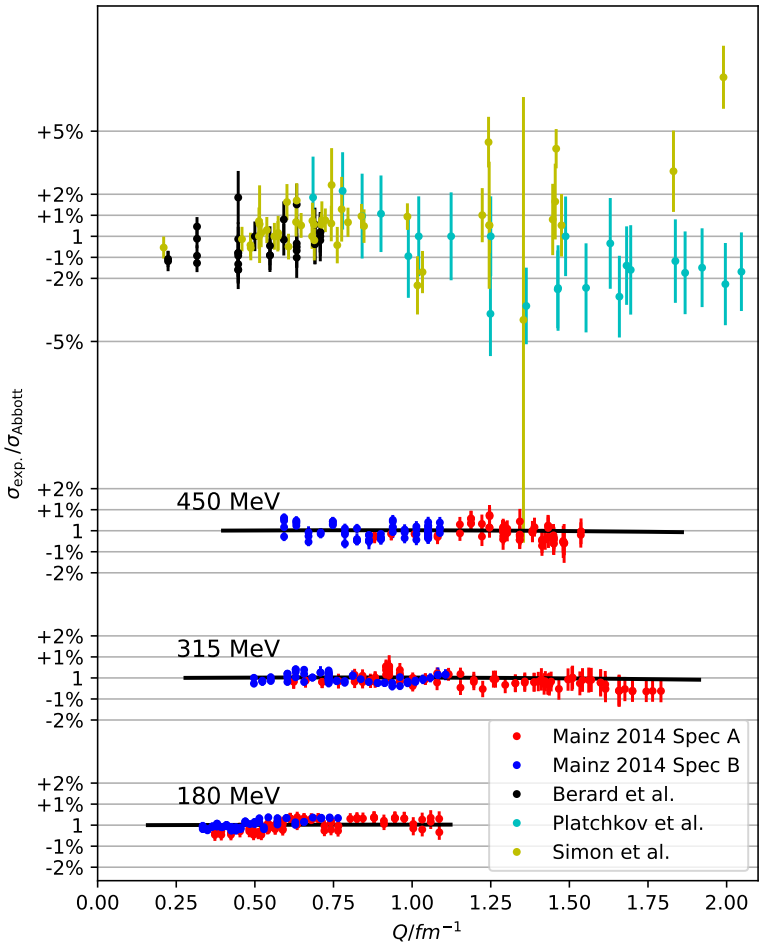

Figure 5.3: The measured cross sections divided by the Abbott cross sections for all three beam energies measured in this experiment (lower part of the plot labeled with 180, 315, 450 MeV) in comparison to existing data from Berard *et al.* (black points, 1973) [46], Simon *et al.* (lightgreen points, 1981) [47] and Platchkov *et al.* (turquoise points, 1990) [48].

from $\frac{\sigma_{exp}}{\sigma_{Abbott}} = 1$, where the existing data sets show a deviation up to 5% and higher. The data set from Simon *et al.* shows a trend to higher values for $\frac{\sigma_{exp}}{\sigma_{Abbott}}$ for higher values of Q. This is not visible in the Mainz2014 data set. Contrary to this the Platchkov *et al.* data sets shows a tendency to lower values for higher Q. This can also be observed in the Mainz2014 data set, especially for the data taken at 315 MeV. The Berard *et al.* data set does not contain data points at higher Q values, so it is not possible to state if this data set shows a trend to higher or lower values.

The charge radius determined from the Mainz2014 experiment can be compared

to the result from existing electron scattering data, but also to results from other kinds of experiments, which are also able to determine the deuteron charged radius. An overview of results from different kind of experiments can be seen in fig. 5.4 and in tab. 5.1.

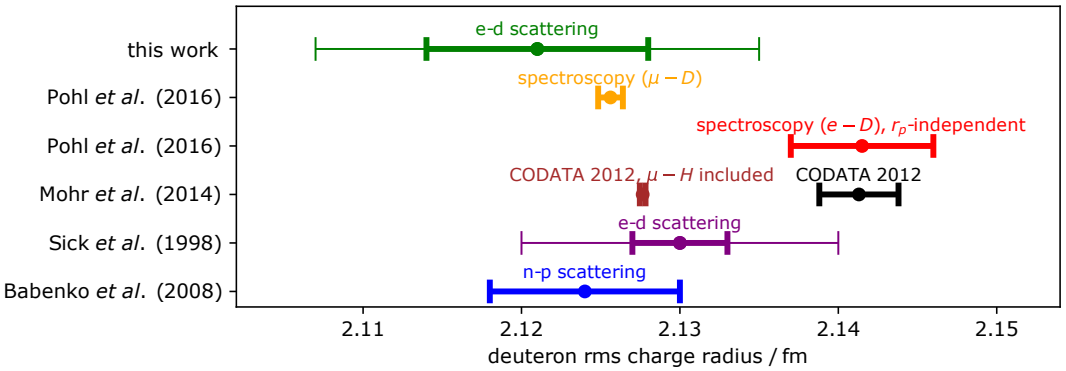

Figure 5.4: Overview of results for the deuteron charge radius from different kind of experiments. The different experiments are (from bottom to top): n-p scattering by Babenko *et al.* [81], e-d scattering by Sick *et al.* [82], CODATA2012 and CODATA2012 μ-H included by Mohr *et al.* [24], spectroscopy μ-D and e-D by Pohl *et al.* [83] and the result from this thesis. For the results from e-d scattering the statistic (bold bars) and systematic (thin bars) error bars are shown separately, for all other results only a total error was available.

name	experiment	r_d / fm	Δr_d / fm
this work	e-d scattering	2.121	$0.007_{stat.} \pm 0.014_{syst}$
Pohl	spectroscopy (μ - D)	2.12562	0.00078
Pohl	spectroscopy (e - D)	2.1415	0.0045
Mohr	CODATA12 μ-H included	2.12765	0.00018
Mohr	CODATA12	2.1413	0.0025
Sick	e-d scattering	2.130	$0.003_{stat.} \pm 0.01_{syst}$
Babenko	n-p scattering	2.124	0.006

Table 5.1: Numerical results for the deuteron charge radius from different kind of experiments. The different experiments are: n-p scattering data analyzed by Babenko *et al.* [81], e-d scattering data analyzed by Sick *et al.* [82], CODATA2012 and CODATA2012 μ-H included by Mohr *et al.* [24], spectroscopy μ-D and e-D by Pohl *et al.* [83] and the result from this thesis.

The result from n-p scattering by Babenko *et al.* was obtained with the aid of modern experimental results for phase shifts from the SAID [84] nucleon - nucleon data base. Investigations of the correlation between the root-mean-square matter radius and its effective radius lead to a value for the charge radius. For more details see [81]. Sick *et al.* [82] used the available world data on e-d elastic scattering to determine the deuteron structure functions and the charge rms radius. The world data includes (besides many more) the data from Berard *et al.*, Simon *et al.* and Platchkov *et al.*. The CODATA values by Mohr *et al.* [24] are based on a least-square adjustment that takes into account all data available up to the end of 2014. Values of r_p and

r_d from electron - proton and electron - deuteron scattering data were used as input data in an adjustment together with H and D spectroscopic data and theory to obtain a combined least-square adjusted value for r_p and r_d. The input value for r_d is the value obtained by Sick *et al.*. The calculations for the two CODATA values in fig. 5.4 and tab. 5.1 differ only in the fact that the value 'CODATA 2012' is the CODATA base value and the 'CODATA12 μ-H included' also includes the value for r_p from muonic hydrogen measurements. The two values by Pohl *et al.* [83] were obtained in spectroscopy measurements with muonic deuterium and muonic hydrogen and were acquired in the same measurement period. In these experiments three 2S-2P transitions were measured. The principle of the experiment is to form μd atoms in the meta stable 2S state and to measure the 2S-2P transition by pulsed laser spectroscopy. Comparison with theory reveals r_d.
Figure 5.4 shows that four of the six shown results agree within the error bar with the result which was obtained in this thesis. Only the (e-D) spectroscopy and the CODATA2012 value differ too much from the here obtained value to lie within the error bar. The e-d scattering result is also within the error margin of the values of n-p scattering and the e-d scattering calculated by Sick *et al.*. Since the muonic spectroscopy experiments result in a very small error, these errors are not comparable to the much bigger errors from scattering experiments.
The size of the error bars can be compared best for the two e-d scattering results. The statistical error of the result by Sick *et al.* is smaller than the one obtained in this thesis, which is probably due to the high number of data points and measurements which contribute to the Sick *et al.* radius result. The statistical error on the radius from this thesis is with less than half a percent as small as could be expected by the design of the experiment. With more measuring time this error would get even smaller. The systematic error is less than one percent for the result in this work, which is more than double as much as the one from Sick *et al.* , comparing it to the result from Sick *et al.* is not completely reasonable since it is not known in detail what kind of systematic error sources contributed to the error. However, it can be concluded that the here obtained value of the deuteron radius agrees with most of the other values shown in fig. 5.4 and tab. 5.1, but it shows a tendency to a smaller value for the radius than the other shown results.

6

Conclusions and Outlook

6.1 Conclusion

A high precision experiment of the elastic electron - deuteron scattering cross section was performed at the A1 3-spectrometer-facility at the MAMI accelerator in the Q range from 0.27 to 1.76 fm^{-1}. In three weeks of beam time 180 different settings were measured for the deuterium target as well as for the corresponding empty cell target. Important tasks in the analysis are the simulation of the electron-deuteron scattering as well as the simulation of the cryogenic depositions around the target cell. The first step for handling the data is the preparation of the raw data by using cuts on the accepted momenta, the out-of-plane angle and the in-plane angle to reduce the background. The handling of the background coming from electrons which were scattered at the walls of the target cell is a critical task in the analysis of the data. Since the tail of the distribution of these electrons is located - especially for small scattering angles - beneath the elastic deuteron peak it has to be removed as effectively as possible from the rest of the data. Available simulations of this contribution to the background did not include the inelastic part. Due to that circumstance the data from the empty cell measurements had to be used instead of the simulation to subtract the wall contribution of the background.
With the measured data points for the cross section the charge form factor was determined with two methods. The first way was to fit the measured cross sections divided by the cross section given by the calculations of Abbott et al. [79] with a Sum-of-Gaussians parametrization. While in the second approach, being a cross check, the measured data points for the cross section were utilized to calculate the charge form factor for each Q value. A similar fit procedure as before was employed to fit the charge form factor. It was found that the two methods are consistent.
The aim of this work was to deduce the deuteron charge radius with high precision to gain more insight into the puzzle of the different radii results from different experimental procedures. The obtained value for the deuteron radius in this thesis

$$r_d = (2.121 \pm 0.007_{\text{stat.}} \pm 0.014_{\text{syst.}})\,\text{fm} \tag{6.1}$$

is in agreement with most of the other values shown in fig. 5.4, but at the same time shows a tendency to a smaller value in comparison to the other shown results. Due to the systematic uncertainties a more precise conclusion cannot be drawn at this point. The sources for these are the energy cut in the elastic tail, the beam energy

uncertainty, the efficiency change due to different positions of the elastic peak on the focal plane and the normalization drift, due to unaccounted dead time effects in the detector / electronics when the event rate changes. The largest contribution to these systematic uncertainties is that of the background subtraction.
It has to be noted that the Coulomb correction applied to the present work is only an approximation and the radius might change when a more detailed calculation is applied. The inclusion of sophisticated Coulomb correction and eventually even hard two photon exchange correction is not within the scope of this work, but will be performed before final publication of the results. A possible strategy to decrease the systematic errors even further in such type of experiments will be discussed in the following section.

6.2 Outlook

The value for the deuteron radius in this thesis with a statistical error as small as could be expected from the design of the experiment and a systematic error twice as large as the statistical one represents a promising result. However it is still not precise enough to solve the proton radius puzzle. Possible future steps could be even more precise electron-deuteron measurements, other kinds of experiments and improvements in the theory. These possibilities will be discussed in this section.
For more precise electron-deuteron measurements the uncertainties have to be decreased. All experimental contributions to the error are shown in fig. 4.14. The statistical error can be decreased in a simple yet time consuming way by increasing the measuring time and therefore the sample quantity for each setting. The systematic errors are more challenging to decrease. A decrease of the error contribution would make the largest impact, due to the background caused by the walls of the empty cell. The most self-evident approach here is to measure without any walls at all. Such an approach is currently not within reach with the target setup used for the present work, since only liquid deuterium in a target cell could be used. However, at the moment a new accelerator with new targets and detectors is under construction in Mainz. The new accelerator will be the **M**ainz **E**nergy-recovering **S**uperconducting **A**ccelerator (MESA) [85], which will be the first superconducting energy-recovering accelerator dedicated to research. With the high intensity and quality of its beam, MESA will provide a unique platform for a forward-looking experimental program to study and test the limits of currently known phenomena in elementary particle physics [86]. A future experiment at MESA will be MAGIX [85], which will be a versatile fixed target experiment which is designed to perform precision measurements of nuclear observables in the range from a few MeV to about 100 MeV. In comparison to the current setup of MAMI far lower energies are accessible. This also opens another point of action to improve the radius determination, since with smaller electron energies it is possible to reach the range of lower Q^2, which is necessary to improve the extrapolation to $Q^2 = 0$. MAGIX will be equipped with two magnetic spectrometers with high precision gas detectors and a jet target [87]. The idea of this target is to blast a high velocity gas (i.e. deuterium) through the

vacuum in the scattering chamber perpendicular to the beam line, into a catcher, where the gas is removed quickly by pumping from the interaction volume. In this procedure the gas will be accelerated up to three times the sonic velocity. The big advantage of this setup is that the absence of target walls and therefore their contribution to the detected signal.
Another promising starting point to improve the radius result is to employ a more precise calculation for the Coulomb correction. As already mentioned several times an approximation was used for this correction in the present work. Sick *et al.* [82] found that the numerical value of the Coulomb correction is sensitive to the deuteron charge distribution. In the range of low values of q the main effect of the Coulomb distortion is the change in cross section given for a point like nucleus. In the cited paper the authors come to the conclusion that at low values of q, these correction reach 0.8% and that this correction affects the radius. They describe their analysis of the world electron-deuteron scattering data as following. First they convert the experimental cross sections from the different scattering experiments to effective plane-wave impulse approximation (PWIA) cross sections by removing the Coulomb distortion effects. Next they determine $A(q)$ and $B(q)$ and fit the cross sections with a parametrization of $A(q)$ and $B(q)$. The flexible form factor parametrization which was used is a Sum-of-Gaussian parametrization, similar to the one used in this thesis. From these form factors they calculate the cross sections in the PWIA and fit the parameters to the data (already corrected for the Coulomb distortion). To calculate the Coulomb distortion the authors use a second order Born approximation, which needs solving a challenging integral. As shown in [88] this approach gives no significant difference to the exact partial-wave cross section.
The deuteron radius can also be measured by employing laser spectroscopy of electronic or muonic hydrogen, and therefore links the fields of nuclear and atomic physics. New insight to the radius puzzle could also come from new experiments and findings in this field. The spectroscopy of deuterium requires the knowledge of the Rydberg-constant R_∞. To deduce R_∞ and r_d two measurements are usually performed. The first utilizes the transition 1S-2S, due to its precise nature and due to the largest sensitivity towards r_p [27]. The second utilizes the transitions from 2S to higher states [28]. The large discrepancy between the result from muonic and electronic deuterium spectroscopy originates from the strong deviation for two of the transitions in the second measurement. The others show a difference below 2σ [29, 30]. New measurements for R_∞ could help discover an error in these two transition measurements and could lead to less variation in total.
It is also possible that there is an error in the muonic theory. The largest contributions to the theory are the one-loop electron vacuum polarization, the finite-size contribution, the two-loop electron vacuum polarization and the one-loop muon self energy together with the muon vacuum polarization. Since all the other contributions are smaller than the discrepancy itself, it is improbable that the discrepancy can be explained by miscalculations in one of these [31–33]. But since the two-photon exchange contribution (TPE) cannot be simply computed using deuteron form factors, the explanation of the radius puzzle might also be reached by new calculations of this contribution [34].

A

Numerical results for the cross section

Table A.1 lists the cross section results for each measured setting. The energy of the incoming electron beam is given as E, the central angle of the spectrometer as θ, Q^2 denotes the average Q^2 of the setting, σ_{exp} is the cross section determined by the experiment and σ_{Abbott} the cross section determined by the calculations of Abbott et al. [79].

Table A.1: All measured settings with results for the cross section.

E / MeV	Spec.	$\theta/°$	Q^2 / fm^{-1}	$\frac{\sigma_{exp}}{\sigma_{Abb.}}$	$\Delta\frac{\sigma_{exp}}{\sigma_{Abb.}}$	E / MeV	Spec.	$\theta/°$	Q^2 / fm^{-1}	$\frac{\sigma_{exp}}{\sigma_{Abb.}}$	$\Delta\frac{\sigma_{exp}}{\sigma_{Abb.}}$
180	A	23	0.0054	0.9954	0.0029	180	A	40	0.0146	1.0031	0.0027
180	A	23	0.0054	0.9962	0.0026	180	A	40	0.0146	1.0031	0.0026
180	A	25	0.0060	0.9972	0.0031	180	A	40	0.0146	1.0032	0.0026
180	A	25	0.0060	0.9954	0.0027	180	A	40	0.0146	1.0033	0.0026
180	A	27	0.0070	0.9954	0.0027	180	A	41	0.0157	1.0038	0.0026
180	A	27	0.0070	0.9963	0.0028	180	A	41	0.0157	1.0022	0.0026
180	A	29	0.0080	0.9970	0.0028	180	A	41	0.0157	1.0002	0.0025
180	A	29	0.0080	0.9984	0.0028	180	A	41	0.0157	1.0030	0.0025
180	A	31	0.0091	0.9971	0.0028	180	A	43	0.0168	1.0032	0.0025
180	A	31	0.0090	0.9982	0.0028	180	A	43	0.0168	1.0030	0.0026
180	A	32	0.0096	0.9954	0.0026	180	A	43	0.0168	1.0026	0.0025
180	A	32	0.0096	0.9973	0.0026	180	A	43	0.0168	1.0021	0.0026
180	A	32	0.0096	0.9963	0.0025	180	A	43	0.0168	1.0023	0.0026
180	A	33	0.0102	0.9959	0.0025	180	A	43	0.0180	1.0024	0.0026
180	A	33	0.0102	0.9960	0.0025	180	A	45	0.0180	1.0031	0.0026
180	A	33	0.0105	0.9973	0.0025	180	A	46	0.0191	1.0031	0.0027
180	A	33	0.0106	0.9954	0.0025	180	A	46	0.0192	1.0030	0.0027
180	A	33	0.0105	0.9970	0.0026	180	A	48	0.0203	0.9997	0.0026
180	A	33	0.0105	0.9973	0.0026	180	A	48	0.0203	0.9974	0.0026
180	A	35	0.0113	0.9982	0.0026	180	A	49	0.0215	1.0011	0.0026
180	A	35	0.0113	0.9989	0.0025	180	A	49	0.0214	1.0020	0.0026
180	A	35	0.0116	0.9987	0.0025	180	A	49	0.0214	0.9978	0.0027
180	A	35	0.0114	0.9985	0.0026	180	A	51	0.0228	0.9996	0.0027
180	A	35	0.0114	0.9989	0.0026	180	A	51	0.0228	0.9996	0.0027
180	A	35	0.0114	0.9982	0.0025	180	A	51	0.0228	0.9973	0.0027
180	A	35	0.0114	1.0003	0.0025	180	A	54	0.0251	1.0030	0.0027

Table A.1: All measured settings with results for the cross section. (Continued)

E / MeV	Spec.	$\theta/°$	Q^2 / fm^{-1}	$\frac{\sigma_{exp}}{\sigma_{Abb.}}$	$\Delta\frac{\sigma_{exp}}{\sigma_{Abb.}}$	E / MeV	Spec.	$\theta/°$	Q^2 / fm^{-1}	$\frac{\sigma_{exp}}{\sigma_{Abb.}}$	$\Delta\frac{\sigma_{exp}}{\sigma_{Abb.}}$
180	A	35	0.0114	0.9984	0.0026	180	A	56	0.0265	1.0030	0.0027
180	A	35	0.0114	0.9993	0.0026	180	A	56	0.0265	1.0034	0.0027
180	A	35	0.0114	0.9997	0.0025	180	A	58	0.0277	1.0032	0.0028
180	A	35	0.0114	0.9982	0.0025	180	A	60	0.0301	1.0038	0.0028
180	A	35	0.0113	0.9995	0.0025	180	A	60	0.0301	1.0034	0.0030
180	A	35	0.0114	0.9995	0.0025	180	A	60	0.0301	1.0034	0.0030
180	A	35	0.0114	0.9997	0.0026	180	A	63	0.0323	1.0005	0.0029
180	A	35	0.0114	0.9997	0.0026	180	A	63	0.0323	1.0021	0.0029
180	A	35	0.0113	1.0002	0.0025	180	A	63	0.0348	1.0033	0.0029
180	A	35	0.0113	1.0002	0.0025	180	A	66	0.0348	1.0032	0.0030
180	A	35	0.0113	0.9990	0.0026	180	A	66	0.0348	1.0036	0.0030
180	A	35	0.0113	0.9994	0.0026	180	A	69	0.0370	1.0032	0.0031
180	A	35	0.0116	1.0002	0.0026	180	A	69	0.0370	1.0031	0.0032
180	A	35	0.0115	1.0004	0.0026	180	A	71	0.0392	1.0005	0.0033
180	A	36	0.0124	1.0001	0.0026	180	A	71	0.0392	0.9984	0.0032
180	A	36	0.0124	0.9981	0.0026	180	A	74	0.0415	0.9979	0.0033
180	A	36	0.0124	0.9996	0.0026	180	A	74	0.0415	1.0026	0.0033
180	A	36	0.0124	0.9987	0.0031	180	A	77	0.0437	1.0035	0.0036
180	A	38	0.0135	1.0015	0.0026	180	A	77	0.0437	1.0016	0.0034
180	A	38	0.0135	0.9982	0.0025	180	A	79	0.0460	0.9966	0.0036
180	A	38	0.0135	1.0004	0.0025	180	A	79	0.0459	1.0030	0.0036
180	A	38	0.0135	0.9977	0.0027						
315	A	23	0.0151	0.9982	0.0033	315	A	43	0.0485	1.0019	0.0029
315	A	23	0.0152	0.9982	0.0033	315	A	43	0.0485	1.0015	0.0029
315	A	25	0.0170	0.9987	0.0034	315	A	45	0.0518	1.0019	0.0030
315	A	25	0.0170	0.9987	0.0029	315	A	45	0.0518	0.9954	0.0035
315	A	27	0.0198	0.9981	0.0029	315	A	46	0.0557	0.9981	0.0039
315	A	27	0.0199	0.9981	0.0029	315	A	46	0.0557	0.9991	0.0038
315	A	29	0.0228	0.9984	0.0033	315	A	48	0.0584	0.9947	0.0039
315	A	29	0.0228	0.9986	0.0034	315	A	49	0.0617	0.9994	0.0040
315	A	31	0.0260	0.9982	0.0030	315	A	49	0.0623	0.9994	0.0041
315	A	31	0.0260	1.0015	0.0028	315	A	51	0.0654	0.9967	0.0040
315	A	32	0.0276	0.9999	0.0030	315	A	53	0.0687	0.9975	0.0041
315	A	32	0.0276	0.9980	0.0030	315	A	53	0.0687	0.9974	0.0042
315	A	32	0.0276	0.9985	0.0030	315	A	54	0.0718	0.9977	0.0043
315	A	32	0.0276	1.0011	0.0030	315	A	54	0.0718	0.9984	0.0042
315	A	33	0.0293	0.9983	0.0030	315	A	56	0.0750	0.9980	0.0044
315	A	33	0.0293	0.9990	0.0030	315	A	56	0.0750	0.9979	0.0045
315	A	33	0.0303	1.0002	0.0030	315	A	58	0.0765	0.9983	0.0046
315	A	33	0.0303	0.9982	0.0029	315	A	58	0.0775	0.9993	0.0053
315	A	33	0.0303	1.0000	0.0030	315	A	59	0.0810	0.9983	0.0047
315	A	33	0.0303	0.9992	0.0031	315	A	59	0.0789	0.9985	0.0048
315	A	35	0.0327	1.0038	0.0030	315	A	60	0.0799	0.9971	0.0048

Table A.1: All measured settings with results for the cross section. (Continued)

E / MeV	Spec.	$\theta/°$	Q^2 / fm^{-1}	$\frac{\sigma_{exp}}{\sigma_{Abb.}}$	$\Delta\frac{\sigma_{exp}}{\sigma_{Abb.}}$	E / MeV	Spec.	$\theta/°$	Q^2 / fm^{-1}	$\frac{\sigma_{exp}}{\sigma_{Abb.}}$	$\Delta\frac{\sigma_{exp}}{\sigma_{Abb.}}$
315	A	35	0.0328	1.0052	0.0030	315	A	60	0.0799	0.9970	0.0050
315	A	35	0.0334	1.0056	0.0029	315	A	60	0.0799	0.9971	0.0050
315	A	35	0.0335	1.0056	0.0052	315	A	62	0.0804	0.9975	0.0050
315	A	35	0.0335	1.0028	0.0030	315	A	62	0.0803	0.9967	0.0051
315	A	35	0.0335	1.0050	0.0031	315	A	63	0.0785	0.9972	0.0051
315	A	35	0.0327	1.0056	0.0032	315	A	63	0.0838	0.9948	0.0051
315	A	35	0.0328	1.0015	0.0031	315	A	65	0.0871	0.9992	0.0053
315	A	35	0.0334	1.0040	0.0030	315	A	66	0.0888	1.0002	0.0056
315	A	35	0.0335	1.0012	0.0033	315	A	66	0.0886	0.9996	0.0058
315	A	35	0.0335	1.0019	0.0032	315	A	67	0.0916	0.9974	0.0057
315	A	35	0.0335	1.0047	0.0034	315	A	67	0.0926	0.9990	0.0056
315	A	35	0.0360	1.0012	0.0032	315	A	69	0.0950	0.9990	0.0060
315	A	35	0.0360	1.0021	0.0033	315	A	69	0.0959	0.9991	0.0057
315	A	35	0.0360	1.0012	0.0033	315	A	70	0.0996	0.9979	0.0062
315	A	35	0.0360	1.0038	0.0033	315	A	70	0.0996	0.9977	0.0065
315	A	36	0.0360	0.9984	0.0035	315	A	71	0.1015	0.9970	0.0064
315	A	36	0.0360	1.0004	0.0025	315	A	71	0.1016	0.9948	0.0063
315	A	36	0.0360	0.9984	0.0028	315	A	73	0.1071	0.9939	0.0070
315	A	36	0.0360	1.0000	0.0025	315	A	73	0.1071	0.9940	0.0076
315	A	38	0.0391	0.9975	0.0026	315	A	73	0.1071	0.9938	0.0075
315	A	38	0.0391	1.0000	0.0026	315	A	74	0.1095	0.9947	0.0058
315	A	38	0.0391	0.9961	0.0026	315	A	75	0.1126	0.9939	0.0052
315	A	38	0.0391	0.9988	0.0027	315	A	75	0.1126	0.9936	0.0049
315	A	40	0.0423	0.9995	0.0027	315	A	77	0.1185	0.9936	0.0051
315	A	40	0.0423	0.9994	0.0028	315	A	78	0.1213	0.9938	0.0051
315	A	41	0.0454	0.9978	0.0036	315	A	79	0.1249	0.9938	0.0054
315	A	41	0.0454	1.0022	0.0028						
450	A	23	0.0302	0.9970	0.0030	450	A	35	0.0647	0.9959	0.0050
450	A	23	0.0302	0.9975	0.0029	450	A	35	0.0648	1.0007	0.0041
450	A	25	0.0340	0.9984	0.0031	450	A	35	0.0661	1.0010	0.0040
450	A	25	0.0339	0.9986	0.0030	450	A	35	0.0661	0.9989	0.0040
450	A	27	0.0396	0.9984	0.0032	450	A	36	0.0702	0.9957	0.0042
450	A	27	0.0396	0.9985	0.0032	450	A	36	0.0702	0.9973	0.0043
450	A	29	0.0455	0.9978	0.0034	450	A	36	0.0702	0.9980	0.0043
450	A	29	0.0455	0.9970	0.0033	450	A	36	0.0702	0.9956	0.0043
450	A	31	0.0517	1.0030	0.0036	450	A	36	0.0702	0.9981	0.0048
450	A	31	0.0517	0.9987	0.0036	450	A	36	0.0702	1.0044	0.0060
450	A	32	0.0549	1.0059	0.0037	450	A	38	0.0751	1.0017	0.0045
450	A	32	0.0549	1.0056	0.0037	450	A	38	0.0744	0.9991	0.0045
450	A	32	0.0549	1.0036	0.0040	450	A	38	0.0744	1.0000	0.0047
450	A	32	0.0549	1.0034	0.0039	450	A	38	0.0745	0.9992	0.0047
450	A	33	0.0582	0.9973	0.0045	450	A	40	0.0777	0.9929	0.0048
450	A	33	0.0581	1.0033	0.0044	450	A	40	0.0778	0.9951	0.0057

Table A.1: All measured settings with results for the cross section. (Continued)

E / MeV	Spec.	$\theta/°$	Q^2 / fm^{-1}	$\frac{\sigma_{exp}}{\sigma_{Abb.}}$	$\Delta\frac{\sigma_{exp}}{\sigma_{Abb.}}$	E / MeV	Spec.	$\theta/°$	Q^2 / fm^{-1}	$\frac{\sigma_{exp}}{\sigma_{Abb.}}$	$\Delta\frac{\sigma_{exp}}{\sigma_{Abb.}}$
450	A	33	0.0605	1.0075	0.0048	450	A	40	0.0777	0.9957	0.0048
450	A	33	0.0605	1.0014	0.0046	450	A	40	0.0789	0.9958	0.0049
450	A	33	0.0604	1.0016	0.0048	450	A	41	0.0799	1.0025	0.0051
450	A	33	0.0605	1.0069	0.0043	450	A	41	0.0799	1.0023	0.0050
450	A	35	0.0647	0.9994	0.0043	450	A	41	0.0799	1.0013	0.0050
450	A	35	0.0647	0.9994	0.0042	450	A	41	0.0800	0.9967	0.0049
450	A	35	0.0647	1.0007	0.0043	450	A	43	0.0819	0.9968	0.0052
450	A	35	0.0647	1.0005	0.0045	450	A	43	0.0820	0.9964	0.0052
450	A	35	0.0648	1.0007	0.0044	450	A	43	0.0818	0.9940	0.0054
450	A	35	0.0647	1.0005	0.0044	450	A	43	0.0820	0.9938	0.0054
450	A	35	0.0647	1.0003	0.0044	450	A	43	0.0818	0.9978	0.0054
450	A	35	0.0648	1.0010	0.0040	450	A	43	0.0820	0.9955	0.0054
450	A	35	0.0648	0.9975	0.0040	450	A	45	0.0858	0.9942	0.0059
450	A	35	0.0648	1.0014	0.0037	450	A	45	0.0854	0.9947	0.0077
450	A	35	0.0653	1.0007	0.0037	450	A	45	0.0855	0.9942	0.0058
450	A	35	0.0648	1.0004	0.0037	450	A	45	0.0857	0.9940	0.0092
450	A	35	0.0648	1.0007	0.0039	450	A	45	0.0853	0.9951	0.0055
450	A	35	0.0648	1.0004	0.0039	450	A	45	0.0854	0.9947	0.0055
450	A	35	0.0648	1.0018	0.0040	450	A	46	0.0920	0.9997	0.0061
450	A	35	0.0648	1.0004	0.0040	450	A	46	0.0919	0.9980	0.0060
180	B	21	0.0043	0.9995	0.0019	180	B	27	0.0070	0.9990	0.0018
180	B	21	0.0043	0.9996	0.0019	180	B	27	0.0070	0.9988	0.0018
180	B	21	0.0043	0.9990	0.0019	180	B	27	0.0070	0.9988	0.0018
180	B	21	0.0044	0.9981	0.0019	180	B	27	0.0070	0.9986	0.0018
180	B	22	0.0048	0.9978	0.0019	180	B	27	0.0070	0.9988	0.0018
180	B	22	0.0048	0.9981	0.0018	180	B	27	0.0075	0.9974	0.0018
180	B	22	0.0048	0.9981	0.0018	180	B	28	0.0075	0.9981	0.0018
180	B	22	0.0048	0.9976	0.0018	180	B	28	0.0075	0.9991	0.0018
180	B	23	0.0052	0.9992	0.0018	180	B	29	0.0080	0.9983	0.0018
180	B	23	0.0052	0.9994	0.0018	180	B	29	0.0080	0.9981	0.0018
180	B	23	0.0052	0.9993	0.0018	180	B	29	0.0080	0.9989	0.0018
180	B	24	0.0056	0.9993	0.0018	180	B	30	0.0086	1.0017	0.0018
180	B	24	0.0056	1.0007	0.0018	180	B	30	0.0086	1.0010	0.0018
180	B	24	0.0056	1.0007	0.0018	180	B	30	0.0086	1.0017	0.0017
180	B	24	0.0056	1.0004	0.0018	180	B	31	0.0091	1.0005	0.0017
180	B	25	0.0061	0.9991	0.0020	180	B	32	0.0097	1.0015	0.0017
180	B	25	0.0061	0.9991	0.0017	180	B	32	0.0097	1.0005	0.0018
180	B	25	0.0061	0.9990	0.0018	180	B	33	0.0103	1.0032	0.0018
180	B	25	0.0061	0.9991	0.0018	180	B	33	0.0103	1.0014	0.0018
180	B	26	0.0065	1.0001	0.0018	180	B	34	0.0109	0.9990	0.0018
180	B	26	0.0065	1.0000	0.0018	180	B	34	0.0109	0.9981	0.0017
180	B	26	0.0065	0.9996	0.0018	180	B	35	0.0115	1.0037	0.0018
180	B	26	0.0065	0.9995	0.0018	180	B	37	0.0127	1.0033	0.0017

Table A.1: All measured settings with results for the cross section. (Continued)

E / MeV	Spec.	$\theta/°$	Q^2 / fm^{-1}	$\frac{\sigma_{exp}}{\sigma_{Abb.}}$	$\Delta\frac{\sigma_{exp}}{\sigma_{Abb.}}$	E / MeV	Spec.	$\theta/°$	Q^2 / fm^{-1}	$\frac{\sigma_{exp}}{\sigma_{Abb.}}$	$\Delta\frac{\sigma_{exp}}{\sigma_{Abb.}}$
180	B	27	0.0070	0.9988	0.0017	180	B	37	0.0127	1.0017	0.0017
180	B	27	0.0070	0.9988	0.0018	180	B	37	0.0127	1.0003	0.0018
180	B	27	0.0070	0.9990	0.0018	180	B	39	0.0140	1.0033	0.0018
180	B	27	0.0070	0.9986	0.0018	180	B	39	0.0140	1.0034	0.0018
180	B	27	0.0071	0.9986	0.0018	180	B	41	0.0154	1.0014	0.0018
180	B	27	0.0071	0.9990	0.0018	180	B	41	0.0154	1.0002	0.0018
180	B	27	0.0071	0.9991	0.0018	180	B	43	0.0168	1.0016	0.0018
180	B	27	0.0071	0.9975	0.0022	180	B	43	0.0168	1.0015	0.0018
180	B	27	0.0070	0.9989	0.0018	180	B	45	0.0182	1.0036	0.0018
180	B	27	0.0070	0.9984	0.0018	180	B	47	0.0197	1.0032	0.0020
180	B	27	0.0070	0.9988	0.0018	180	B	47	0.0197	1.0035	0.0017
180	B	27	0.0070	0.9988	0.0018	180	B	47	0.0197	1.0033	0.0018
180	B	27	0.0070	0.9974	0.0018	180	B	49	0.0212	1.0033	0.0018
180	B	27	0.0070	0.9985	0.0018	180	B	49	0.0212	1.0037	0.0017
180	B	27	0.0070	0.9984	0.0018	180	B	51	0.0227	1.0033	0.0018
180	B	27	0.0070	0.9987	0.0018						
315	B	18	0.0096	0.9973	0.0018	315	B	27	0.0210	0.9980	0.0017
315	B	18	0.0096	1.0000	0.0017	315	B	27	0.0210	1.0019	0.0019
315	B	19	0.0107	0.9984	0.0017	315	B	27	0.0210	1.0014	0.0019
315	B	19	0.0107	0.9987	0.0017	315	B	27	0.0210	1.0004	0.0019
315	B	19	0.0107	0.9982	0.0019	315	B	27	0.0210	1.0002	0.0018
315	B	20	0.0118	0.9986	0.0017	315	B	27	0.0210	1.0003	0.0018
315	B	20	0.0118	0.9990	0.0017	315	B	27	0.0210	0.9990	0.0018
315	B	20	0.0118	1.0003	0.0017	315	B	28	0.0225	0.9987	0.0018
315	B	22	0.0142	1.0002	0.0017	315	B	28	0.0225	0.9984	0.0017
315	B	22	0.0142	1.0020	0.0017	315	B	29	0.0240	0.9985	0.0018
315	B	22	0.0142	1.0005	0.0017	315	B	29	0.0240	0.9977	0.0017
315	B	22	0.0142	0.9981	0.0017	315	B	30	0.0256	1.0012	0.0024
315	B	22	0.0142	1.0020	0.0017	315	B	30	0.0256	1.0009	0.0018
315	B	23	0.0154	1.0041	0.0017	315	B	31	0.0273	0.9994	0.0019
315	B	23	0.0154	1.0029	0.0017	315	B	32	0.0289	0.9981	0.0019
315	B	23	0.0154	1.0003	0.0017	315	B	33	0.0309	0.9976	0.0018
315	B	23	0.0154	1.0039	0.0011	315	B	33	0.0309	0.9977	0.0019
315	B	24	0.0168	1.0039	0.0016	315	B	34	0.0324	0.9975	0.0018
315	B	24	0.0168	1.0019	0.0017	315	B	34	0.0324	0.9978	0.0021
315	B	24	0.0168	0.9981	0.0019	315	B	35	0.0342	0.9977	0.0019
315	B	25	0.0182	1.0002	0.0017	315	B	35	0.0342	0.9960	0.0019
315	B	25	0.0182	1.0002	0.0017	315	B	36	0.0360	0.9962	0.0019
315	B	26	0.0196	1.0025	0.0017	315	B	36	0.0360	1.0004	0.0020
315	B	26	0.0196	1.0026	0.0030	315	B	37	0.0378	0.9975	0.0019
315	B	27	0.0210	1.0018	0.0017	315	B	37	0.0378	0.9977	0.0019
315	B	27	0.0210	1.0003	0.0017	315	B	37	0.0378	0.9983	0.0019
315	B	27	0.0210	0.9995	0.0017	315	B	38	0.0397	0.9988	0.0020

Table A.1: All measured settings with results for the cross section. (Continued)

E / MeV	Spec.	$\theta/°$	Q^2 / fm^{-1}	$\frac{\sigma_{exp}}{\sigma_{Abb.}}$	$\Delta\frac{\sigma_{exp}}{\sigma_{Abb.}}$	E / MeV	Spec.	$\theta/°$	Q^2 / fm^{-1}	$\frac{\sigma_{exp}}{\sigma_{Abb.}}$	$\Delta\frac{\sigma_{exp}}{\sigma_{Abb.}}$
315	B	27	0.0210	0.9995	0.0016	315	B	38	0.0397	0.9981	0.0022
315	B	27	0.0210	0.9990	0.0018	315	B	39	0.0417	0.9994	0.0022
315	B	27	0.0210	1.0023	0.0017	315	B	39	0.0417	0.9992	0.0022
315	B	27	0.0210	0.9987	0.0017	315	B	40	0.0436	1.0000	0.0022
315	B	27	0.0210	1.0035	0.0018	315	B	41	0.0456	1.0016	0.0027
315	B	27	0.0210	0.9992	0.0018	315	B	41	0.0456	1.0013	0.0037
315	B	27	0.0210	1.0027	0.0018	315	B	42	0.0477	1.0016	0.0024
315	B	27	0.0210	0.9975	0.0019	315	B	42	0.0477	1.0015	0.0026
315	B	27	0.0210	0.9982	0.0018						
450	B	15	0.0137	0.9972	0.0021	450	B	23	0.0316	0.9966	0.0023
450	B	15	0.0137	1.0017	0.0021	450	B	23	0.0316	0.9959	0.0024
450	B	15	0.0137	1.0062	0.0020	450	B	24	0.0343	1.0051	0.0024
450	B	15	0.0137	1.0048	0.0019	450	B	24	0.0343	1.0018	0.0023
450	B	15	0.0137	1.0057	0.0020	450	B	24	0.0343	1.0014	0.0023
450	B	16	0.0155	1.0024	0.0021	450	B	24	0.0343	0.9993	0.0028
450	B	16	0.0155	1.0036	0.0021	450	B	24	0.0343	1.0044	0.0023
450	B	16	0.0155	1.0048	0.0021	450	B	25	0.0371	0.9998	0.0025
450	B	16	0.0155	1.0043	0.0021	450	B	25	0.0371	0.9992	0.0024
450	B	17	0.0175	0.9993	0.0028	450	B	25	0.0371	1.0005	0.0025
450	B	17	0.0175	0.9974	0.0021	450	B	25	0.0371	0.9965	0.0025
450	B	17	0.0175	0.9947	0.0020	450	B	26	0.0400	1.0020	0.0026
450	B	18	0.0196	0.9992	0.0020	450	B	26	0.0400	1.0008	0.0026
450	B	18	0.0196	0.9984	0.0021	450	B	26	0.0400	0.9957	0.0026
450	B	19	0.0218	1.0045	0.0021	450	B	26	0.0400	0.9984	0.0026
450	B	19	0.0218	1.0032	0.0022	450	B	27	0.0430	1.0003	0.0026
450	B	19	0.0218	1.0043	0.0022	450	B	27	0.0430	0.9998	0.0026
450	B	19	0.0218	1.0027	0.0022	450	B	27	0.0430	0.9963	0.0026
450	B	20	0.0241	1.0011	0.0023	450	B	27	0.0430	1.0023	0.0026
450	B	20	0.0241	0.9991	0.0023	450	B	27	0.0430	0.9995	0.0025
450	B	20	0.0241	0.9983	0.0022	450	B	27	0.0430	0.9973	0.0033
450	B	20	0.0241	0.9939	0.0022	450	B	27	0.0430	1.0041	0.0025
450	B	21	0.0265	1.0011	0.0022	450	B	27	0.0430	0.9987	0.0026
450	B	21	0.0265	0.9953	0.0021	450	B	27	0.0430	1.0024	0.0026
450	B	21	0.0265	0.9960	0.0028	450	B	27	0.0430	0.9968	0.0025
450	B	21	0.0265	0.9953	0.0022	450	B	27	0.0430	0.9977	0.0025
450	B	22	0.0290	0.9979	0.0024	450	B	27	0.0430	0.9995	0.0026
450	B	22	0.0290	0.9979	0.0023	450	B	27	0.0430	0.9965	0.0026
450	B	22	0.0290	0.9955	0.0023	450	B	27	0.0430	1.0013	0.0026
450	B	22	0.0290	0.9953	0.0042	450	B	27	0.0430	0.9984	0.0025
450	B	22	0.0290	0.9951	0.0024	450	B	27	0.0430	0.9979	0.0026
450	B	22	0.0290	0.9949	0.0023	450	B	28	0.0461	0.9989	0.0027
450	B	23	0.0316	0.9985	0.0023	450	B	28	0.0461	1.0039	0.0027
450	B	23	0.0316	0.9960	0.0026	450	B	28	0.0461	1.0009	0.0027

Table A.1: All measured settings with results for the cross section. (Continued)

E / MeV	Spec.	$\theta/^\circ$	Q^2 / fm^{-1}	$\frac{\sigma_{exp}}{\sigma_{Abb.}}$	$\Delta\frac{\sigma_{exp}}{\sigma_{Abb.}}$	E / MeV	Spec.	$\theta/^\circ$	Q^2 / fm^{-1}	$\frac{\sigma_{exp}}{\sigma_{Abb.}}$	$\Delta\frac{\sigma_{exp}}{\sigma_{Abb.}}$
450	B	23	0.0316	0.9969	0.0030	450	B	28	0.0461	1.0013	0.0027

B

Interchangeable luminosity monitors

For all measurements, one of the spectrometers was utilized as a luminosity monitor, i.e. this spectrometer stayed with the same field at the same angle thus measuring the count rate for a fixed momentum transfer for a time when runs at at least two different angles were executed with the other spectrometers. This spectrometer monitors the luminosity. While spectrometer C stayed at the same angle, spectrometer A and B were used to execute runs at many different angles. To make this possible and to keep the 50° spacing between spectrometer B and C as mentioned in 3.3, spectrometer C had to be at a significantly higher angle than the other two spectrometers. Unfortunately this gave rise to low count rates in spectrometer C for most of the runs, since the count rate for electron scattering decreases for higher angles significantly and the beam current was always optimized for sufficient count rates in spectrometer A and B. On this account spectrometer C could not be used to get a luminosity reading for all runs and a different approach was chosen. The fact that spectrometer A and B were never moved to a new angle at the same time rendered it possible to instrumentalize these spectrometers interchangeably as luminosity monitors.
In addition to the procedure to calculate the luminosity when only one spectrometer is used as a luminosity monitor (as described in 4.5), for interchangeable luminosity monitors a distinction of cases has to be done:
The first case is equivalent to using only one spectrometer as a luminosity monitor. That is the case if spectrometer A and B stayed at the same angle for consecutive runs. Then spectrometer A is employed for the calculation. Since the prescaler was never changed, when the angle stayed the same for both spectrometer, the prescaler can be left out of the calculation:

$$\theta_{A,i} = \theta_{A,i-1}, \theta_{B,i} = \theta_{B,i-1}: \qquad I_i = I_{i-1}\frac{E_{A,i} \cdot t_{i-1}}{E_{A,i-1} \cdot t_i} \tag{B.1}$$

In the second case, when only for spectrometer B an angle change was present, spectrometer A is used for the calculation:

$$\theta_{A,i} = \theta_{A,i-1}, \theta_{B,i} \neq \theta_{B,i-1}: \qquad I_i = I_{i-1}\frac{E_{A,i} \cdot PS_{A,i} \cdot t_{i-1}}{E_{A,i-1} \cdot PS_{A,i-1} \cdot t_i} \tag{B.2}$$

In the third and last case only spectrometer A changed the angle, therefore spectrometer B is used for the calculation:

$$\theta_{A,i} \neq \theta_{A,i-1}, \theta_{B,i} = \theta_{B,i-1}: \qquad I_i = I_{i-1} \frac{E_{B,i} \cdot PS_{B,i} \cdot t_{i-1}}{E_{B,i-1} \cdot PS_{B,i-1} \cdot t_i} \tag{B.3}$$

This distinction of cases is done for each energy separately. For each energy a starting value I_0 for the current is needed, since the equation is each time defined recursively. As a starting value the corresponding picoamperemeter current was chosen.

The disadvantage of this procedure to calculate the luminosity is that the error

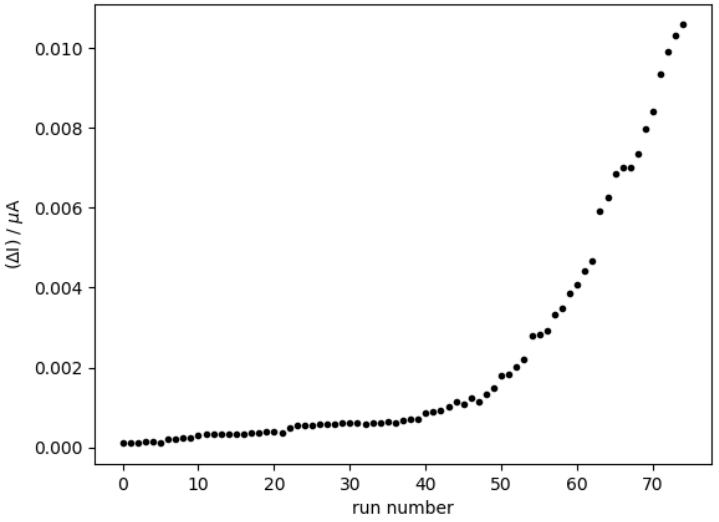

Figure B.1: The error on the luminosity is increasing with higher current, shown here for all runs at 315 MeV. Also here the common factors of the calculations are not considered and the error on the current is shown representative.

for the luminosity value increases with each iteration, since the error of the previous run always enters the error propagation equation for the next run. Due to that circumstance one gets an around 100 times larger error on the last luminosity of the last run at one energy than on the first one, as can be seen in fig. B.1 for an energy of 315 MeV. Especially for the higher currents also the relative error shows an increase (see fig. B.2). To avoid this large error for the further analysis, the picoamperemeter values are used from now on for all following steps of the analysis. This is possible, because the luminosity values calculated with the procedure described in this section agree with the ones measured with the picoamperemeter, as shown in 4.5.

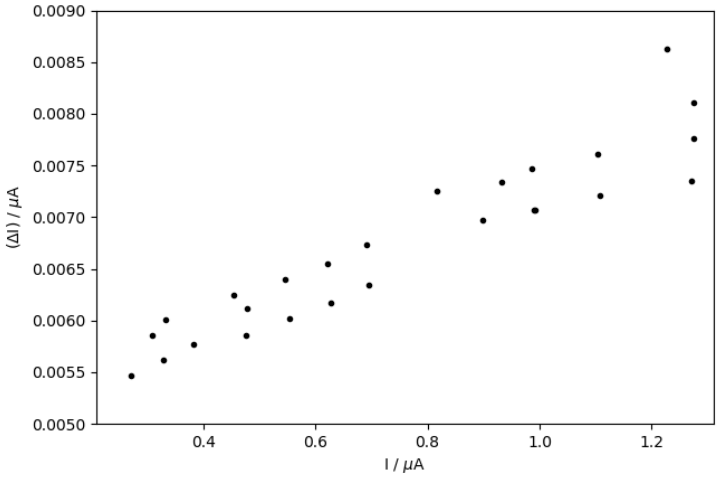

Figure B.2: The relative error on the luminosity is also increasing with higher current, shown here for 315 MeV. Also here the common factors of the calculations are not considered and the error on the current is shown representative.

C

Target class

In the A1 software package *Cola++/Simul++* the target is handled with the file *Targetlength.cc*. This file holds classes for the different kinds of targets, which can be used for the A1 experiments. Within the scope of this thesis an updated and more detailed version of the old class *cryo_ cyl* was written. The new class *cryo_ cyl_ 2014* takes care of the round cryogenic target cell, which was used in the electron deuteron scattering experiment. In this class the geometry and material of the cell is used to calculate the energy losses of electrons which traverse the cell. Depending on whether data (*Cola++*) or simulation (*Simul++*) is processed, different functions of the class are called.
Input parameters are needed for the class, which are stored in a run database text file (*run.db*). There the geometrical quantities like lengths and thicknesses as well as the densities of the different components of the cell are stored. The basic geometry of the cell is hard coded but values like the thickness of the cell wall can be varied for different runs. For example the empty target cell, which was build for this thesis uses the same target class, although the empty target cell has thicker walls than the cryogenic cell.

C.1 Calculation of lengths inside the target

One important function of the class is called *getLength_ in_ Target*. This function is used to calculate all the distances, which are needed for the energy loss calculations, like the distance the electron traveled through the deuterium, through the front and back part of the cell walls and the same for the cryogenic depositions. For these distance calculations the function receives the coordinates of the scattering vertex, the angles ϕ and θ of the scattered electron and the modeltype which specifies the model for the simulation (*ElasticDeuteron* for the deuteron, *ElasticNucleus* for the HAVAR wall, *ElasticCryogens* for the cryogenic deposition, ..). In fig. C.1 examples for the different possible vertex positions are shown. Most of the electrons will scatter somewhere inside the deuterium (1). On the other hand it is also possible that they scatter in the front (2), back (3) or side part of the HAVAR wall. Even less electrons are scattered in the cryogenic depositions (5,6,7). The basis for all the calculations can be illustrated in two dimensions with fig. C.2. In two dimensions

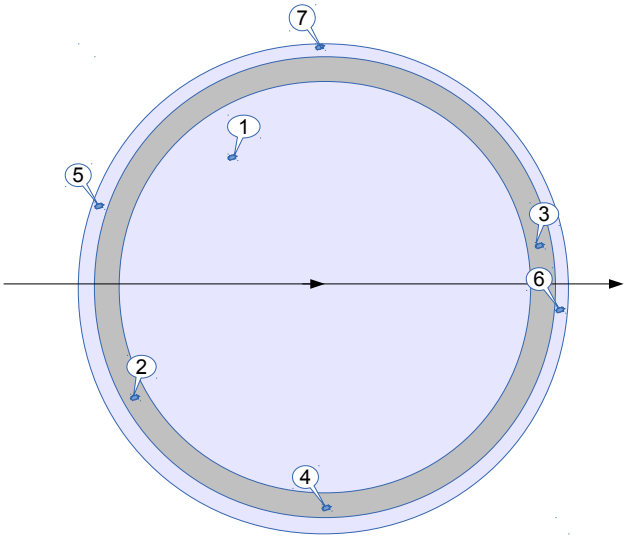

Figure C.1: All possible vertex positions in the target cell. Most of the electrons will scatter somewhere inside the deuterium (1). Some in the front (2), back (3) or side part of the HAVAR wall. Even less electrons than at the wall are scattered in the cryogenic depositions (5,6,7).

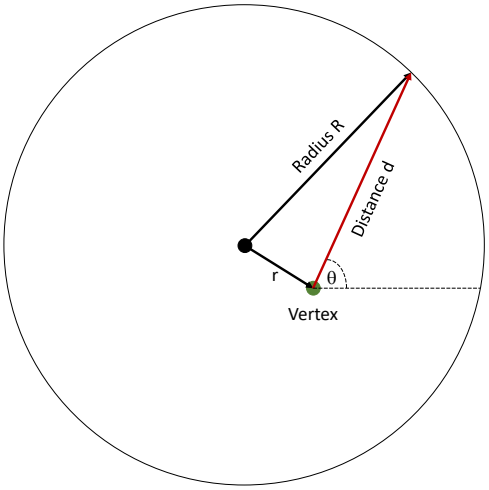

Figure C.2: Illustration of some distances in two dimensions in the target cell. The dotted line shows the beam axis.

the vectors are given as following:

$$\begin{aligned} \vec{d} &= d \begin{pmatrix} \sin\theta \\ \cos\theta \end{pmatrix} \\ \vec{r} &= \begin{pmatrix} x \\ z \end{pmatrix} \end{aligned} \tag{C.1}$$

The radius of the target cell as well as the vector $\vec{r}$ are always known based on the function arguments. With these two vectors you can determine the distance d ($Distance\_to\_BackWall$) as it is shown in eq. C.2:

$$\begin{aligned} \vec{d} &= \vec{R} - \vec{r} \\ |\vec{d} + \vec{r}|^2 &= |\vec{R}|^2 \\ \vec{d}^2 + 2\vec{d}\vec{r} + \vec{r}^2 &= \vec{R}^2 \\ d^2 + d\underbrace{2(x\sin(\theta) + z\cos(\theta))}_{p} + \underbrace{x^2 + z^2 - R^2}_{q} &= 0 \\ d^2 + pd + q &= 0 \\ d &= -\frac{p}{2} \pm \sqrt{\frac{p^2}{4} - q} \end{aligned} \tag{C.2}$$

If one is using the radius of the outside of the cell (radius + wall thickness) one receives the distance from the vertex to the end of the cell ($Distance\_to\_EndOfCell$). The difference of $Distance\_to\_EndOfCell$ and $Distance\_to\_BackWall$ results in the length inside the wall.
By changing the angles as if the electron traveled back from the vertex to the front wall in opposite beam direction the distances to the front part of the cell can be calculated with the same formulas.
The remaining distances that are needed are located inside the possible cryogenic depositions on the target cell. These are calculated in analogy to the distances inside the wall by using the radius to the outside of the depositions (radius + wall thickness + thickness of the depositions).

C.2 Simulated energy loss in *Targetlength.cc* for target *cryo_cyl_2014*

The energy loss in the simulation is separated into two parts and is handled by different functions, respectively:

- *EnergyLossSimBeam* handles the energy loss before the vertex
- *EnergyLossSim* handles the energy loss after the vertex

C.2.1 *EnergyLossSimBeam*

This function distinguishes between simulation for deuterium/hydrogen, the HAVAR walls and the cryogenic depositions.

C.2.1.1 Energy loss for target material simulation

If the model for deuterium (hydrogen): *ElasticDeuteron* (*ElasticProton*) is chosen following energy losses are done:
An electron whose vertex is inside the target material (1) in figure C.1 first looses energy and (or) changes its momentum direction in the possible cryogenic depositions on the outside of the target walls by:

- Landau Loss
- External Bremsstrahlung
- Multiscattering

(Since these are the standard energy losses, which are used in each case, they will be called standard losses for the other cases.) For all three standard losses the energy loss happens over the distance, which the particle is traveling inside the cryogenic depositions. In the end this equals the thickness of the depositions. After the electron passes the cryogenic depositions, it has to pass the front wall of the target cell, in which it is again loosing energy by the standard losses. Here the distance over which the energy is lost is the distance inside the wall, which considers the differences of distances inside the wall if the electron is reaching the wall non centric to the beam centre (x-coordinate $\neq 0$).
When the electron reaches the target material it is also loosing energy in this material. Since scattering happens here, there are the standard energy losses and the internal Bremsstrahlung to consider.

C.2.1.2 Energy loss for wall material simulation

If a model for the target walls (*ElasticNucleus* or *QuasiElasticNucleus*) is chosen, the procedure is as following:
To check which energy losses are needed the vertex position is determined, since it is possible that the scattering happens in the front-, in the back- or even (in principle) in the sidewall. If the z-coordinate of the vertex is less than zero, the scattering took place in the front wall. In this case the electron first looses energy in the possible cryogenic depositions at the front wall by the standard losses over the distance, which the particle is passing inside the cryogenic depositions and this equals the thickness of the depositions. After it passes this part the electron looses energy in the front wall by the standard losses over the distance inside the wall up to the vertex.
If the z-coordinate of the vertex is larger than zero the scattering took place in the back wall. Also in this case the first energy is lost in the possible cryogenic

depositions and the front wall by the standard losses. After the front wall the electron passes through the target cell volume where it interacts non-elastically by loosing energy in the target material (for the empty cell the density of the target material is set to 0.0001 $\frac{g}{cm^3}$ in *run.db* to get nearly zero energy loss for an empty cell) by the standard losses. The last part of the energy loss in this case happens inside the back wall before the scattering takes place by the standard losses and internal Bremsstrahlung.
There is one possibility left, where the scattering could take place: In the side wall, this means the x-coordinate of the vertex is larger than 10 mm. Electrons which are scattering here, first have to pass the cryogenic depositions on the front wall and they are loosing energy in these depositions by the standard losses. After the cryogenic depositions the electron looses energy in the wall by the standard losses and the internal Bremsstrahlung.

C.2.1.3 Energy loss for cryogenic deposition simulation

If a model for the cryogenic depositions (*ElasticCryogens*) is chosen, the procedure is analog to the one described for the energy loss in the wall material.

C.2.2 *EnergyLossSim*

This function distinguishes between simulation for deuterium/hydrogen, the HAVAR walls and the cryogenic depositions and considers the same cases for the vertex position as *EnergyLossSimBeam*. But now the energy losses after the vertex are calculated. Since these are analog to the ones described in the previous subsection, there is no detailed description of the losses for each case.
For all cases in *EnergyLossSim* there is also the possibility that the particle is not an electron. If this is the case, the energy loss is done with Bethe-Bloch instead of the described losses.

D

Determination of the interpolation of the errors for the empty cell background

For the interpolation of the errors for the empty cell background the uncertainties for this background at different angles were determined. In fig. D.1 it can be seen that the values for the uncertainty do not follow a linear function, when plotted against the scattering angle. In 4.7 it is described that the factor, which was used for the interpolation between the minimum and maximum estimated uncertainty, is multiplied onto the cross section values in a linear fashion. To validate this procedure it was checked how the result for the uncertainties would change if a different interpolation was being used. In this context the procedure described in 4.7 was on the one hand also performed with an interpolation consisting of two linear parts, one with a steeper slope for angles up to 40° and one with a lesser slope for the higher angles and on the other hand with a polynomial function which was fitted to the data points in fig. D.1. Comparing the results from these procedure with the

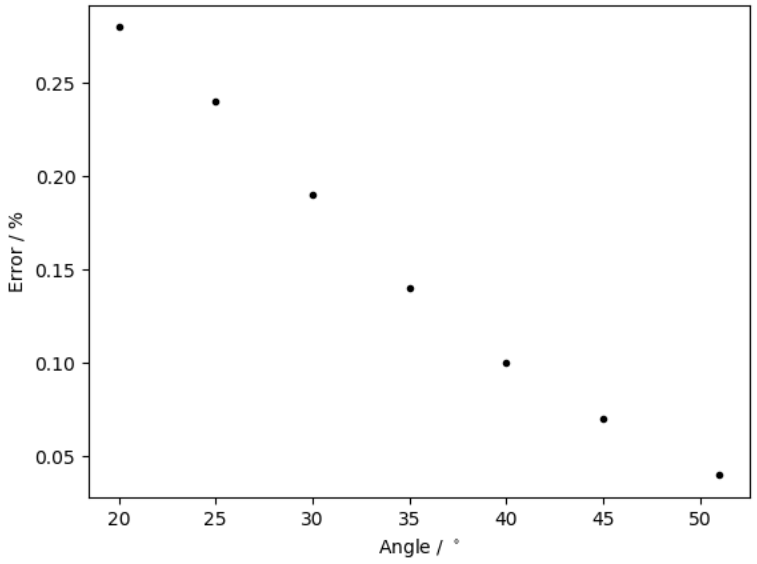

Figure D.1: Uncertainty for the empty cell background for different values of the scattering angle.

linear ansatz showed that the error did not change on the significant digits. So it was decided to use the less complex procedure with the linear ansatz.

List of Tables

List of Figures

Bibliography

[1] E. Rutherford. The scattering of alpha and beta particles by matter and the structure of the atom. *Phil. Mag. Ser.6* (1911). 21: 669–688.

[2] H. Geiger et al. On a diffuse reflection of the α-particles. *Proceedings of the Royal Society of London A: Mathematical, Physical and Engineering Sciences* (1909). 82(557): 495–500.

[3] J. J. Thomson. Cathode rays. *Philosophical Magazine* (1897). 44: 293.

[4] W. Wien. Über positive Elektronen und die Existenz hoher Atomgewichte. *Annalen der Physik* (1904). Band 318: 669–677.

[5] E. Rutherford. Collision of alpha Particles with Light Atoms; An Anomalous Effect in Nitrogen. *Phil. Mag* (1919). 37.

[6] J. Chadwick. Possible existance of a neutron. *Nature* (1932). 129.

[7] R. G. Lerner et al. *ENCYCLOPEDIA OF PHYSICS*. VCH Publishers, Inc., zweite Auflage (1991).

[8] P. A. M. Dirac. The quantum theory of the electron. *Proceedings of the Royal Society of London A: Mathematical, Physical and Engineering Sciences* (1928). 117(778): 610–624.

[9] T. Kinoshita et al. Improved α^4 term of the electron anomalous magnetic moment. *Phys. Rev. D* (2006). 73.

[10] B. Odom et al. New measurement of the electron magnetic moment using a one-electron quantum cyclotron. *Physical Review Letters* (2006). 97.

[11] G. Gabrielse et al. Erratum: New Determination of the Fine Structure Constant from the Electron g Value and QED [Phys. Rev. Lett. 97, 030802 (2006)]. *Phys. Rev. Lett.* (2007). 99.

[12] R. Frisch et al. Über die magnetische Ablenkung von Wasserstoffmolekülen und das magnetische Moment des Protons. I. *Zeitschrift für Physik* (1933). 85(1).

[13] I. Estermann et al. Über die magnetische Ablenkung von Wasserstoffmolekülen und das magnetische Moment des Protons. II. *Zeitschrift für Physik* (1933). 85(1).

[14] H. Nishino et al. Search for Proton Decay via $p \to e^+\pi^0$ and $p \to \mu^+\pi^0$ in a Large Water Cherenkov Detector. *Phys. Rev. Lett.* (2009). 102: 141801.

[15] E. E. Chambers et al. Structure of the Proton. *Phys. Rev.* (1956). 103: 1454.

[16] R. Hofstadter et al. Electron Scattering from the Proton. *Phys. Rev.* (1955). 98.

[17] R. Hofstadter. Electron Scattering and Nuclear Structure. *Rev. Mod. Phys.* (1956). 28: 214.

[18] G. Simon et al. Absolute electron-proton cross sections at low momentum transfer measured with a high pressure gas target system. *Nuclear Physics A* (1980). 333(3): 381 – 391.

[19] J. Friedrich et al. A coherent interpretation of the form factors of the nucleon in terms of a pion cloud and constituent quarks. *The European Physical Journal A - Hadrons and Nuclei* (2003). 17(4): 607–623.

[20] M. K. Jones et al. G_{E_p}/G_{M_p} Ratio by Polarization Transfer in $\vec{e}\ p \rightarrow e\ \vec{p}$. *Phys. Rev. Lett.* (2000). 84: 1398–1402.

[21] J. Arrington et al. Review of two-photon exchange in electron scattering. *Progress in Particle and Nuclear Physics* (2011). 66(4): 782 – 833.

[22] J. Arrington et al. Hard probes of short-range nucleon–nucleon correlations. *Progress in Particle and Nuclear Physics* (2012). 67(4): 898 – 938.

[23] J. J. Krauth et al. The proton radius puzzle. *arXiv:1706.00696* (2017).

[24] P. J. Mohr et al. CODATA recommended values of the fundamental physical constants: 2014. *Rev. Mod. Phys.* (2016). 88: 035009.

[25] P. Amaro et al. Quantum interference effects in laser spectroscopy of muonic hydrogen, deuterium, and helium-3. *Phys. Rev. A* (2015). 92: 022514.

[26] U. Jentschura. Lamb shift in muonic hydrogen—I. Verification and update of theoretical predictions. *Annals of Physics* (2011). 326(2): 500 – 515.

[27] C. G. Parthey et al. Improved Measurement of the Hydrogen $1S^{\smile}2S$ Transition Frequency. *Phys. Rev. Lett.* (2011). 107: 203001.

[28] B. de Beauvoir et al. Metrology of the hydrogen and deuterium atoms: Determination of the Rydberg constant and Lamb shifts. *The European Physical Journal D - Atomic, Molecular, Optical and Plasma Physics* (2000). 12(1): 61–93.

[29] R. Pohl et al. Muonic Hydrogen and the Proton Radius Puzzle. *Annual Review of Nuclear and Particle Science* (2013). 63(1): 175–204.

[30] A. Beyer et al. Precision spectroscopy of 2S– n P transitions in atomic hydrogen for a new determination of the Rydberg constant and the proton charge radius. *Physica Scripta* (2015). 2015(T165): 014030.

[31] A. Antognini et al. Theory of the 2S–2P Lamb shift and 2S hyperfine splitting in muonic hydrogen. *Annals of Physics* (2013). 331: 127 – 145.

[32] K. Pachucki. Theory of the Lamb shift in muonic hydrogen. *Phys. Rev. A* (1996). 53: 2092–2100.

[33] K. Pachucki. Proton structure effects in muonic hydrogen. *Phys. Rev. A* (1999). 60: 3593–3598.

[34] G. A. Miller. Proton polarizability contribution: Muonic hydrogen Lamb shift and elastic scattering. *Physics Letters B* (2013). 718(3): 1078 – 1082.

[35] I. Sick et al. Proton root-mean-square radii and electron scattering. *Phys. Rev. C* (2014). 89: 012201.

[36] J. C. Bernauer et al. Electric and magnetic form factors of the proton. *Phys. Rev. C* (2014). 90: 015206.

[37] G. Lee et al. Extraction of the proton radius from electron-proton scattering data. *Phys. Rev. D* (2015). 92: 013013.

[38] I. T. Lorenz et al. Theoretical constraints and systematic effects in the determination of the proton form factors. *Phys. Rev. D* (2015). 91: 014023.

[39] Mihovilovič, M. et al. Initial state radiation experiment at MAMI. *EPJ Web of Conferences* (2014). 72: 00017.

[40] P. Indelicato. Talk. In *10TH EUROPEAN RESEARCH CONFERENCE ON "ELECTROMAGNETIC INTERACTIONS WITH NUCLEONS AND NUCLEI"*. Cyprus (2013) .

[41] P. J. Mohr et al. CODATA Recommended Values of the Fundamental Physical Constants:2010. *Rev. Mod. Phys.* (2012).

[42] I. Sick. Elastic Electron Scattering from Light Nuclei. *Progress in Particle and Nuclear Physics* (2001). 47(1): 245 – 318.

[43] N. F. Mott. The Scattering of Fast Electrons by Atomic Nuclei. *Proceedings of the Royal Society of London. Series A, Containing Papers of a Mathematical and Physical Character* (1929). 124(794): 425–442.

[44] R. Hofstadter. Nuclear and nucleon scattering of high-energy electrons. *Annual Review of Nuclear Science* (1957). 7(1): 231–316.

[45] M. N. Rosenbluth. High Energy Elastic Scattering of Electrons on Protons. *Phys. Rev.* (1950). 79: 615–619.

[46] R. Berard et al. Elastic electron deuteron scattering. *Physics Letters B* (1973). 47(4): 355 – 358.

[47] G. Simon et al. Elastic electric and magnetic e-d scattering at low momentum transfer. *Nuclear Physics A* (1981). 364(2–3): 285 – 296.

[48] S. Platchkov et al. The deuteron A(Q2) structure function and the neutron electric form factor. *Nuclear Physics A* (1990). 510(4): 740 – 758.

[49] R. Pohl et al. The size of the proton. *Nature* (2010). 466(7303): 213–216.

[50] D. Abbott et al. Precise Measurement of the Deuteron Elastic Structure Function $A(Q^2)$. *Phys. Rev. Lett.* (1999). 82: 1379–1382.

[51] L. C. Maximon et al. Radiative corrections to electron-proton scattering. *Phys. Rev. C* (2000). 62: 054320.

[52] Y.-S. Tsai. Radiative Corrections to Electron-Proton Scattering. *Phys. Rev.* (1961). 122: 1898–1907.

[53] M. Vanderhaeghen et al. QED radiative corrections to virtual Compton scattering. *Phys. Rev. C* (2000). 62: 025501.

[54] J. M. Friedrich. *Messung der Virtuellen Comptonstreuung an MAMI zur Bestimmung Generalisierter Polarisierbarkeiten des Protons.* Doktorarbeit, Institut für Kernphysik, Johannes Gutenberg-Universität Mainz (2000).

[55] W. A. McKinley et al. The Coulomb Scattering of Relativistic Electrons by Nuclei. *Phys. Rev.* (1948). 74: 1759–1763.

[56] H. Herminghaus et al. The design of a cascaded 800 MeV normal conducting C.W. race track microtron. *Nuclear Instruments and Methods* (1976). 138(1): 1 – 12.

[57] A. Jankowiak. *Many Body Structure of Strongly Interacting Systems: Refereed and selected contributions from the symposium "20 Years of Physics at the Mainz Microtron MAMI"*, 149–160. Springer Berlin Heidelberg, Berlin, Heidelberg (2006).

[58] K.-H. Kaiser et al. The 1.5 GeV harmonic double-sided microtron at Mainz University. *Nuclear Instruments and Methods in Physics Research Section A: Accelerators, Spectrometers, Detectors and Associated Equipment* (2008). 593(3): 159 – 170.

[59] K. Blomqvist et al. The three-spectrometer facility at the Mainz microtron MAMI. *Nuclear Instruments and Methods in Physics Research Section A: Accelerators, Spectrometers, Detectors and Associated Equipment* (1998). 403(2): 263 – 301.

[60] M. O. Distler. *Elektroproduktion von neutralen Pionen am Wasserstoff an der Schwelle.* Doktorarbeit, Institut für Kernphysik, Johannes Gutenberg-Universität Mainz (1996).

[61] S. Schardt. *Aufbau und Erprobung der Drei-Spektrometer-Anordnung für Koinzidenzexperimente mit Elektronen am 855 MeV-Elektronenbeschleuniger MAMI.* Doktorarbeit, Institut für Kernphysik, Johannes Gutenberg-Universität Mainz (1994).

[62] M. O. Distler. *Aufbau und Test einer vertikalen Driftkammer.* Diplomarbeit, Institut für Kernphysik, Johannes Gutenberg-Universität Mainz (1990).

[63] M. Kahrau. *Aufbau der vertikalen Driftkammern des Spektrometers C an MAMI.* Diplomarbeit, Institut für Kernphysik, Johannes Gutenberg-Universität Mainz (1993).

[64] A. W. Richter. *Trennung des longitudinalen, transversalen und longitudinal-transversal interferierenden Anteils des Wirkungsquerschnitts der Reaktion H(e,e'π*) in der Nähe der Pionschwelle.* Doktorarbeit, Institut für Kernphysik, Johannes Gutenberg-Universität Mainz (1994).

[65] *Praxair Speciality gases reference guide.*

[66] Philips Wissenschaftliche Apparate Datenblatt zur Gaskälteanlage für experimentelle Zwecke PEH 100/110 (Hamburg 1968).

[67] C.-G. Schilling. *Aufbau und Eichung eines Flüssig Deuterium Targets für hohe Strahlströme.* Diplomarbeit, Institut für Kernphysik, Johannes Gutenberg-Universität Mainz (1994).

[68] T. Pospischil. *Aufbau und Inbetriebnahme eines Protonen-Polarimeters an MAMI und Messung der Proton-Polarisation in der Reaktion* $p(e, e'P)\pi^0$. Doktorarbeit, Institut für Kernphysik, Johannes Gutenberg-Universität Mainz (2000).

[69] J. Bernauer. *Vorbereitung zur hochpräzisen Messung des elektrischen und magnetischen Formfaktors von Protonen.* Diplomarbeit, Johannes Gutenberg- Universität Mainz (2004).

[70] M. O. Distler et al. Measurement of the elastic A(Q^2) form factor of the deuteron at very low momentum transfer and the extraction of the monopole charge radius of the deuteron (2012).

[71] J. Bernauer. *Measurement of elastic electron-proton cross section and separation of the electric and magnetic form factor in the* Q^2 *range from 0.004 to 1* $(GeV/c)^2$. Doktorarbeit, Institut für Kernphysik, Johannes Gutenberg-Universität Mainz (2010).

[72] National Institute of Standards and Technology (2013).

[73] M. O. Distler et al. Data aquisition and analysis for the 3-spectrometer-setup at MAMI. In *Proceedings of the 12th IEEE Real Time Congress on Nuclear and Plasma Science* (2001) .

[74] M. E. Rose. The Charge Distribution in Nuclei and the Scattering of High Energy Electrons. *Phys. Rev.* (1948). 73: 279–284.

[75] J. Friedrich et al. The salient features of charge density distributions of medium and heavy even-even nuclei determined from a systematic analysis of elastic electron scattering form factors. *Nuclear Physics A* (1982). 373(2): 192 – 224.

[76] M. G. C. Dally, E. B. et al. Scattering of High-Energy Electrons by Nitrogen-14 and -15. *Phys. Rev. C* (1970). 2: 2057–2068.

[77] M. Korn. *Entwicklung des Bahnrückverfolgungsverfahrens für die Drei-Spektrometer-Anlage und experimentelle Bestimmung der Abbildungseigenschaften der Spektrometer A und B mit elastischer Elektronenstreuung.* Doktorarbeit, Institut für Kernphysik, Johannes Gutenberg-Universität Mainz (1994).

[78] I. Sick. Model-independent nuclear charge densities from elastic electron scattering. *Nuclear Physics A* (1974). 218(3): 509 – 541.

[79] D. Abbott et al. Phenomenology of the deuteron electromagnetic form factors - The Jefferson Lab t_{20} Collaboration. *Eur. Phys. J. A* (2000). 7(3): 421–427.

[80] M. Dehn. private communication (2014).

[81] V. A. Babenko et al. Determination of the root-mean-square radius of the deuteron from present-day experimental data on neutron-proton scattering. *Physics of Atomic Nuclei* (2008). 71(10): 1730–1739.

[82] I. Sick et al. On the rms radius of the deuteron. *Nuclear Physics A* (1998). 637(4): 559 – 575.

[83] R. Pohl et al. Laser spectroscopy of muonic deuterium. *Science* (2016). 353(6300): 669–673.

[84] R. A. Arndt et al. Nucleon-nucleon elastic scattering to 3 GeV. *Phys. Rev. C* (2000). 62: 034005.

[85] H. Merkel, Hg. *Internal Target Experiments at the MESA accelerator* (2016).

[86] Wittig. $http://www.uni-mainz.de/presse/19433_ENG_HTML.php$ (2018).

[87] S. Griesera et al. A Cryogenic Supersonic Jet Target for Electron Scattering Experiments at MAGIX@MESA and MAMI. *arXiv* (2018).

[88] T. Henmann et al. A consistent calculation of dispersion corrections in elastic electron-deuteron scattering. *Eur. Phys. J. A2* (1998). 29–40.

Acknowledgement

Firstly I would like to express my gratitude to my advisor for the opportunity of doing the research at the institute of nuclear physics and to write this thesis in her group. In addition I want to thank her for her interest and all the guidance and help she gave me during my time as her PhD student.

I want to thank the A1-group for all the assistance and help while performing the beam time and the analysis, especially was always available to help with words and deeds. Likewise the entire AG I have to thank for the helpful discussions and the advise. Not to be forgotten are also all the people at MAMI, who made the experiment for this work possible.

I will always enjoy remembering the time with my fellow PhD student , and who shared the office with me, as well as and from the offices across the hallway. We went through a lot of good and bad times during the course of our PhD theses.

For the detailed correction of my thesis I have to thank a lot , and . Equally I want to say thank you to for his help finding mistakes in my written english and solving several Latex formatting problems.

Special thanks goes to my family and friends who always supported me and motivated me in all possible circumstances during the last years. In particular I want to thank for all the motivation and support he provided, not only with a lot of diverting conversations during lunch breaks, but also at many other occasions like all the events during the 'fifth season' in Mainz.

Last but not least my gratitude goes to my husband , who has been by my side throughout this PhD and who encouraged and helped me with his love and patience in all good and bad times, not only during my thesis, but in the last 16 years.